An investigation of the effects of axle spacing on the rail bending stress behavior

by

Lihua Zhang

A thesis submitted in partial fulfillment of the requirements for the degree of

Master of Science

in

Structural Engineering

Department of Civil and Environmental Engineering

University of Alberta

Abstract

Under heavy and frequent train loads, large stresses can develop in the rail, of which the bending stress is an important portion. Bending stress may cause fatigue defects to grow and also result in rail breaks, which is the dominant failure mode according to the records of derailments caused by rail issues reported by the Transportation Safety Board of Canada.

In this study, the rail bending stresses under different track and loading conditions when the axle spacing between adjacent railcars varies were investigated. Finite element models of different complexities were established using ABAQUS. The Winkler model was also used in the investigation for comparison and reference. Three levels of track modulus, which are 13.79 MPa, 27.58 MPa, and 41.37 MPa were studied, representing soft, medium and stiff track conditions respectively. Two rail sections, the 115 RE rail and the 136 RE rail, were used, which are common rail sections in North American freight railways. Location effects of wheel loads on the rail bending stress behavior when the axle spacing varies were also examined.

It is demonstrated that when wheel loads were applied at the middle of the rail head surface, under each track modulus and for each rail section, the maximum bending stress at the rail head generally follows a pattern of first increasing and then decreasing when the axle spacing increases, while the maximum bending stress at the rail base fluctuates in a small variation range and does not show a clear pattern.

This thesis provides useful guidance in the aspect of studying the effects of axle spacing on the rail bending stress behavior. At the end of the thesis, limitations of current work, recommendations, and future work were also addressed.

Acknowledgements

This work was carried out at the Department of Civil and Environmental Engineering, University of Alberta, Edmonton, Canada, under the supervision of Dr. Mustafa Gül and Dr. Michael Hendry.

The work is under the financial support from the Canadian Rail Research Laboratory (CaRRL).

Table of Contents

List of Figures

List of Tables

List of Nomenclature

E	Modulus of elasticity
I	Moment of inertia
k	Spring stiffness
x	Longitudinal coordinate
P	Wheel load
U	Track modulus
$w(x)$	Deflection of the beam (rail)
$M(x)$	Moment distribution of the beam (rail)
$q(x)$	Distributed load along the beam (rail)
L1	The axle spacing between adjacent railcars
L2	The spacing between the two inboard axles of a railcar
L3	The spacing of two adjacent axles mounted on a common truck
α	Linear thermal expansion coefficient
∇^2	Laplace operator
T	Tension field
H	Foundation layer thickness
Q	Vertical supporting force of a unit length of rail
f	Loading function

E_f, G_f	Material property constants of the foundation
K_G	Parameter of the impressible layer
D	Wheel diameter
p	Single wheel load
σ_V	Vertical bending stress
M_V	Vertical bending moment
y	Distance from the rail neutral axis
H_r	Height of the rail
W_h	Width of the rail head
W_b	Width of the rail base
A	Area of the rail cross section
H_n	Height of neutral axis above the rail base
I_{xx}	Moment of inertia of the rail cross section about the neutral axis
S_h	Section modulus of the rail head
S_b	Section modulus of the rail base
ρ_r	Density of the rail
σ_y	Yield strength
σ_t	Tensile strength
a_c	Crack length

N	Number of cycles
ΔK	Stress intensity factor
n, A_c	Coefficients in the Paris Equation
α_c	Edge correction factor
S	Stress
S_{max}	Maximum stress
S_{min}	Minimum stress
L_c	Length of crossties
W_c	Width of crossties
H_c	Height of crossties
ρ_c	Density of crossties
P_d	Dynamic wheel load
P_s	Static wheel load
φ	Dynamic impact factor
v	Train speed
C	Damping matrix
M	Mass matrix
K	Stiffness matrix
ξ_1, ξ_2	Damping ratio

ω_1, ω_2	Circular frequencies of vibration in the system
a	Mass proportional damping
b	Stiffness proportional damping

CHAPTER 1:INTRODUCTION

1.1 Background of the research

Freight railway transportation plays an important role in the promotion of economic developments within Canada due to the efficiency of transporting goods by rails over long distances. Canada has one of the largest railway networks in the world with a track network of more than 48,000 kilometers, spanning the continent. This network carries more than 70% of the country's goods by mass (Transportation Safety Board of Canada (TSB), 2013). The current trends within the industry are to run more frequent and longer trains, to meet the growing transportation needs of its customers. These trends have created additional challenges for the railway operators in ensuring the safe operation of the railway network.

Of the reported main-track derailments in 2015, approximately 15% were attributed to rail issues, such as broken rails, rail joint bars, or welds within the rail (TSB, 2016). Most of these rail failures occur due to excessive stress (Igwemezie, et al., 1993) or accumulated damage to the rail (Lewis and Olofsson, 2009; Lyons, et al., 2009). The cyclic bending stresses that are generated during the passage of a train are of particular concern as they contribute to the development and propagation of defects and crack within the rail (Orringer, 1988; Jeong and Gordon, 2009). The magnitude and location of the maximum bending stresses in the rail are a result of several factors. These factors include the magnitude and location of the axle loads, the type of rail, and the supporting property beneath the rail (Jeong and Perlman, 2013). Of these factors, the spacing of the axles is one that has not been extensively evaluated to determine if there is the potential to reduce the rail stresses and the resulting number of rail breaks. This relationship of the axle spacing between the adjacent railcars vs. the maximum bending stress in the rail is the focus of the study presented within this thesis.

The different axle spacing dimensions are presented in Figure 1.1. Where L1 is the distance between the axles of adjacent (coupled) railcars, L2 is the spacing between the two inboard axles of a railcar, and L3 is the spacing of two adjacent axles mounted on a common truck. L2 is commonly in the range of 12 m to 18 m, and the spacing between these axles is large

enough that the axle loads at one end of the railcar do not influence the maximum bending stresses that result from the axle loads at the other end. The dimensions of the trucks which carry pairs of axles on each end of the railcar is standardized to allow for them to be interchangeable with different freight car types, and as a result L3 is constant. L1 varies widely between different types, models, and manufactures of railcars. The axle spacing L1 is short that the maximum bending stresses are a result of the influence of the four axle loads.

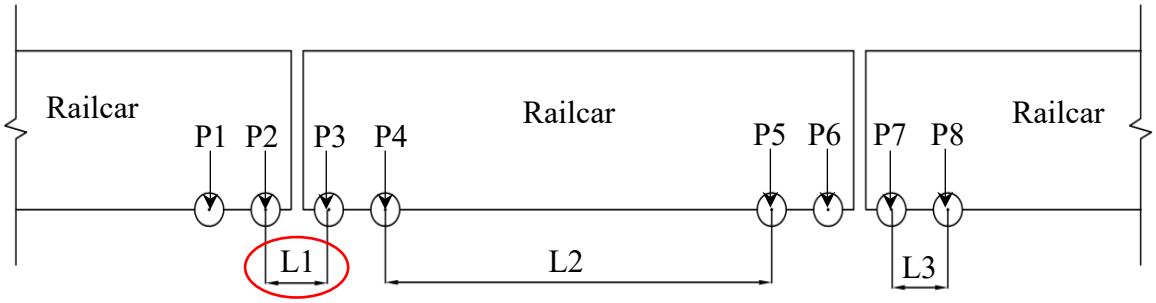

Figure 1.1. A common configuration of railcars

1.2 Research objectives

The overall objective of this study is to evaluate the relationship of the axle spacing between adjacent railcars (L1) vs. the maximum bending stresses generated within the rail. And, to determine from these results if the spacing could be optimized to reduce the magnitude of the maximum bending stresses and thus the failure of rail and rail components. With further analysis conducted to determine the impact of different track moduli (support stiffness), rail sections and wheel load locations on this relationship.

This overall objective was divided into the three specific objectives listed below.

1) To assemble the necessary background information on the track components, substructure behaviour and properties, railcar configurations used within the industry, and the nature of the modelling conducted within previous studies to allow for the construction of representative numerical models.
2) To evaluate the location of the maximum bending stresses generated within the head and base of the rail due to the application of the axle loads, and the effect of the increasing model complexity on these maximum stresses.

3) To determine the relationship between the axle spacing L1 and the maximum bending stresses in the rail. And, to evaluate the impact of track moduli, rail sections and wheel load locations on these results.

1.3 Organization of the thesis

These thesis is comprised of five chapters including this first introductory chapter.

Chapter 2 presents a literature review, and assembles the necessary background information on the composition of the ballasted railway track structure. This is then followed by previous efforts to model these railway track systems, a review of the rail stress composition and factors influencing the rail bending stress behavior, and finally a description of the relation between the rail bending stress and rail defects.

Chapter 3 presents the methodology used in the thesis and provides a detailed description of the finite element models developed for this investigation.

Chapter 4 presents the results from the modelling for the investigation of the maximum bending stresses, and the relationship between these stresses with the axle spacing L1 under different track moduli, rail sections and wheel load locations.

Finally, *Chapter 5* summarizes the conclusions developed within the other chapters and offers recommendations for future work.

CHAPTER 2:LITERATURE REVIEW

2.1 Ballasted railway track system composition

A typical ballasted railway track system can be divided into the substructure composed of ballast, subballast and subgrade, while the superstructure consists of rails, fastening systems and crossties, as shown in Figure 2.1.

Ballast is a layer of crushed uniform size granular material. It is the top layer in the substructure system and has many functions. The most important functions include retaining the track position by the resistance of longitudinal, lateral and vertical forces applied on crossties, reducing the pressure in underlying materials through resiliency and energy absorption, draining away water in the track and storage of fouling materials through voids, and rearrangement during the maintenance process thus restoring the required track geometry (Ali et al., 2013).

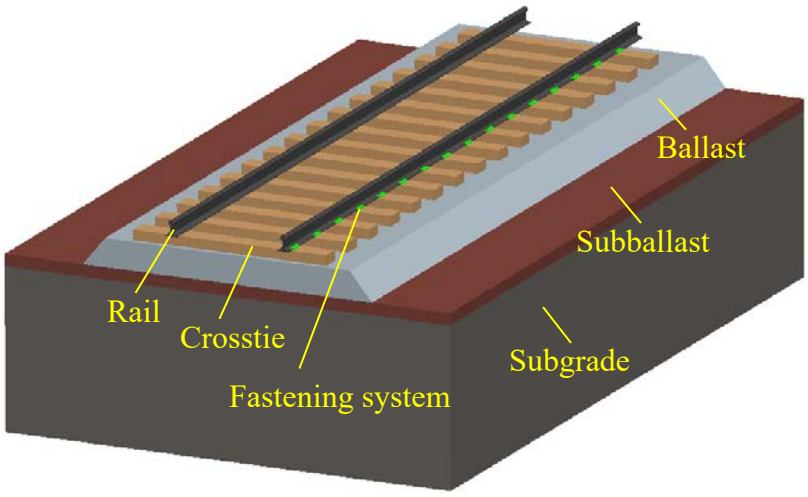

Figure 2.1. A typical ballasted railway track system composition

Subballast is a layer of broadly graded materials placed between the ballast and the subgrade. The subballast can assist in reducing the stress or pressure from the bottom of the ballast layer to a level that is tolerable for the lower subgrade layer. In addition, subballast can prevent the interpenetration between the ballast layer and the subgrade layer due to its material property, thus the migration of fine materials from the subgrade layer to the ballast layer can be reduced. By acting as a surface layer for water to shed away,

subballast can facilitate the drainage in the track system. The attrition between ballast and subgrade can also be mitigated by the subballast due to separation (Kennedy, 2011).

Subgrade is the final foundation layer of the track system and can be composed of placed fill or naturally existing soil. It bears the resultant load from all upper components and also facilitates the drainage of the track system (Steffens, 2005).

Crossties, also called sleepers, are the discretely laid supports under the rails. The main function of crossties is to transmit rail seat loads to the lower substructure layers. Another important function is maintaining track gauge, alignment and level by providing stable supports for rail fasteners (Sadeghi, 2010).

The fastening system is a group of components that form together to attach a rail to the crosstie below. It provides resistance to prevent the rail from overturning and also prevents unacceptable movements in longitudinal, lateral and vertical directions. It can also increase the elasticity of the track system and act as buffering parts for wheel rail impact loads. The wear due to movements between rails and crossties under impact loads can also be reduced by tight fastening systems (Vantuono, 2008).

Rail in the track system, is the component in direct contact with railcars. The rail functions as guiding railcars and providing a smooth running surface for the railcars passing on it. In addition, the rail directly bears and transmits the train loads to the components below it in the track system (American Railway Engineering & Maintenance-of-Way Association (AREMA), 2003). Under frequent and heavy train loads, fatigue cracks and other various types of defects which are usually caused by excessive stress or plastic strain accumulation may occur in the rail. These defects can harm the performance of the whole track system and in a severe case, may even cause derailments.

2.2 Numerical models widely used for the railway track system

2.2.1 Beam on elastic foundation (BOEF) model

The classic model used to investigate the railway track system is the beam on elastic foundation model. It was proposed by Winkler in 1867 (Winkler, E., 1867) and can be called BOEF model or Winkler model (see Figure 2.2). In the BOEF model, the rail is taken as an infinite Euler-Bernoulli beam with a flexural rigidity *EI* resting on a continuous

elastic foundation, which is called the Winkler foundation and can be seen as a uniform and infinite line of vertical and uncoupled linear elastic springs with a stiffness of k (Newton, 1979; Skoglund, 2002). Thus, the supporting force under the rail is proportional to the deflection of the beam.

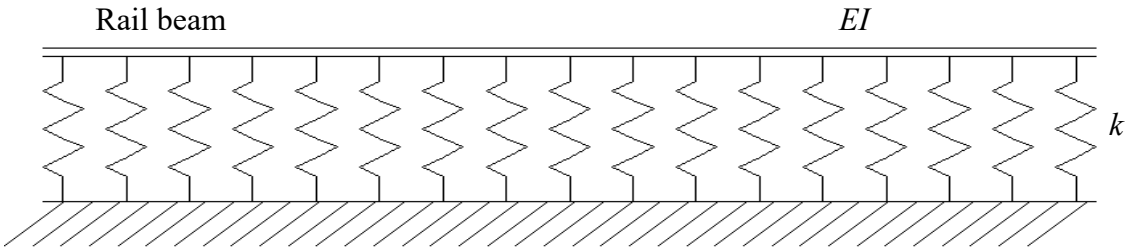

Figure 2.2. Beam on elastic foundation model

The deflection of the beam denoted by $w(x)$ can be obtained using Equation 2.1.

$$EI\frac{d^4w(x)}{dx^4}+kw(x)=q(x) \tag{2.1}$$

where, x is the length coordinate along the beam, and $q(x)$ represents the distributed load on the beam.

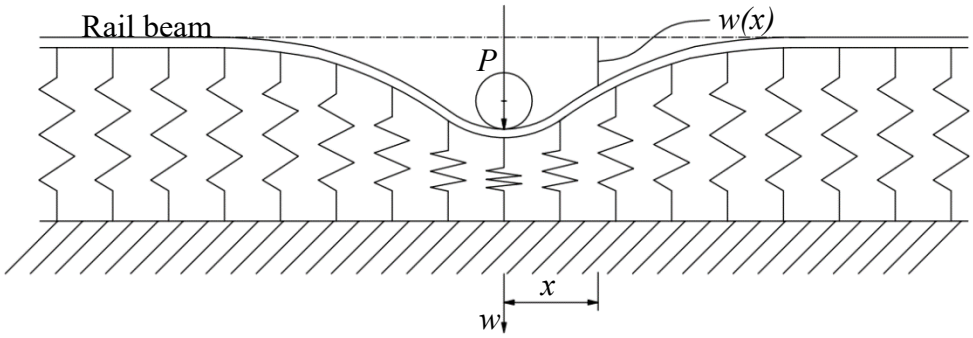

Figure 2.3. Analytical model for rail deflection and bending moment calculation

When a wheel load P is acting on the rail (see Figure 2.3), the deflection and bending moment can be calculated using Equation 2.2 and Equation 2.3 respectively (Sadeghi, 2010).

$$w(x)=\frac{P\beta e^{-\beta x}}{2U}(\cos\beta x+\sin\beta x) \tag{2.2}$$

$$M(x) = \frac{P}{4\beta} e^{-\beta x} (\cos \beta x - \sin \beta x) \tag{2.3}$$

where, x is the distance from the load point, $w(x)$ and $M(x)$ are the rail vertical deflection and rail bending moment, respectively, at the location of x distance from the load location, U is the track modulus, and β is a parameter that can be calculated using Equation 2.4.

$$\beta = (\frac{U}{4EI})^{1/4} \tag{2.4}$$

When the rail is under multiple wheel loads, since the BOEF model assumes linear track responses, individual responses of the rail under each wheel load can be calculated separately and then superimposed together to get the final response of the rail under multiple wheel loads (Skoglund, 2002).

There are some assumptions or limitations in the BOEF model. The BOEF model assumes continuous foundation and continuous welded rail (CWR). The track response is assumed to be linear and only vertical responses are considered. The shear deformation of the rail is neglected due to the Euler-Bernoulli beam assumption. Another evident limitation in the BOEF model is that tensile response or stress can develop in the foundation which is not realistic. Other limitations in the BOEF model include circular definition of foundation stiffness, no time dependent behavior, etc. (Skoglund, 2002).

Some researchers have developed methods trying to avoid one or more limitations in the BOEF model. For instance, Adin et al. (1985) use the finite element method to solve the tension problem in the BOEF model by using beam elements especially for a beam on the Winkler foundation which have exact stiffness matrices. Skoglund (2002) tackles the tension problem by adding equal opposite loads to the uplift regions in the BOEF model. In this model, the nonlinearity of supports is also taken into account.

Despite of those inherent limitations, the BOEF model is simple and direct to use, and meanwhile can give us a good understanding of the track behavior. It is still widely in use and has often been applied as a reference in railway track design and research. The BOEF model also forms the foundation of subsequent improvements in railway track model establishments.

2.2.2 Beam (rail) on discrete supports model

In the BOEF model, track components below the rail are combined together and represented by a layer of continuous springs, so there is no separation between crossties, ballast, subballast, etc. In addition, the spacing between crossties is not taken into account, which is not the case in reality. Another type of model called beam (rail) on discrete supports model provides some solutions to these problems.

The biggest difference between the beam (rail) on discrete supports model (see Figure 2.4) and the BOEF model is that, the connection between crossties and the beam (rail) is modelled using discrete spring and damping units that can form a spring-damper system. The crossties are modelled as rigid masses and also are rested on another spring-damper system which is linked to the ground.

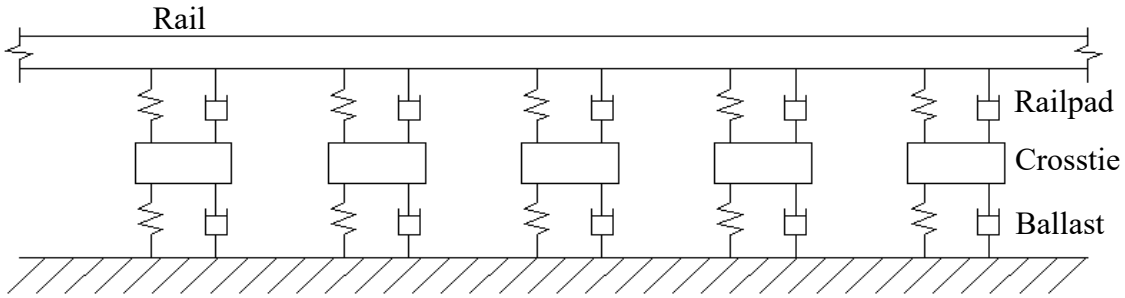

(a) Longitudinal view

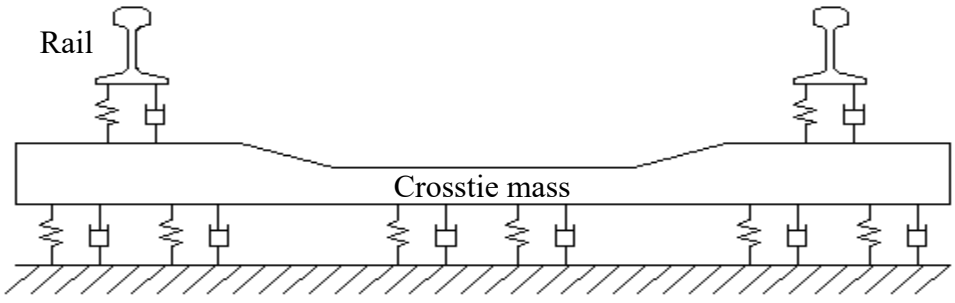

(b) Transverse view

Figure 2.4. Beam (rail) on discrete supports model

A more complex model was developed by Oscarsson (2001) in which the ballast and subgrade masses are taken into account. In addition, the influence of adjacent crossties on

each other is also included by the spring-damper units established between ballast and subgrade masses (see Figure 2.5).

The equilibrium equation for the beam (rail) on discrete supports model can be written as shown in Equation 2.5.

$$M\ddot{x} + C\dot{x} + Kx = f \tag{2.5}$$

where, x is the longitudinal coordinate of the beam (rail), K, C, and M are the stiffness, damping and mass matrices of the track system respectively, and f is the loading function along the beam (rail).

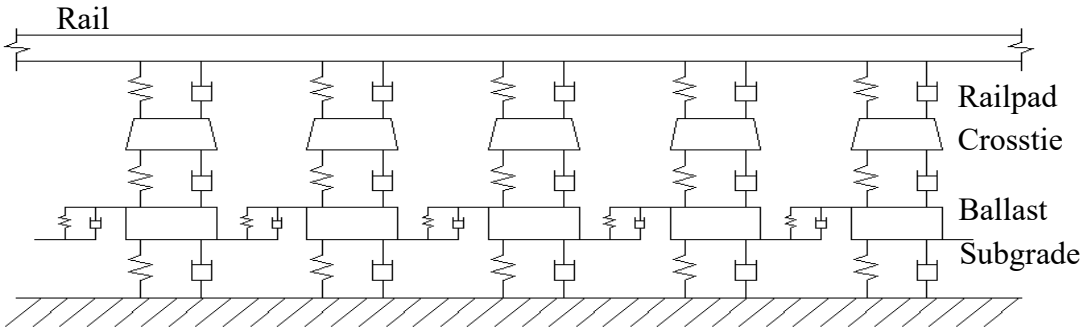

(a) Longitudinal view

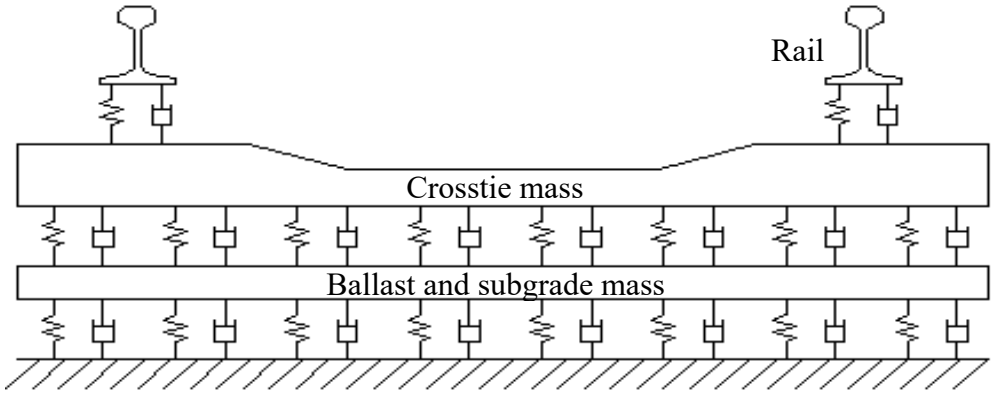

(b) Transverse view

Figure 2.5. Rail on discrete supports model with ballast and subgrade mass included

In the beam (rail) on discrete supports models, the distance between adjacent spring and damping units is set according to the crosstie spacing and its distribution along the track can be either uniform or non-uniform, which is more realistic since the crosstie spacing

may vary during its in-service life. The stiffness and damping parameters of discrete supports can be adjusted according to in-situ data. Meanwhile, these parameters can also be uniform or non-uniform since rail fasteners may be loose at one or more locations and hanging crossties may also occur, which will change the supporting conditions in the track from uniform to non-uniform. The difference between track components can be taken into account by assigning different spring and damper properties to each layer of discrete supports.

2.2.3 Rails on crossties on continuum foundation model

In the rails on crossties on continuum foundation model, the substructure in the track system consisting of ballast, sub-ballast and subgrade is modelled using several layers of three dimensional solid elements (Nguyen, 2011), as shown in Figure 2.6.

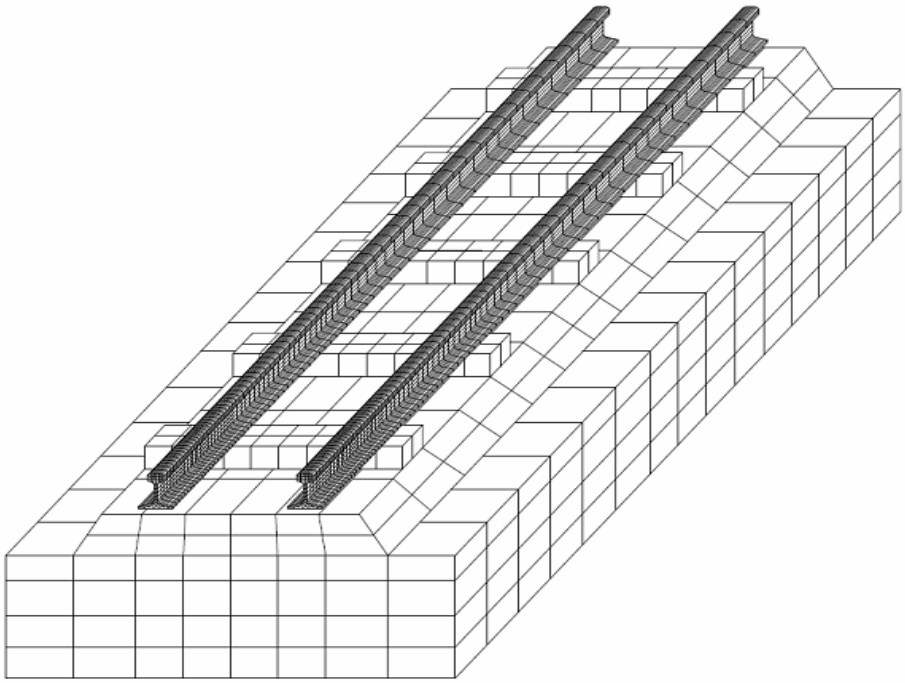

Figure 2.6. Rail on crossties on continuum foundation model

In the rail on crossties on continuum foundation model, different material properties (see Figure 2.7) can be assigned to each layer of solid elements to represent different parts of the foundation (Shahu, 1999; Connolly, 2013). This type of model is quite useful when we need to have a deep investigation into the material behavior and responses of the substructure components in the track system (Powrie, 2007).

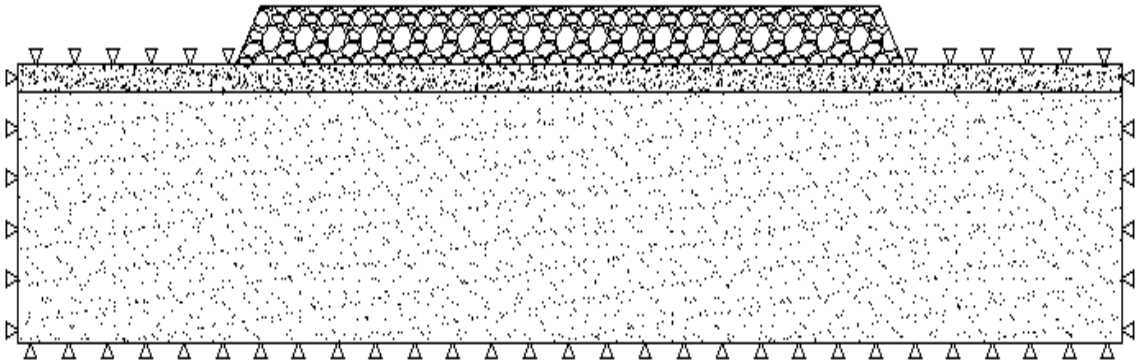

Figure 2.7. Substructure components with different material properties

In addition, the wave propagation from the track system to its surroundings can be simulated by using the rail on crossties on continuum foundation model combined with a modelling of its surroundings (Simon, 2006). One important aspect we should keep in mind is that when the model is small, in order to avoid the wave reflection problem at the boundaries in the track system, non-reflecting boundary conditions should be adopted for modelling (Simon, 2006) or suitable dimensions should be determined to improve accuracy. The rail on crossties on continuum foundation model is the most realistic model and also costs the most in calculation (Simon, 2006). Popp et al. (1999) states that the general rule for modelling is that, "Models should be as simple as possible and as accurate as necessary regarding the task they serve".

2.2.4 Other types of railway track models

In addition to these numerical models mentioned above, there are several other types of models that can be used in railway track engineering.

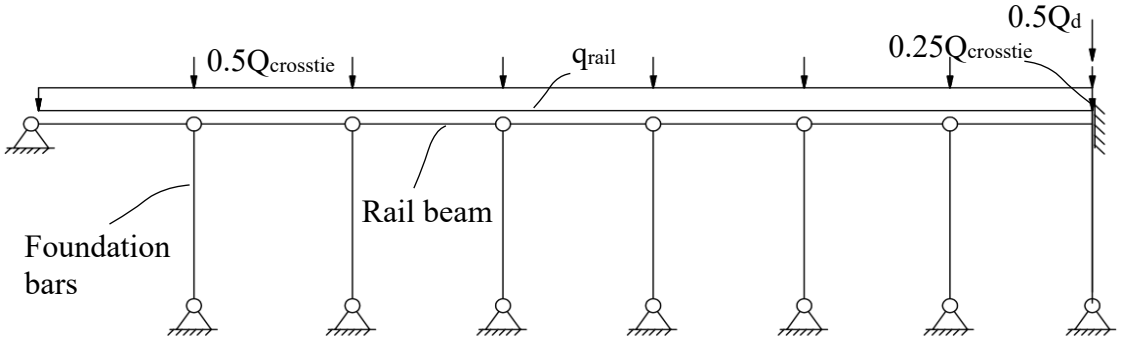

Figure 2.8. Simple Euler-Bernoulli beam element model

In the simple Euler-Bernoulli beam element model in Figure 2.8 (Feng, 2011), the rail is supported by a layer of discretely aligned springs. The springs in this model can be linear supports with tension and compression properties or with compression property only.

In the Filonenko-Borodich foundation model (Filonenko-Borodich, 1940) as shown in Figure 2.9, the top ends of springs are connected to a stretched elastic membrane that is under a constant tension field T, in order to consider the interaction properties between foundation springs. The load-displacement relationship can be expressed by Equation 2.6, in which the intensity of T characterizes the interaction between springs.

$$q = -T\nabla^2 w + kw \tag{2.6}$$

where, ∇^2 is the Laplace operator, q is the load applied and w is the displacement.

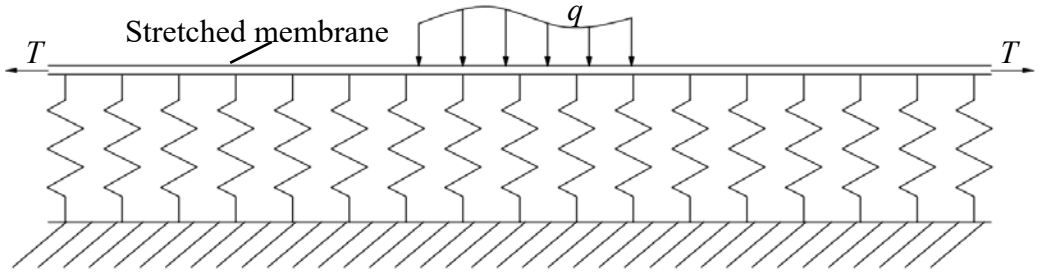

Figure 2.9. Filonenko-Borodich foundation model

In the Pasternak Foundation model (Pasternak, 1954), the shear interactions between springs are introduced by connecting the spring top ends to an incompressible layer resisting transverse shear deformation only. Then the load-displacement relationship can be expressed by Equation 2.7.

$$q = -k_G \frac{d^2 w}{dx^2} + kw \tag{2.7}$$

where, k_G is a parameter of the incompressible layer.

In the Reissner Foundation model (Reissner, 1958), it is assumed that the horizontal displacements at the lower and upper boundaries of the foundation are zero, and in-plane stresses through the foundation are negligibly small. Then the load-displacement relationship for the elastic case can be obtained by Equation 2.8.

$$c_1 w - c_2 \nabla^2 w = -\frac{c_2}{4c_1}\nabla^2 p + p \tag{2.8}$$

where, $c_1 = \frac{E_f}{H}$ and $c_2 = \frac{HG_f}{3}$ in which H is the foundation layer thickness and E_f , G_f are constants relating to the material property of the foundation.

In the Vlasov Foundation model, variational method is used and certain restrictions are imposed upon the possible deformations of the elastic layer. Details of this type of model can be found in the work of Vlasov (1949) and Vlasov and Leontiev (1966).

2.3 Rail stress composition

Rail stress can be taken as a superimposition of three parts, as Figure 2.10 (Jeong, 2011) shows: live load stress caused by railcars running on the rail, thermal stress caused by temperature change, and residual stress that may develop during the manufacturing process and also the in-service process of the rail. For live load stress, it includes wheel-rail contact stress and bending stress due to flexural behavior of the rail under train loads.

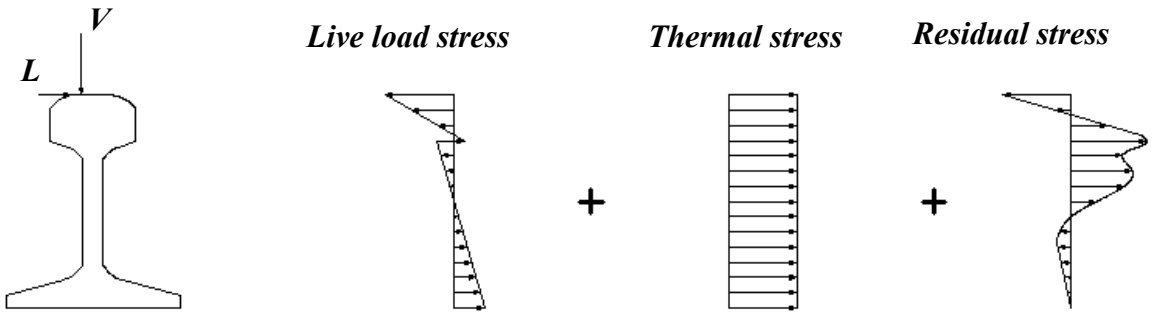

Figure 2.10. Superimposition of rail stresses (Jeong, 2011)

The bending stress can be calculated as a sum of three components caused by vertical loads, lateral loads and torsional loads on the rail, as shown in Figure 2.11 (Jeong, 2013). Among these components, while the bending stresses from lateral loads and torsional loads have influence on the rail performance, the bending stress due to vertical loads dominates (Cannon, 2003).

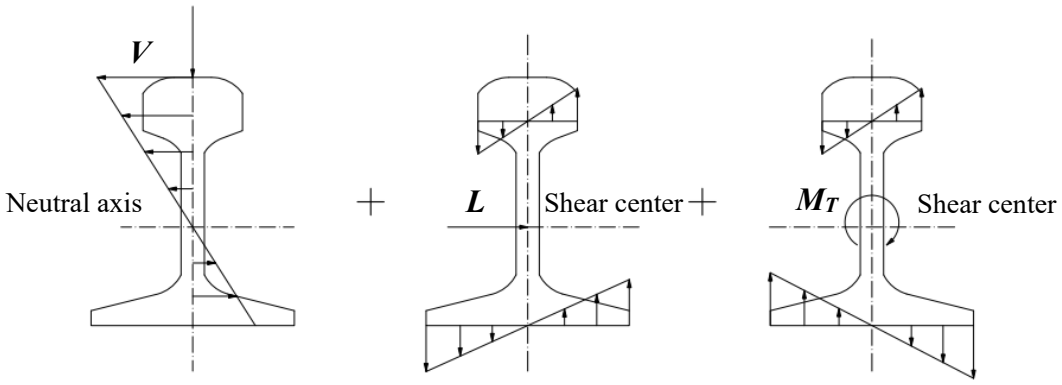

Figure 2.11. Bending stress composition in the rail (Jeong, 2013)

Thermal stress is the uniform stress in the rail originated from the difference between the rail neutral temperature or stress-free temperature and the rail instantaneous temperature. Rail neutral temperature is the temperature at which there is zero longitudinal stress or force in the rail. The initial rail neutral temperature is the temperature when the rail is installed (Lim, 2003). Afterwards, due to the temperature change in environment, the rail's temperature may increase or decrease, thus causing in the rail either compressive stress, when the rail instantaneous temperature is above the rail neutral temperature, or tensile stress, when the rail instantaneous temperature is below the rail neutral temperature, respectively, which are called thermal stress (Zerbst, 2009). When the thermal stress reaches a certain limit, it can lead to the rail buckling due to excessive compression (Szelążek, 1992) or facilitate the rail cracking with tension (Hirao, 1994), which are great threats to the railway transportation safety. Thus, after some time, the thermal stress in the rail needs to be released through maintenance and the initial rail neutral temperature may change during and after this process (Kish, 2005).

Residual stress is mainly developed from the manufacturing process and can also develop during the in-service life of the rail. To be specific, the manufacturing process is comprised of three steps which are hot rolling, cooling and straightening. In each step, residual stress can develop, although the straightening step has been proven to contribute most to the residual stress in the rail (Biempica, 2009). When the rail is in service, under cyclic wheel load passages, the plastic flow from wheel-rail contact will also add to the rail residual stress (Jeong, 2011).

2.4 Factors influencing the rail bending stress behavior

2.4.1 Track modulus

Track modulus is a measure of the rail foundation vertical stiffness (Selig and Li, 1994) and it is defined as the supporting force needed of a unit length of rail per unit deflection, as expressed by Equation 2.10.

$$U = Q / w \tag{2.10}$$

where, Q is the vertical supporting force of a unit length of rail and w is the corresponding rail deflection.

In general, track modulus is an indication parameter of the track quality and a higher track modulus is usually associated with better track performance（Selig and Li, 1994). From Equation (2.2)-Equation (2.4), we can see that, the deflection and bending moment of the rail are both greatly dependent upon the track modulus U. Since the bending moment is directly related to the bending stress generated in the rail, the track modulus U will influence the rail bending stress behavior. A track modulus value of 27.58 MPa (4000 psi) is recommended by the AREMA (2006) for a typical railway track with light to medium rails. In addition, a minimum track modulus value of 13.79 MPa (2000 psi) is needed to ensure a satisfactory railway track performance (Hay, 1982; American Railway Engineering Association, 1991). Raymond (1985) suggested an optimum track modulus value between 34.47 and 68.95MPa (5000 to 10000 psi). Ahlf (1975) concluded that when the track modulus is less than 13.79 MPa, the track quality is poor, when it's between 13.79 MPa and 27.58 MPa, the track quality is average, and when higher than 41.37 MPa, the track quality is good. In general, a higher track modulus is considered to provide higher track performance. However, a too high track modulus will not always be good since it is beneficial to have some track resilience to accommodate dynamic vehicle-track interaction (Li, et al., 2002).

For a certain track condition, the general method to determine the track modulus is to measure the deflection of one rail under a given load and with both rails on each side of a crosstie loaded simultaneously. The track modulus can also be obtained using numerical

methods. Details about how to obtain track modulus through field tests or numerical methods are discussed by previous researchers (Kerr, 1985; Selig and Li, 1994).

2.4.2 Rail section

The rail section has evolved from a variety of early shapes (eg. the cast-iron plate created in 1767) to the modern self-supporting T-rail section still in use today (Armstrong, 2008). The T-rail section, since first rolled in 1831, has been the standard in North American railways (AREMA, 2003). The rail section is identified using a number indicating the rail weight per unit length followed by a code representing the engineering group that created the design plan for the rail section. Some common section codes are the following: "RE"-AREMA, "REHF"-AREMA "head free" section, "ASCE"-American Society of Civil Engineers, and "ARA-A/B"-American Railway Association "A" section or "B" section (AREMA, 2003). Based on these identification rules, the 115 RE rail section means the rail has a nominal weight of 115 lb/yd and the rail section is rolled to standard specifications established by the AREMA.

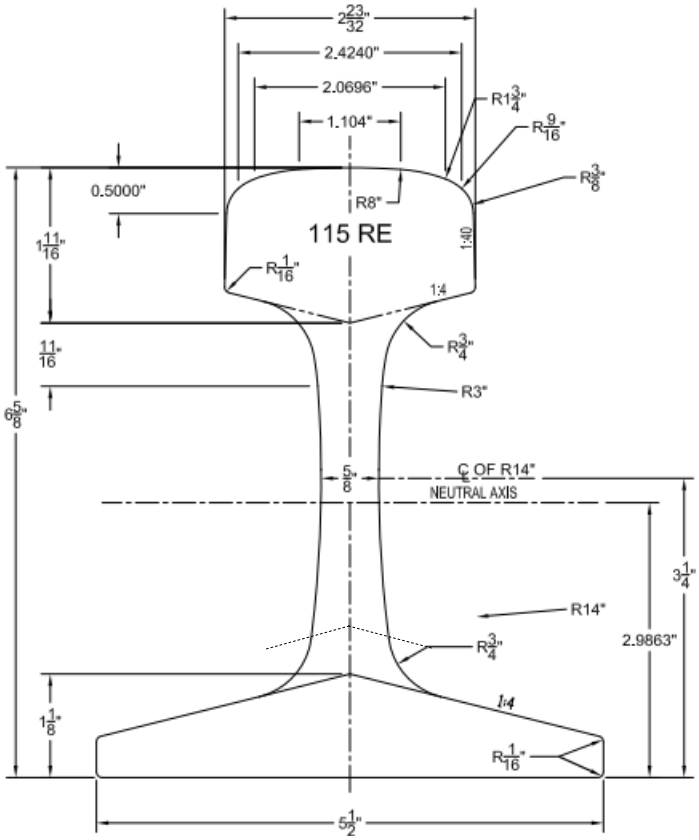

Figure 2.12. The 115 RE rail section (AREMA, 2011)

Figure 2.12 and Figure 2.13 give examples of the 115 RE rail section and the 136 RE rail section from the AREMA Manual for Railway Engineering (AREMA, 2011).

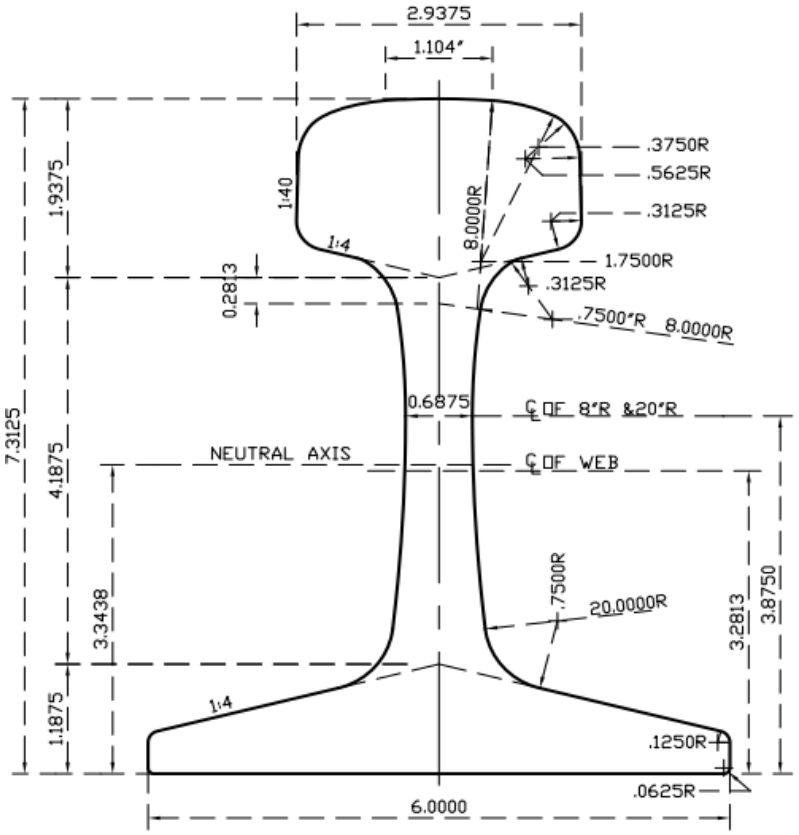

Figure 2.13. The 136 RE rail section (AREMA, 2011)

The cost of rail is directly related with the rail weight, thus the rail section with the heaviest rail weight is usually reserved for tracks carrying the highest level of traffic loads. The rail size can vary from 90 lb/yd, which is used for light transit tracks, to 141 lb/yd, used for heavy-haul railway operations (Armstrong, 2008). Except for specific purposes (e.g. special track work, repair rail and insulated joint replacement), the new rail sections recommended by the AREMA to be purchased are limited to the 115 RE, 136 RE and 141 RE sections (AREMA, 2011).

Assuming that the entire rail cross section is elastic, the rail bending stress under the vertical wheel load can be obtained from Equation 2.11 (Hibbeler, 2010).

$$\sigma_V = \frac{M_V y}{I} \tag{2.11}$$

where, M_V is the vertical bending moment at the rail cross section, y is the distance of the point on the rail cross section to the rail neutral axis, and I is the moment of inertia of the rail cross section with respect to its neutral axis.

Equation 2.11 indicates that the rail cross section property is related to the rail bending stress. Many studies conducted on the rail bending stress behavior have used different rail sections. For example, Jeong (2013) examined the rail bending stress and deflection for various conditions combining rail sizes, foundation modulus and the FRA (Federal Railroad Administration) track class. It was found that the minimum rail size needed to support heavy wheel loads (174 kN and above) while not exceeding the allowable bending stress and deflection limits depends on foundation modulus and track class. In the technical report of Shahin (1986), rail size is used as a parameter input to the track model to determine the track structural condition indicators including the rail bending stress. Jeong (2009) investigated the defect growth curves of the 115 RE rail and 136 RE rail using a risk assessment model. It was found that, the crack propagation life of detail fractures in the 115 RE rail is approximately 29% less than that in the 132 RE rail. This finding is consistent with the fact that rail bending stresses are increased due to smaller section properties.

2.4.3 Axle spacing

The proportion of different types of railcars in North America railways by the 1st quarter of 2016 is shown in Figure 2.14 and the data is from the railroad industry equipment database, UMLER®. Among these eleven types of railcars, the three dominant railcar types are covered hoppers (26%), tank cars (21%) and gondolas (12%). For different types of railcars, the range of axle spacing L1 varies. From the statistics of CN, CP, TTX, BNSF, etc., the range of axle spacing L1 for different types of railcars can be summarized as shown in Figure 2.15.

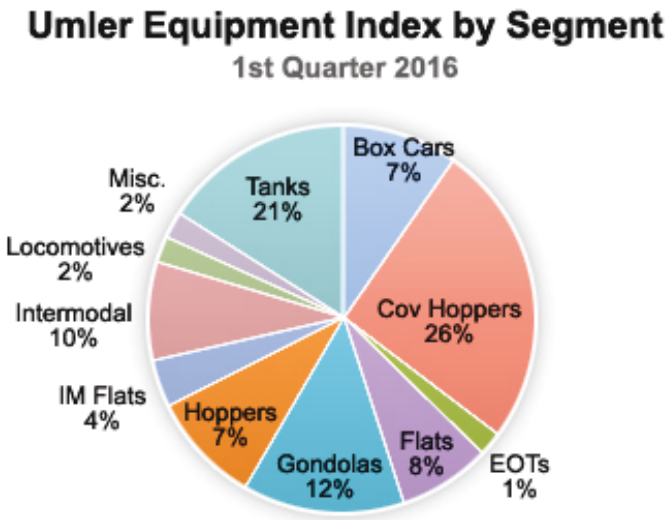

Figure 2.14. Umler Equipment Index for different types of railcars in North America by the 1st quarter of 2016

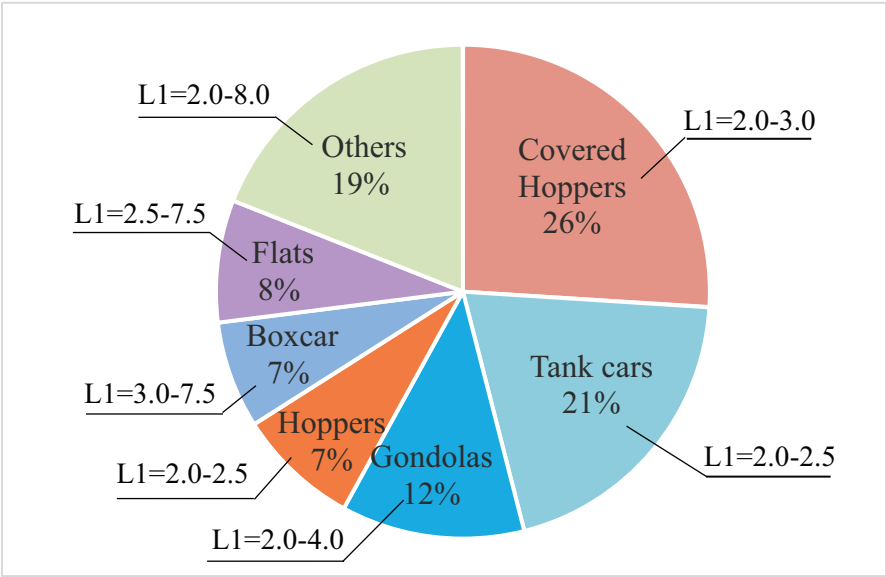

Figure 2.15. The range of axle spacing L1 for different types of railcars

Figure 2.15 shows that, for the three dominant types of railcars, covered hoppers, tank cars, and gondolas, which together comprise 59% of common railcars running in North American freight railways, the range of their axle spacing L1 falls in 2.0-4.0 m. Even for other types of railcars, for example, the hoppers, which represents 7% of all railcars, the range of axle spacing L1 is 2.0-2.5 m, still within the range of 2.0-4.0 m. For boxcars, flats and other types of railcars, the axle spacing L1 has a wider range, which can reach 2.0-8.0

m. However, these types of railcars are not the dominant types of railcars in North America freight railways. Therefore, an axle spacing L1 range of 2.0-4.0 m may be suitable for our investigation.

There is research conducted using different types of railcars that have different axle spacings. However, in these studies, the axle spacing usually is not treated as an independent parameter thus the results are not comparable for investigating the axle spacing effects. For example, in the work of Sadeghi and Shoja (2015), the emphasis is on investigating the effects of train speed, sleeper spacing, railpad stiffness, etc. on the load amplification factor. Although five types of railcars, which have different axle spacing L1, were used in experiments, data for studying the effects of the parameter axle spacing L1 remains incomplete because the focus is not on the axle spacing effects. In the work of Bowess et al. (2007), seven types of railcars were used in experiments and their axle spacing varies. However, the axle load of these railcars are also different. Displacements in the track system were measured to assess the performance and robustness of their measurement systems.

This thesis investigates how the variation of the axle spacing L1 can affect the rail bending stress behavior and hopes to provide meaningful results for future research and practice in this aspect.

2.5 Rail defects

Under long term frequent and heavy train loads, various types of defects may occur in the rail, e.g. wear, corrugation, squat, shelling, head checking, transverse defects, etc. Some of these defects are shown in Figure 2.16 (TSB, 2010; Lewis, 2009; Cannon et al., 2003; NRS&IT).

Among various types of rail defects, transverse defects dominate in today's heavy haul railway transportation and it's also one of the most prevalent and problematic rail defects in North America (Cannon, 2003; Clark, 2004). Transverse defects is a kind of fatigue defects, of which the crack plane is perpendicular to the running direction of the rail (TSB, 2006). Detail fracture and transverse fissure both are transverse defects (TSB, 2008; Fowler and Don, 2013).

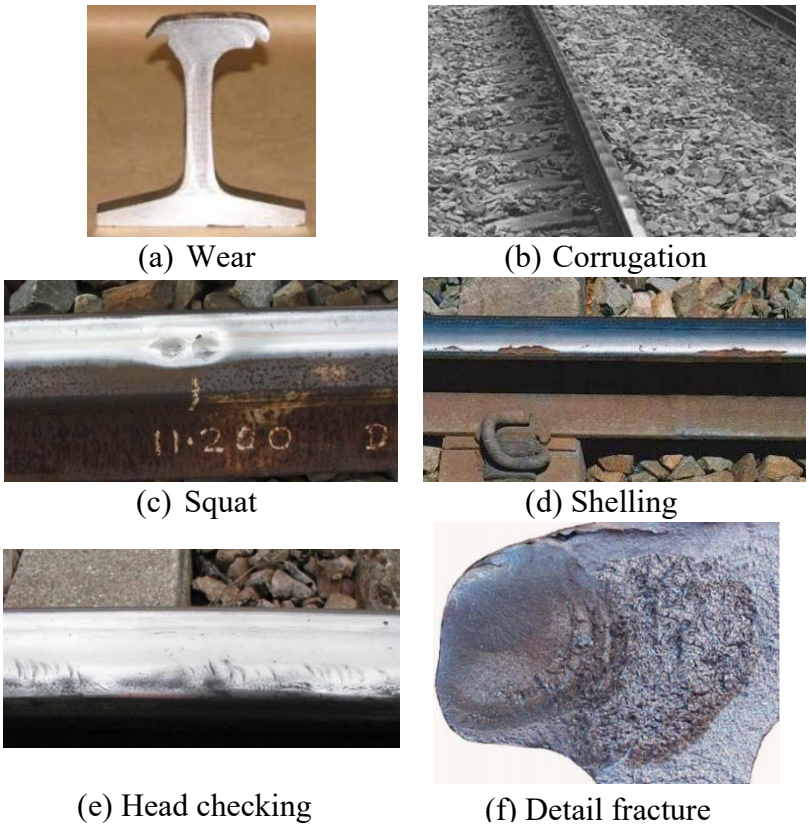

Figure 2.16. Examples of common rail defects (Transportation Safety Board of Canada, 2010; Lewis, 2009; Cannon et al., 2003; NRS&IT)

Transverse fissure, also called tache ovale or kidney defect in different countries around the world (John L. and Roy A., 2015), is a type of progressive crosswise fracture that initiates from a nucleus or crystalline centre in the rail head from which spreads to a round or oval, bright or dark smooth surface substantially at a right angle to the rail's longitudinal direction (Transport Canada). The transverse fissure has internal origins and nearly smooth surface, which is different with other types of rail defects. Transverse fissure is a type of milled defects due to excess hydrogen left in the rail steel during the cooling or vacuum degassing process (Orringer, 1988). With the improvements in the rail steel manufacturing process, such as clean steel, this type of defect can be reduced.

Detail fracture is a type of transverse defect that starts from or near the rail head surface. It may arise from shelling, flaking and head checking (Transport Canada). It accounts for about 75% in the rail defects found in CWR in North America railways (Jeong, 2001).

From the railway investigation reports provided by the Transportation Safety Board of Canada, detail fracture can often be found in rail break or derailment cases.

Detail fracture belongs to fatigue cracks that have three stages: crack initiation, crack propagation, and finally fracture. The crack propagation life, which is also called slow crack-growth life, is defined as the accumulated tonnage for a detail fracture to grow from a detectable size to a critical size that can cause the rail to fail under next train passage (Jeong, 2013). The detail fracture is formed by wheel rail contact stresses under repeated traffic loading. However, the effects of wheel-rail contact stress is usually neglected in the slow crack-growth life of detail fracture and rail bending stress dominates in this stage (Orringer, 1988). Recent studies indicate that an increase in bending stresses due to smaller rail section properties, heavier axle loads or increasing crosstie spacing can increase the crack growth rate and shorten the overall fatigue life of detail fracture (Jeong and Gordon, 2009; Jeong and Gordon, 2011).

The principles of engineering fracture mechanics can be used to estimate the crack propagation life of the detail fracture in the rail. The bending stress in the rail head cycles from compression, when a wheel is directly over the transverse plane containing the defect, to tension, when the wheel has progressed and the defective section is engaged in reverse bending. The passage of a single wheel produces two stress cycles (0, Smax) and (Smin, Smax), as shown in Figure 2.17 (Orringer, 1988).

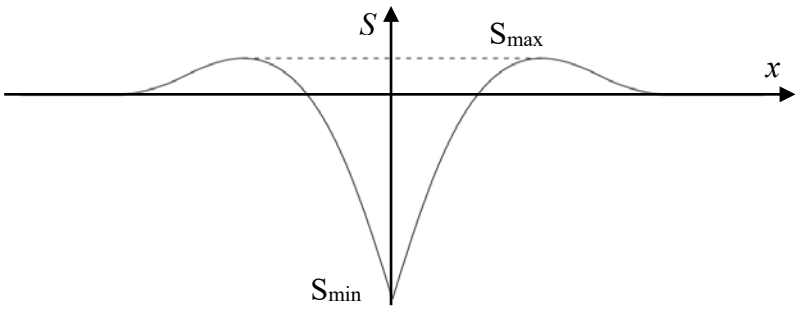

Figure 2.17. Distribution of rail head bending stress under one wheel load

The crack growth rate can be calculated using the Paris Equation as follows (Cortie and Garrett, 1988; Roberts and Talebzadeh, 2003):

$$\frac{da_c}{dN} = A_c(\Delta K)^n \tag{2.12}$$

where, a_c is the crack length, N is the number of cycles, ΔK is the applied stress intensity factor range, n and A_c are material and test condition-dependent coefficients. The determination of n and A_c are complex and some values are given in Table 2.1 (Aglan and Fateh, 2006) for reference.

Table 2.1. Average values of Paris law coefficients (Aglan and Fateh, 2006)

Material	n	A_c
Bainitic rail steel	1.13	1.0×10^{-8}
Pearlitic rail steel	5.44	3.04×10^{-12}

The stress intensity factor ΔK can be calculated using Equation 2.13 (Newman, et al., 1999).

$$\Delta K = \Delta S\sqrt{\pi a_c}\alpha_c = S_{\max}\sqrt{\pi a_c}\alpha_c - S_{\min}\sqrt{\pi a_c}\alpha_c \tag{2.13}$$

where, α_c is the edge correction factor, and ΔS is the stress range in a cycle.

From the above equations, it can be seen that the magnitude of the rail head bending stress is related to the crack growth rate and thus influencing the fatigue life. In this thesis, the rail bending stresses under varying track and loading conditions were investigated, which can affect the detail fracture growth in the rail and in a severe case leading to rail break or derailments.

2.6 Summary

In this chapter, a brief review on the ballasted railway track system and rail stress composition was presented. Different types of numerical models used for railway track system research were described and their advantages and disadvantages were discussed. Factors that can influence the rail bending stress behavior (i.e. track moduli, rail section and axle spacing) were described and related research progress was presented. At last, rail defects were introduced. Detail fracture, the most common type of transverse defect found in the CWR of North American railways was described and its relationship with the rail bending stress was presented. Based on these, the rail bending stress under varying track and loading conditions when the axle spacing L1 varies were proposed as a meaningful topic in this thesis.

CHAPTER 3:METHODOLOGY AND NUMERICAL MODEL ANALYSIS

3.1 Methodology

In many cases, large scale field testing can be impractical for exploratory research and numerical modelling provides a means of exploring the mechanism and trends based on the known physics of the mechanism being explored. In this chapter, different types of finite element models for the railway track system were constructed and the classical commercial finite element analysis software ABAQUS was used. In order to validate our results from the finite element analysis, the Winkler model, which is widely used in railway design and analysis, was used for comparison and reference.

Four types of finite element models of different complexities were established step by step: the Rail on Continuous Foundation Model, the Rail on One layer of Discrete Spring Supports Model, the Rail on Two layers of Discrete Spring Supports Model and the Rail on Continuum Foundation Model. Afterwards, the deflection and bending moment responses of the rail from these models were compared together with that from the Winkler model for validation. In order to see how the relative locations of wheel loads to crossties can influence the rail bending stress behavior when the axle spacing L1 varies, a finite element model in which wheel loads were moved along the rail was established. In reality, wheel loads are usually deviated from the middle point of the rail head surface, thus a finite element model in which the wheel loads were applied at the rail gauge corner was also established. To be brief here, the wheel loads in these models were applied at the middle of the rail head surface if not otherwise specified.

In order to study the effects of axle spacing L1 on the rail bending stress behavior, the relationship of the maximum rail bending stress at the rail head vs. axle spacing L1, the relationship of the maximum bending stress at the rail base vs. axle spacing L1, and the relationship between the mean bending stress at the rail head vs. axle spacing L1 were investigated under different track and loading conditions.

There are various parameters in the railway track system that can make the results incomparable and confusing. Therefore, in each condition, only one parameter was varied and the others remain set. Three parameters were considered in this thesis: the track modulus, rail section and load location.

When the track modulus is considered, the rail section investigated is 115 RE and wheel loads were applied at the middle of the rail head surface. Three levels of track modulus which are 13.79 MPa, 27.58 MPa and 41.37 MPa were investigated. For each type of model, the relationships of the maximum bending stress at the rail head vs. the axle spacing L1 were obtained and compared at different track modulus. Under each track modulus, the maximum bending stresses at the rail head when the axle spacing L1 varies from different types of models were also compared with each other. The same was conducted on the maximum bending stresses at the rail base. The mean bending stresses at the rail head were also obtained and compared with the maximum bending stresses at the rail head when the axle spacing L1 varies under each track modulus based on the data from the Rail on Continuum Foundation Model.

When the rail section is considered, the 115 RE rail and the 136 RE rail were used for investigation. Under each track modulus, the relationship between the maximum bending stress at the rail head of the 115 RE rail and the axle spacing L1 was compared with that of the 136 RE rail for each type of model. The same was conducted on the maximum bending stresses at the rail base. The mean bending stresses at the rail head of the 115 RE rail and the 136 RE rail when the axle spacing L1 varies were also compared together for each track modulus based on data from the Rail on Continuum Foundation Model.

When the load location is considered, two loading cases were established and analyzed. For Case I, the wheel loads were moved along the rail to different locations, thus the relative locations of wheel loads to crossties can vary. At each axle spacing L1, the maximum bending stresses at the rail head when relative locations of wheel loads vary were extracted and plotted under each track modulus. The maximum value and minimum value of these stresses were marked, thus getting the variation range. Afterwards, these stresses were plotted on the former curve representing the relationship between the maximum bending stress at the rail head and the axle spacing L1 in the same condition to

see how the curve pattern can be affected. The same were conducted on the maximum bending stresses at the rail base.

For Case II, the wheel loads were applied at the gauge corner of the 115 RE rail. The relationship of the maximum bending stress at the rail head vs. the axle spacing L1 when wheel loads were applied at the rail gauge corner was compared with that when wheel loads were applied at the middle of the rail head surface for each track modulus. The same was conducted on the maximum bending stresses at the rail base.

3.2 Establishment of the railway track system models

According to the complexity of models, based on the literature review in Chapter 2, four types of finite element models of different complexities were established for our investigation on the rail bending stress behavior at different axle spacings, which are the Rail on Continuous Foundation Model, the Rail on One layer of Discrete Spring Supports Model, the Rail on Two layers of Discrete Spring Supports Model, and the Rail on Continuum Foundation Model. The length of these models is 30 m, which is enough to eliminate the boundary condition effects on the rail bending stress responses under static wheel loads. Each type of finite element model will be described in detail as follows.

3.2.1 The Rail on Continuous Foundation Model

The established Rail on Continuous Foundation Model in ABAQUS is shown as follows in Figure 3.1. In the Rail on Continuous Foundation Model, a layer of continuous elastic foundation was assigned to the rail bottom surface to represent the supports under it, as shown by the red area in the detailed view on the upper left corner of Figure 3.1. Thus, the fastening systems, crossties, ballast, etc. are combined together as a supporting layer under the rail. A set of track modulus values, which are 13.79 MPa, 27.58 MPa and 41.37 MPa, were assigned to the continuous elastic foundation layer respectively to represent the soft, medium and stiff track conditions respectively. Each track modulus were divided by the width of the rail base to obtain the area stiffness of the elastic continuous foundation for each track condition.

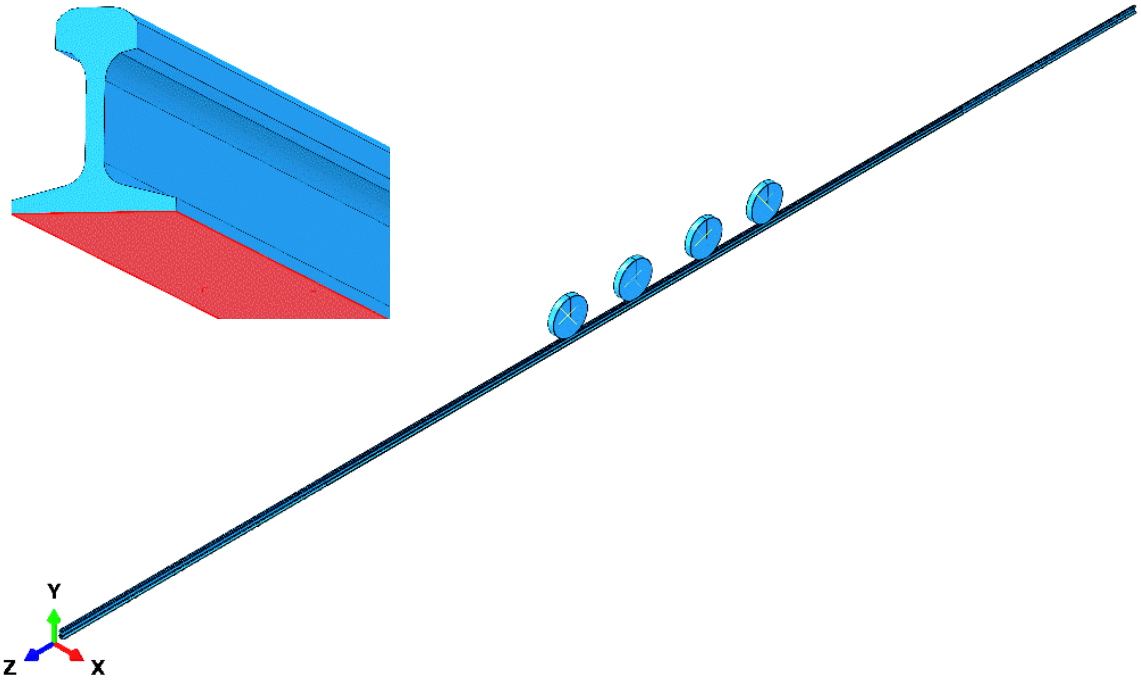

Figure 3.1. The established three dimensional Rail on Continuous Foundation Model and the detail view of the elastic foundation (red area) on the rail bottom surface (upper left corner)

Two rail sections, which are the 115 RE rail and the 136 RE rail, were investigated in the model. The rail cross section geometry parameters are listed in Table 3.1 (AREMA, 2009).

Table 3.1. Rail cross section geometry parameters (AREMA, 2009)

Type	115 RE	136 RE
H_r (mm)	168.3	185.7
W_h (mm)	69.1	74.6
W_b (mm)	139.7	152.4
A (mm^2)	7236.8	8597.6
H_n (mm)	75.9	84.9
I_{xx} (mm^4)	27,263,200	39,209,000
S_h (mm^3)	294,967	388,373
S_b (mm^3)	358,877	462,115

The rail material properties are listed in Table 3.2 as follows (AREMA, 2009).

Table 3.2. Rail material properties (AREMA, 2009)

Variable	Value
E (GPa)	207
ρ (tonne/mm^3)	7.84×10^{-9}
σ_y (MPa)	483
σ_t (MPa)	983, minimum

The allowable rail stress for continuous welded rails can be established as shown in Table 3.3 (AREMA, 2011). Assuming the rail yield strength is 483 MPa, the permissible bending stress in the rail becomes 172 MPa (25 ksi) for the continuous welded rail, which accounts for the effects of various factors except for the dominant load in the vertical direction.

Table 3.3. Recommended rail stress reduction factors for CWR (AREMA, 2011)

Reduction factor	Severity assumption
Lateral bending	20%
Track condition	25%
Rail wear and corrosion	15%
Unbalanced superelevation	15%
Temperature stress	138 MPa

The rail was meshed using the C3D8R elements in ABAQUS, as shown in Figure 3.2. It is an 8-node linear brick element with reduced integration, which has one integration point in the center of the element (Dassault Systèmes Simulia Corp., 2013). A section of 18 m in the middle of the rail was applied with a fine mesh of element size 10 mm. The other parts of the rail were applied with a mesh size of 40 mm. The wheels were modeled as discrete rigid bodies and the element size is 50 mm. The mesh view of the Rail on Continuous Foundation Model is shown in Figure 3.3 as follows.

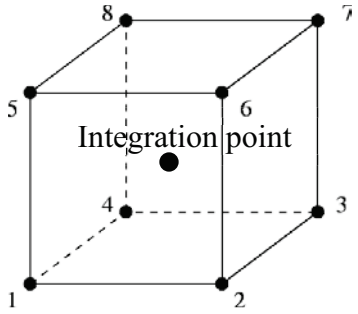

Figure 3.2. The C3D8R element in ABAQUS (Dassault Systèmes Simulia Corp., 2013)

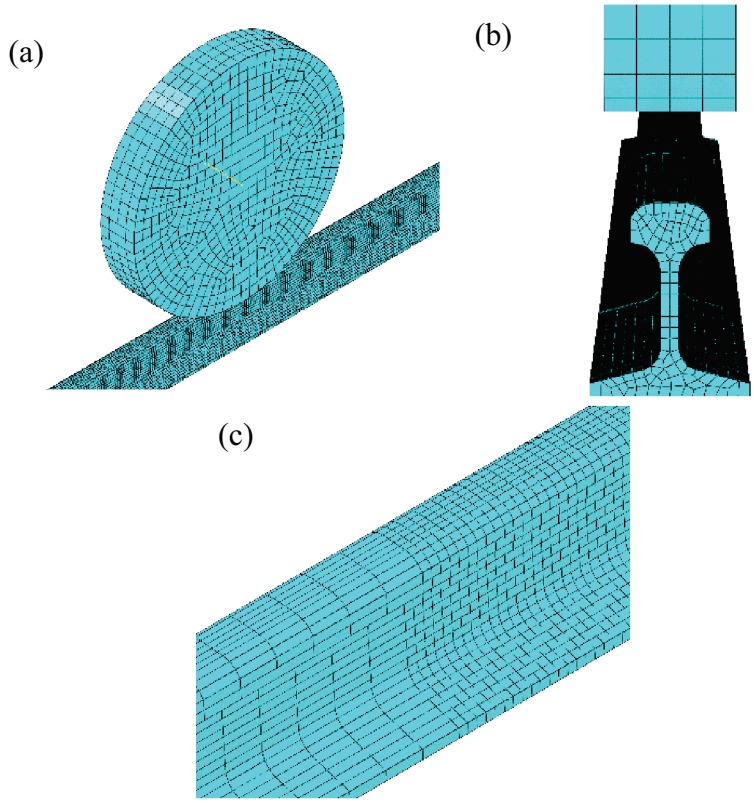

Figure 3.3. Mesh view of the Rail on Continuous Foundation Model. (a) Mesh of the wheel; (b) Mesh of the rail cross section; (c) Mesh variation in the longitudinal direction of the rail.

Surface to surface contact was applied for modelling wheel rail contacts. The wheel surface was defined as the master surface and the rail head surface was defined as the slave surface since the wheel is more rigid than the rail in the model. For the tangential behaviour between the wheel surface and the rail head surface, the friction coefficient can vary from 0.2 to 0.5 due to different lubrication conditions, weather conditions, rail conditions, etc.

(Seo, 2011). In our models, the friction coefficient was set as 0.3, which is a common value for the wheel rail tangential friction property and has often been used in former railway research (Liu, et al., 2006; Sheng, et al., 2006; Liu, et al., 2007; Torstensson, et al., 2014). Penalty method was used for the friction formulation. For the normal behavior between the wheel and the rail, hard contact was used for pressure-overclosure and the penalty method was used for constraint enforcement. The rail was fixed at both ends. The wheels movements were constrained in all but the vertical direction..

The static wheel load can be calculated by dividing the gross weight of the railcar by the number of wheels under it. In our investigation, the gross weight of a railcar is taken as 1272 kN, the maximum gross weight of most railcars running on North American freight railways according to the railcar statistics from CN, CP, BNSF, TTX, etc. Assuming average distribution of the gross weight to eight wheels supporting the railcar, the static wheel load can be calculated as 159 kN. The actual wheel load can be slightly higher or lower than this number due to unbalanced load distribution. The four wheel loads were distributed along the rail symmetrically as in Figure 3.4. The distance between wheel 1 and wheel 2 is 1.78 m, the typical wheel base of trucks in North American freight railways. The distance between wheel 3 and wheel 4 is also 1.78 m. The distance between wheel 2 and wheel 3 varies at 2.0 m, 2.5 m, 3.0 m, 3.5 m, 4.0 m, 4.5 m and 5.0 m. The ABAQUS/Standard module (ABAQUS version 6.13-4, 2013) was used for analysis.

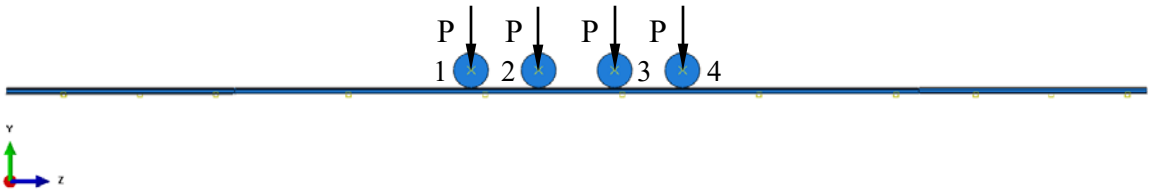

Figure 3.4. Load distribution along the rail in the Rail on Continuous Foundation Model

For the 115 RE rail, under the track modulus of 27.58 MPa and when the axle spacing L1 is 2.0 m, the deflection response of the rail is shown in Figure 3.5. It shows that the maximum deflection of the rail is 6.81 mm.

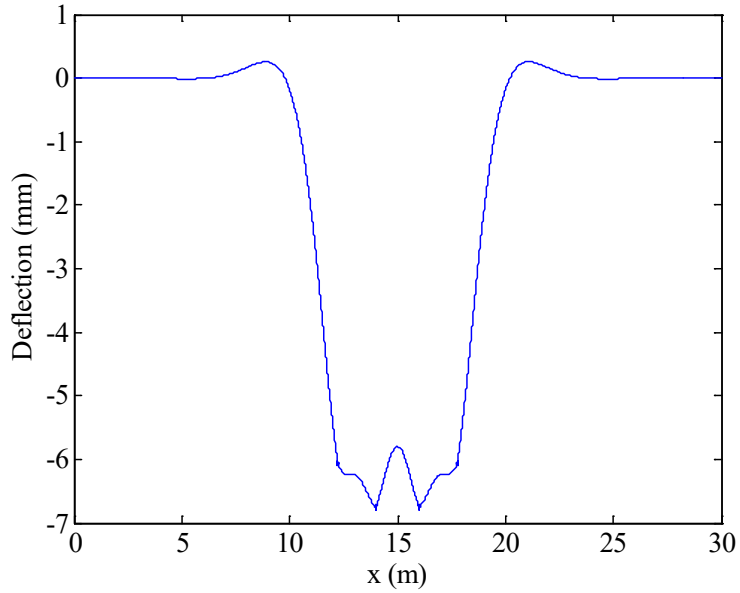

Figure 3.5. Deflection of the rail when the track modulus is 27.58 MPa at the axle spacing L1=2.0 m from the Rail on Continuous Foundation Model

The bending moment at 40 cross sections along the longitudinal direction of the rail were extracted and shown in Figure 3.6. The maximum positive bending moment in the rail is 33.76 kN.m and the maximum negative bending moment is -15.17 kN.m.

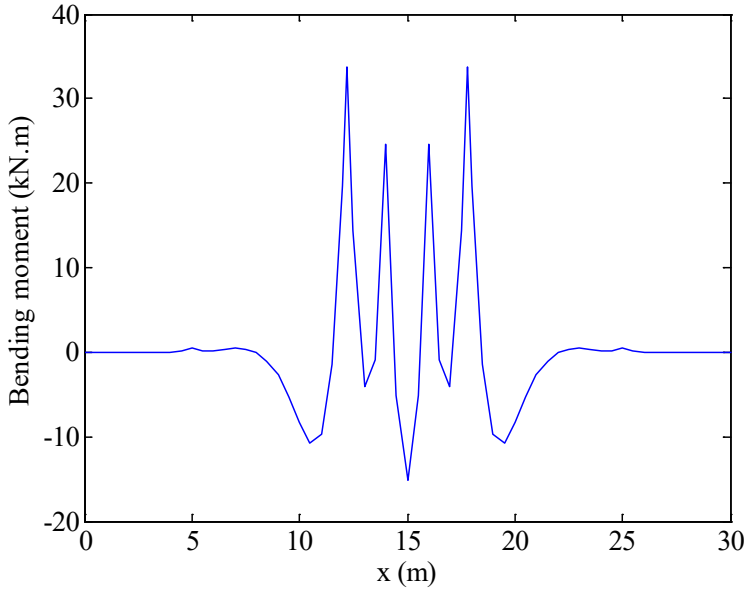

Figure 3.6. The bending moment response along the rail when the track modulus is 27.58 MPa at the axle spacing L1=2.0 m from the Rail on Continuous Foundation Model

Figure 3.7 shows the Von Mises stress distribution of the rail. For a clear distinction, the two wheels near the rail ends are called outer wheels, and the other two wheels are called inner wheels. At the right corner of Figure 3.7 are detail views of the Von Mises stress distribution of the rail at the outer wheel location (DB1) and the inner wheel location (DB2) respectively.

From Figure 3.7, it can be seen that the wheel load pattern is clearly shown by the stress distribution pattern along the rail and the maximum Von Mises stress is 384.0 MPa, which occurs right at the wheel-rail contact area. It also shows that, the stress level is quite low at the area apart from the wheel load acting locations.

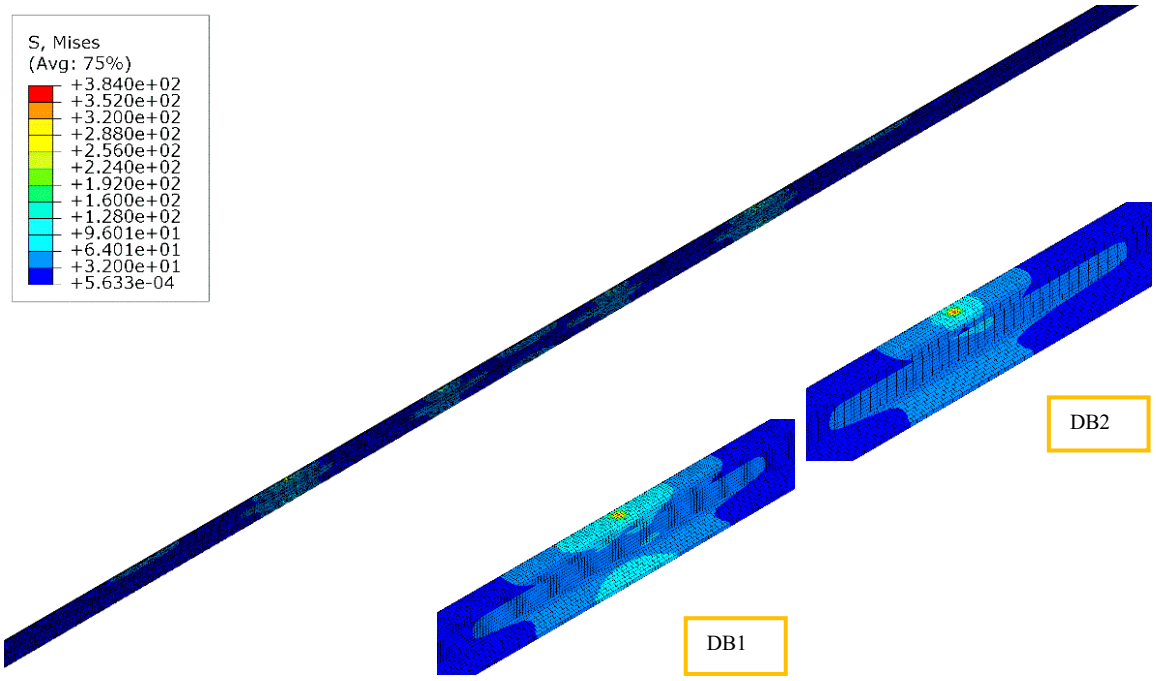

Figure 3.7. Von Mises stress distribution of the rail from the Rail on Continuous Foundation Model. DB1-Von Mises stress distribution of the rail at the outer wheel location; DB2- Von Mises stress distribution of the rail at the inner wheel location.

The bending stress distribution along the rail is shown in Figure 3.8. At the right corner are detail views of the bending stress distribution at the outer wheel location (DB3) and inner wheel location (DB4) respectively. From Figure 3.8, it shows that the maximum bending stress is 95.78 MPa which is tensile and the minimum bending stress is -360.9 MPa, which is compression, always occurring at the wheel rail contact area.

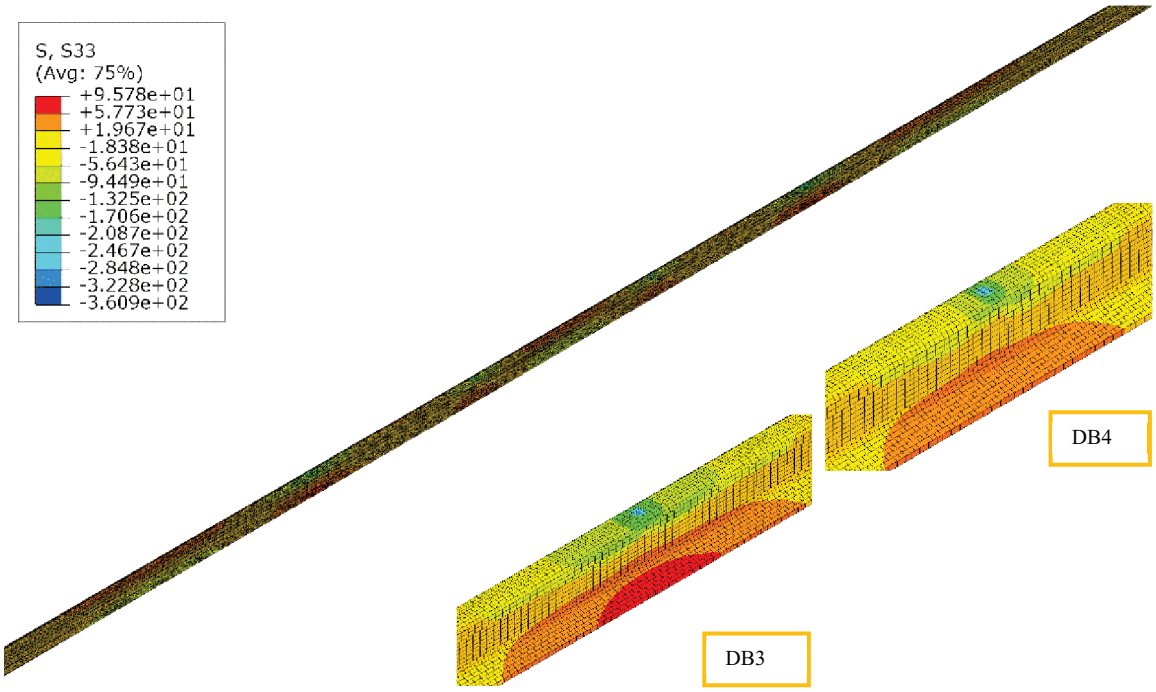

Figure 3.8. Bending stress distribution of the rail from the Rail on Continuous Foundation Model. DB3-Bending stress distribution of the rail at the outer wheel location; DB4-Bending stress distribution of the rail at the inner wheel location.

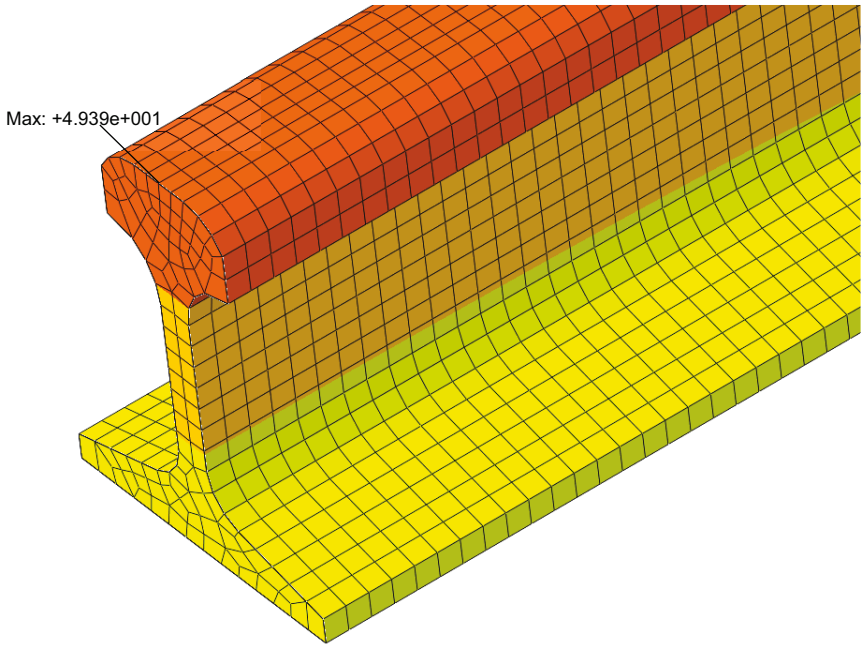

Figure 3.9. Contour plot of the rail bending stress at the maximum negative bending location from the Rail on Continuous Foundation Model (scale shown in Figure 3.8)

The contour plot of bending stress at the location corresponding to the maximum negative bending in the rail is shown in Figure 3.9. The maximum bending stress at the rail head is 49.39 MPa and occur at the middle element node of the rail head surface. The contour plot of bending stress at one of the wheel locations is shown in Figure 3.10. It can be seen that the maximum bending stress at the rail base is 95.78 MPa, which is tensile and occurs at the middle element node of the rail base.

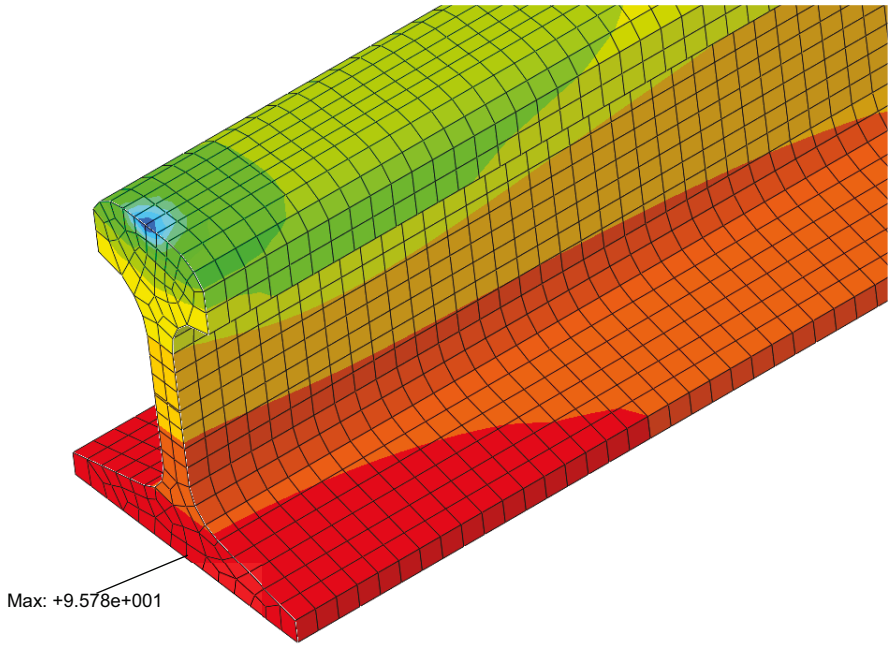

Figure 3.10. Contour plot of the rail bending stress at the wheel load location from the Rail on Continuous Foundation Model (scale shown in Figure 3.8)

3.2.2 The Rail on One layer of Discrete Spring Supports Model

The established Rail on One layer of Discrete Spring Supports Model is shown in Figure 3.11. In this model, a layer of discrete springs, as shown by the orange markers in the detail view on the upper left corner of Figure 3.11, were assigned to the bottom surface of the rail to represent the discrete supporting property of crossties under the rail. The springs were configured according to the spacing of crossties, which is taken as 0.508 m (20 in.), a typical value for wooden crossties. The stiffness of springs was uniform and transferred from the track modulus by multiplying the crosstie spacing to represent different levels of track conditions. Both the 115 RE rail and the 136 RE rail were investigated using this model.

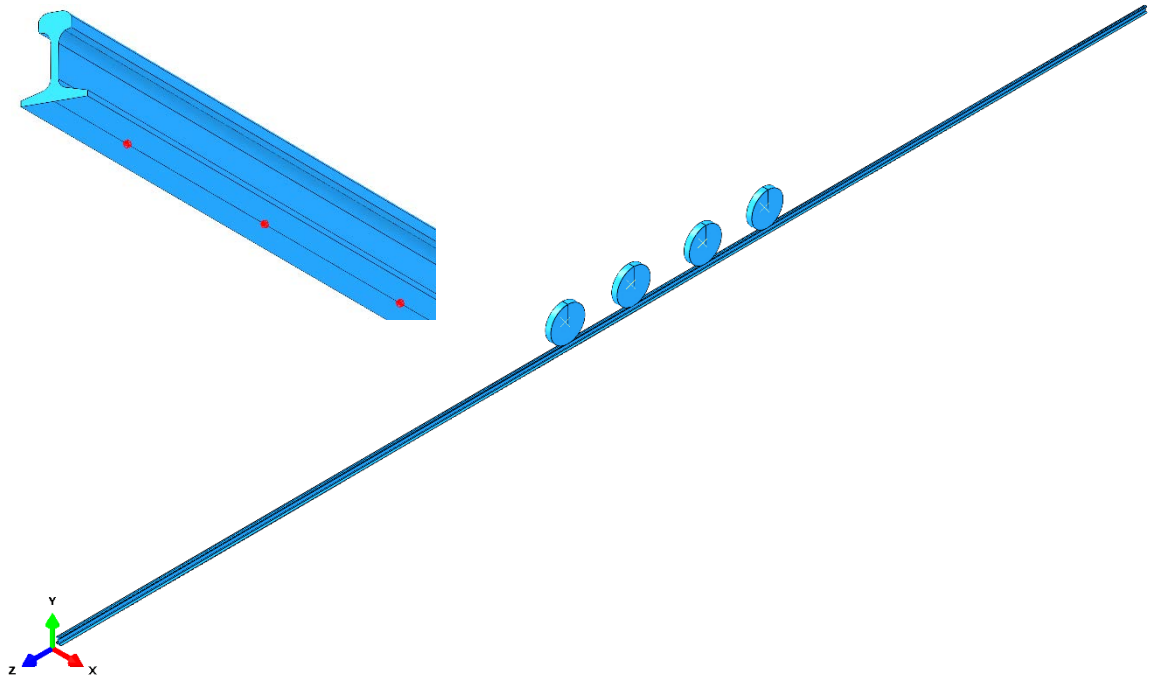

Figure 3.11. The established three dimensional Rail on One layer of Discrete Spring Supports Model and the detail view of discrete spring supports (orange markers) under the rail bottom surface (upper left corner)

The boundary conditions, wheel rail contacts, and mesh assignments in the Rail on One layer of Discrete Spring Supports Model are the same as that in the Rail on Continuous Foundation Model, thus not repeated here. The wheel loads were also symmetrically located along the rail, as shown in Figure 3.12.

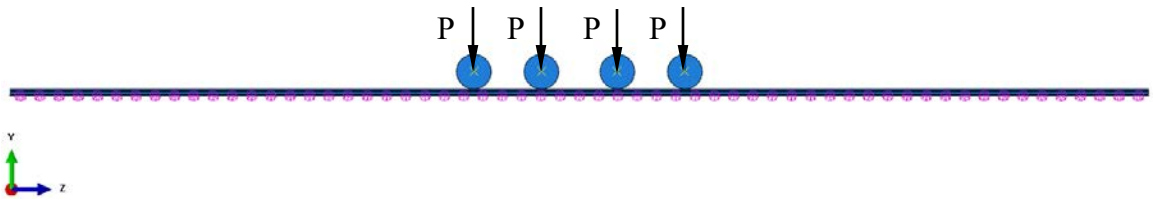

Figure 3.12. Load distribution along the rail in the Rail on One layer of Discrete Spring Supports Model

When the track modulus is 27.58 MPa and the axle spacing L1 is 2.0 m, for the 115 RE rail, the deflection response of the rail from the Rail on One layer of Discrete Spring Supports Model is shown in Figure 3.13. It shows that the maximum deflection of the rail is 6.98 mm. The bending moment response along the rail is plotted in Figure 3.14. It can

be seen that the maximum positive bending moment of the rail is 33.95 kN.m and the maximum negative bending moment is -16.99 kN.m.

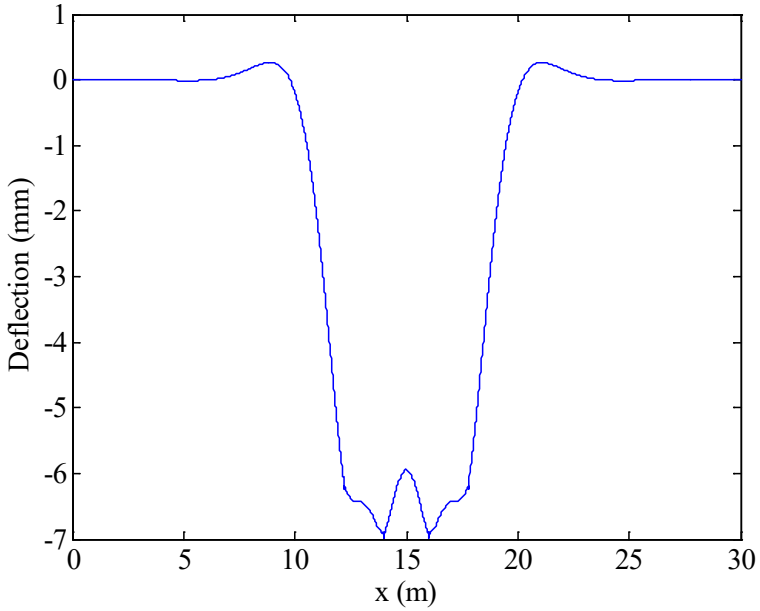

Figure 3.13. Deflection of the rail when the track modulus is 27.58 MPa at the axle spacing L1=2.0 m from the Rail on One layer of Discrete Spring Supports Model

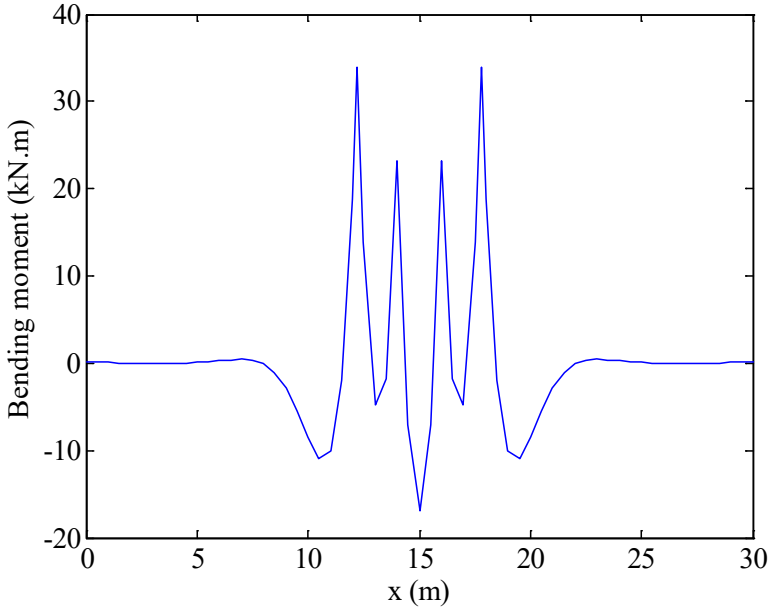

Figure 3.14. The bending moment response along the rail when the track modulus is 27.58 MPa at the axle spacing L1=2.0 m from the Rail on One layer of Discrete Spring Supports Model

The Von Mises stress distribution along the rail is shown in Figure 3.15. It shows that the maximum Von Mises stress is 390.8 MPa, which is slightly higher than that in the Rail on Continuous Foundation Model, which is 384.0 MPa. At the right corner are detail views of the Von Mises stress distribution at the outer wheel location (DO1) and inner wheel location (DO2) respectively.

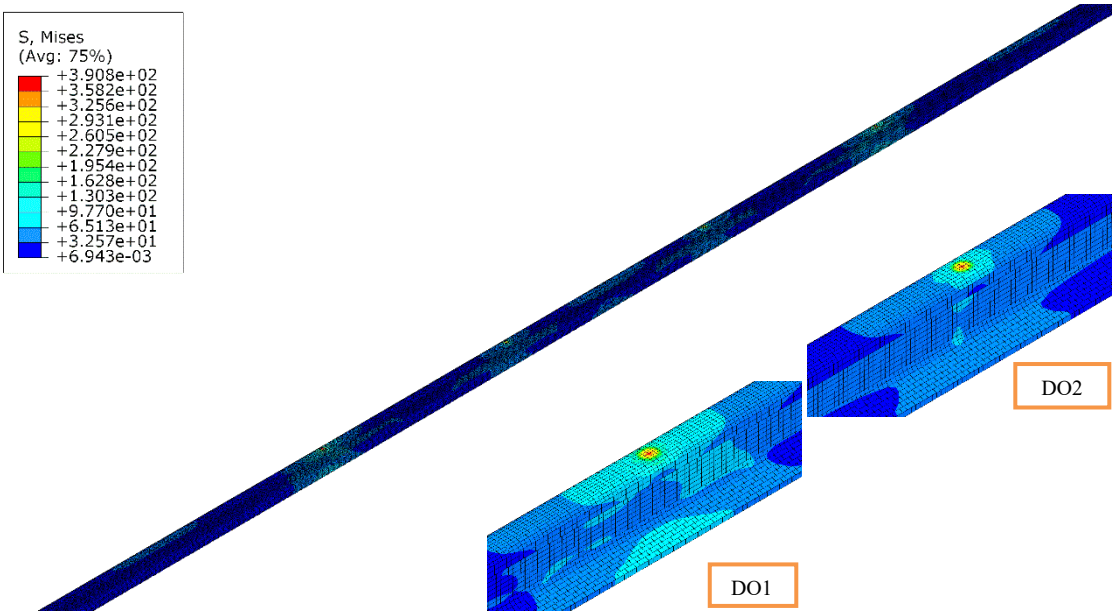

Figure 3.15. Von Mises stress distribution of the rail from the Rail on One layer of Discrete Spring Supports Model. DO1-Von Mises stress distribution of the rail at the outer wheel location; DO2-Von Mises stress distribution of the rail at the inner wheel location

The bending stress distribution of the rail is shown in Figure 3.16. The maximum bending stress is 97.39 MPa which is tensile and the minimum bending stress is -356.3 MPa, which is compression. At the right corner are detail views of the bending stress distribution at the outer wheel location (DO3) and inner wheel location (DO4) respectively.

The contour plot of bending stress at the location corresponding to the maximum negative bending in the rail is shown in Figure 3.17. The maximum bending stress at the rail head is 58.52 MPa, occurring at the middle element node of the rail head surface. The contour plot of bending stress at one of the wheel locations is shown in Figure 3.18. It can be seen that the maximum tensile stress is 97.39 MPa and it occurs at the middle element node of the rail bottom surface.

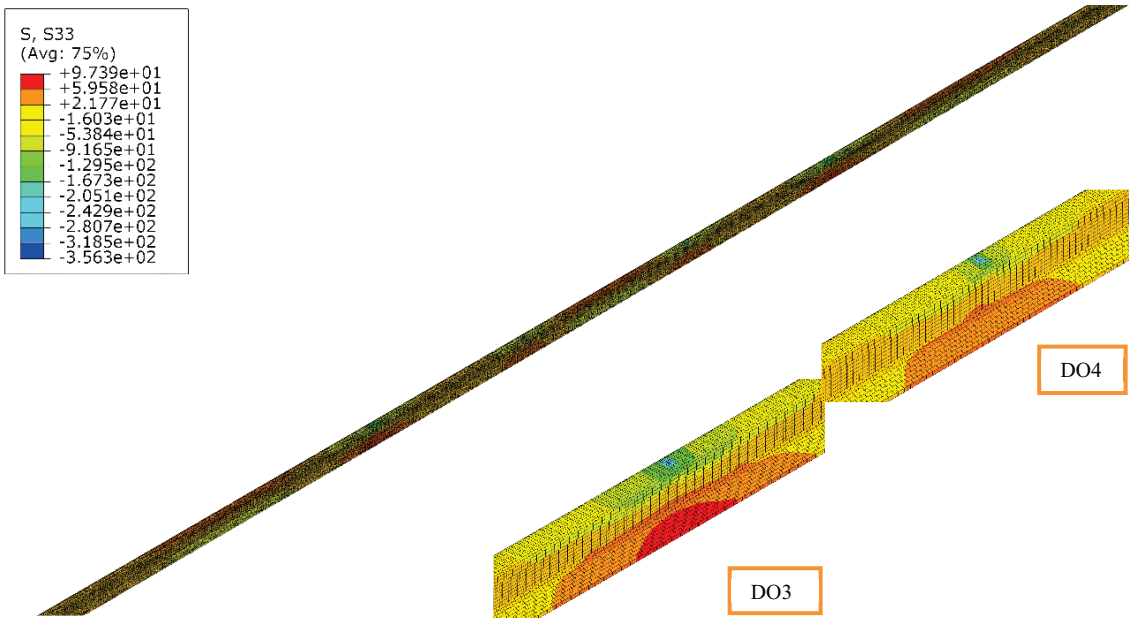

Figure 3.16. Bending stress distribution of the rail from the Rail on One layer of Discrete Spring Supports Model. DO3-Bending stress distribution of the rail at the outer wheel location; DO4-Bending stress distribution of the rail at the inner wheel location

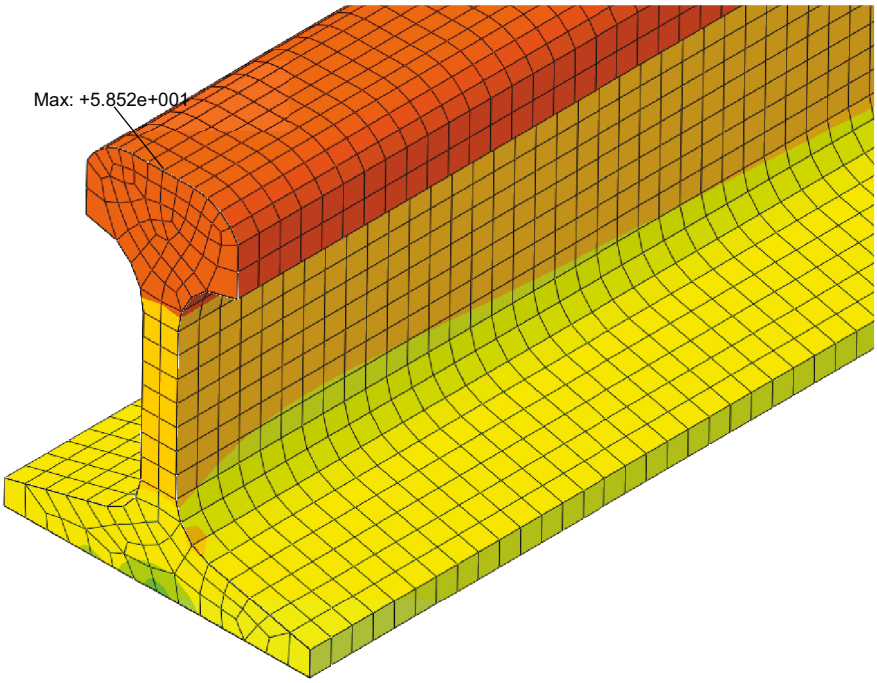

Figure 3.17. Contour plot of the rail bending stress at the maximum negative bending location from the Rail on One layer of Discrete Spring Supports Model (scale shown in Figure 3.16)

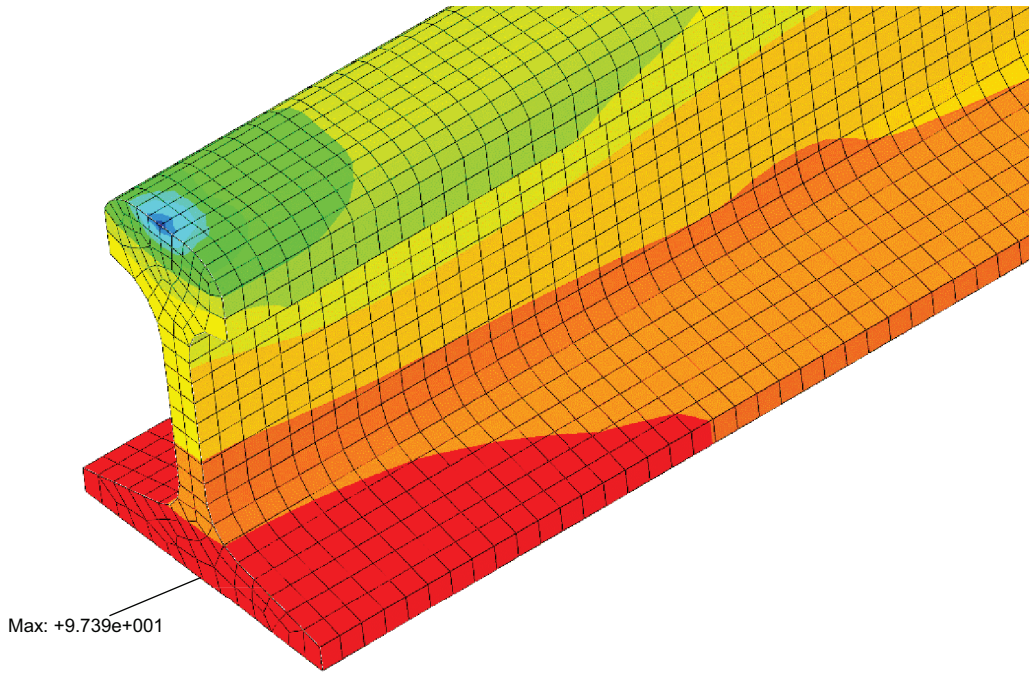

Figure 3.18. Contour plot of the rail bending stress at the wheel load location from the Rail on One layer of Discrete Spring Supports Model (scale shown in Figure 3.16)

3.2.3 The Rail on Two layers of Discrete Spring Supports Model

The established Rail on Two layers of Discrete Spring Supports Model is shown in Figure 3.19. In this type of model, crossties are modeled as solid elements and configured with a spacing of 0.508 m. The geometry and material property information of crossties are listed in Table 3.4.

A layer of discrete springs was assigned between the rail bottom surface and the top surfaces of crossties. In order to model the contact between the rail bottom surface and the crosstie surface more realistically, a 3×3 distributed spring allocation was applied to the top surface of each crosstie as shown in the detail view on the upper left corner of Figure 3.19 by magenta line and markers since the rail base width is comparable with the crosstie width. Below the crossties, another layer of discrete springs were allocated between the bottom surface of each crosstie and the ground. Similarly, to model the supports more realistically, a 3×4 distributed spring allocation was assigned (Zhao, 2011), as shown by magenta markers on the rail bottom surface in the detail view on the upper left corner of Figure 3.19.

Table 3.4. Geometry and material property information of crossties

Variable	Value
L_c (mm)	2590
W_c (mm)	229
H_c (mm)	178
E (GPa)	10
ρ_c (tonne/mm^3)	1.046×10^{-9}

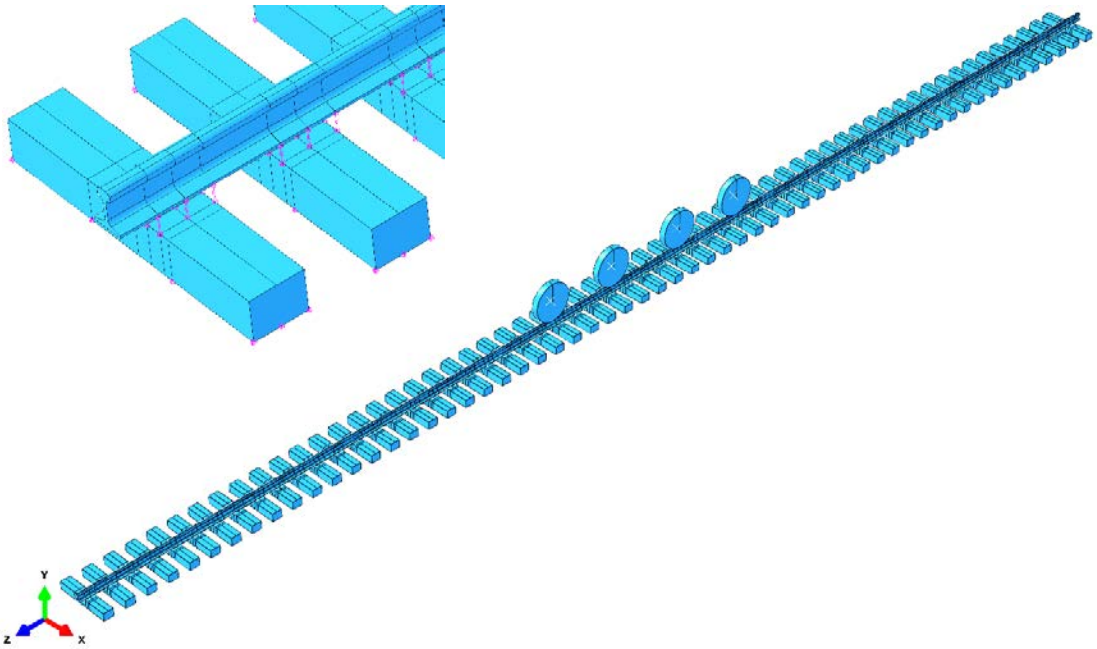

Figure 3.19. The established three dimensional Rail on Two layers of Discrete Spring Supports Model and the detail view of discrete spring supports (magenta line and markers) in the model (upper left corner)

The discrete springs located between the rail bottom surface and the top surfaces of crossties represents the fastening systems and the stiffness of each set of springs is 70,000 N/mm, a typical value for fastener stiffness in the wooden crosstie case. The stiffness of the springs between the bottom surfaces of crossties and the ground was adjusted to obtain an overall stiffness equal to each level of track modulus.

The rail material properties, mesh assignments of the rail, and wheel rail contact properties in the model are the same as that in the Rail on Continuous Foundation Model and the Rail

on One layer of Discrete Spring Supports Model, thus not repeated here. The crossties in the Rail on Two layers of Discrete Spring Supports Model were meshed with solid elements and the mesh size is 50 mm. Since the track is symmetric, half of each crosstie was modelled and symmetric boundary conditions were applied. Wheel loads were configured symmetrically along the rail as in Figure 3.20.

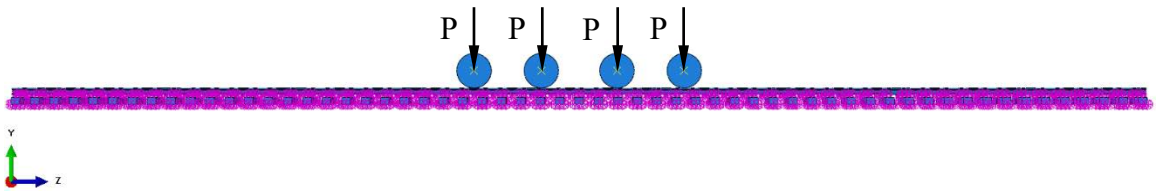

Figure 3.20. Load distribution along the rail in the Rail on Two layers of Discrete Spring Supports Model

When the track modulus is 27.58 MPa and the axle spacing L1 is 2.0 m, for the 115 RE rail, the deflection response of the rail from the Rail on Two layers of Discrete Spring Supports Model is shown in Figure 3.21. It shows that the maximum deflection of the rail is 7.41 mm. The bending moment response along the rail is shown in Figure 3.22. The maximum positive bending moment of the rail is 34.40 kN.m and the maximum negative bending moment of the rail is -15.83 kN.m.

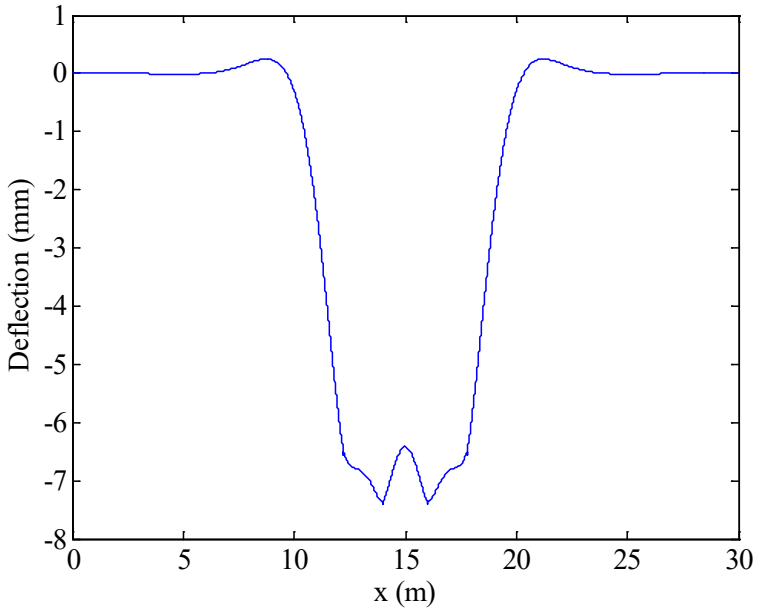

Figure 3.21. Deflection of the rail when the track modulus is 27.58 MPa at the axle spacing L1=2.0 m from the Rail on Two layers of Discrete Spring Supports Model

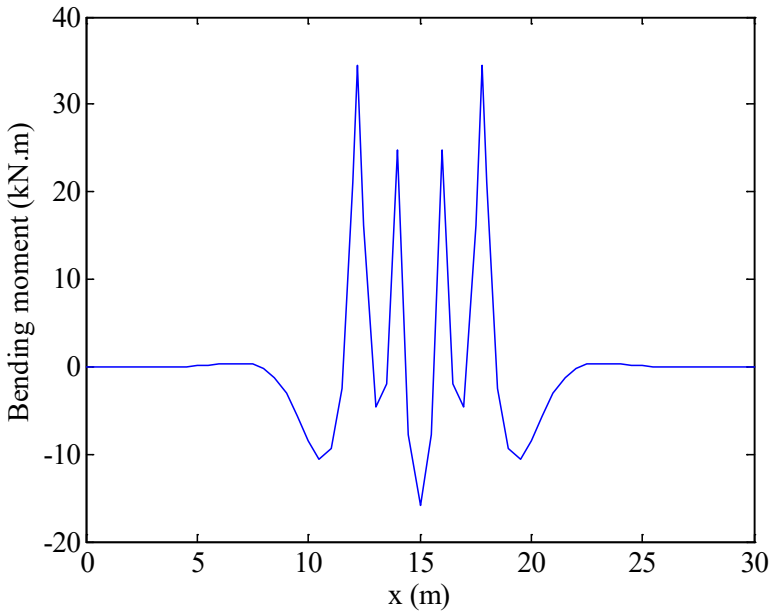

Figure 3.22. The bending moment response along the rail when the track modulus is 27.58 MPa at the axle spacing L1=2.0 m from the Rail on Two layers of Discrete Spring Supports Model

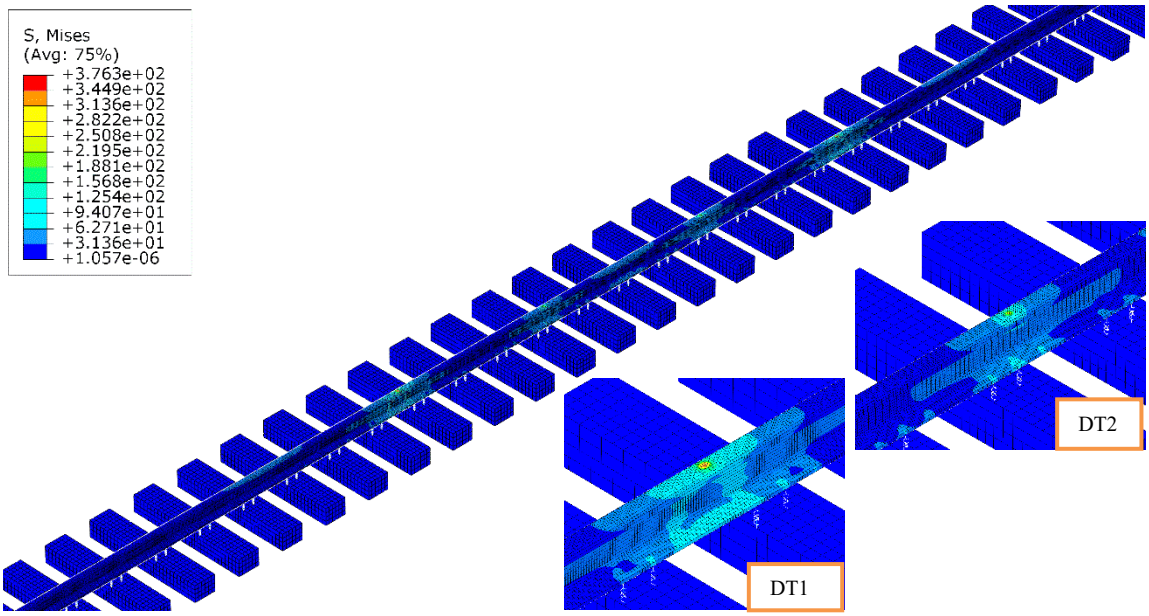

Figure 3.23. Von Mises stress distribution of the rail from the Rail on Two layers of Discrete Spring Supports Model. DT1-Von Mises stress distribution of the rail at the outer wheel location; DT2-Von Mises stress distribution of the rail at the inner wheel location

The Von Mises stress distribution of the rail is shown in Figure 3.23. It shows that the maximum Von Mises stress is 376.3 MPa. At the right corner in Figure 3.23 are detail views of the Von Mises stress distribution at the outer wheel location (DT1) and inner wheel location (DT2) respectively.

The bending stress distribution is shown in Figure 3.24. The maximum bending stress is 97.59 MPa which is tensile and the minimum bending stress is -332.2 MPa, which is compression. At the right corner of Figure 3.24 are detail views of the bending stress distribution at the outer wheel location (DT3) and inner wheel location (DT4) respectively.

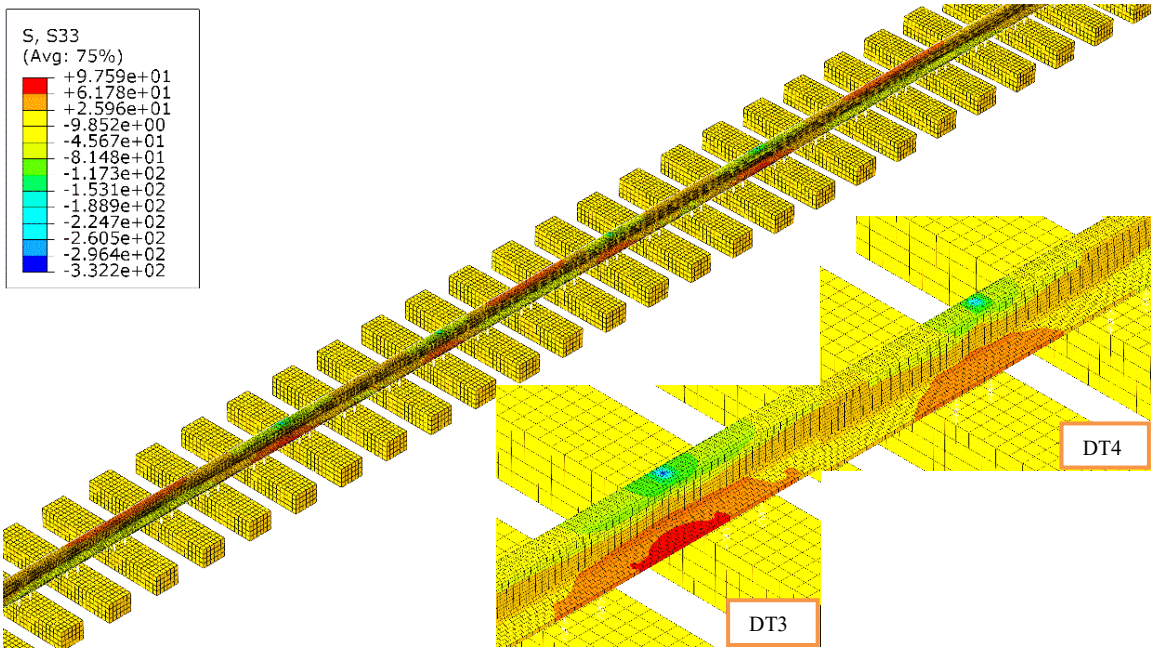

Figure 3.24. Bending stress distribution of the rail from the Rail on Two layers of Discrete Spring Supports Model. DT3-Bending stress distribution of the rail at the outer wheel location; DT4-Bending stress distribution of the rail at the inner wheel location

The contour plot of bending stress at the location corresponding to the maximum negative bending in the rail is shown in Figure 3.25. The maximum bending stress at the rail head is 53.69 MPa, occurring at the middle element node of the rail head surface. The contour plot of the rail bending stress at one of the wheel locations is shown in Figure 3.26, which indicates the location of maximum rail bending stress is at the middle element node of the rail base and the value is 97.59 MPa.

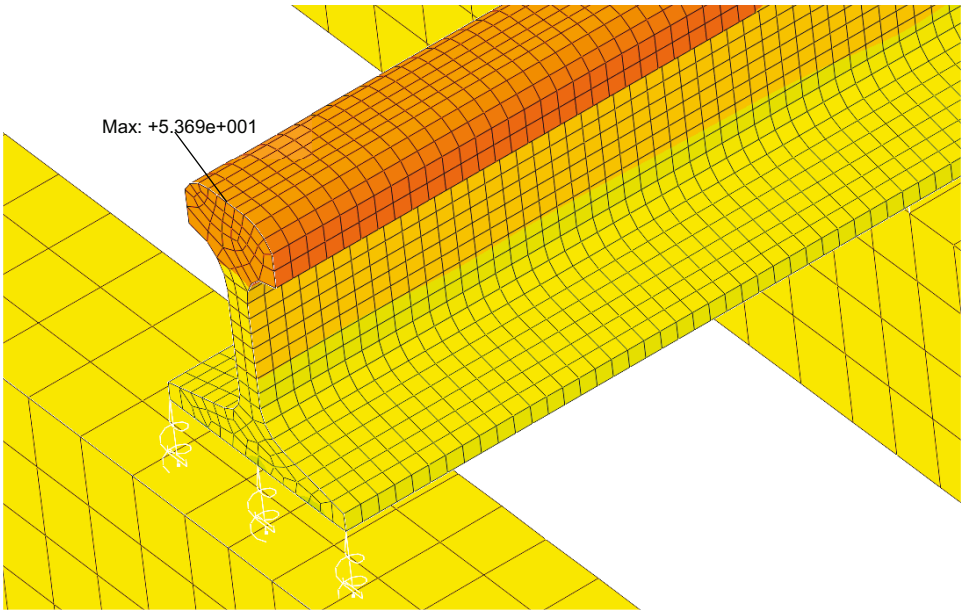

Figure 3.25. Contour plot of the rail bending stress at the maximum negative bending location from the Rail on Two layers of Discrete Spring Supports Model (scale shown in Figure 3.24)

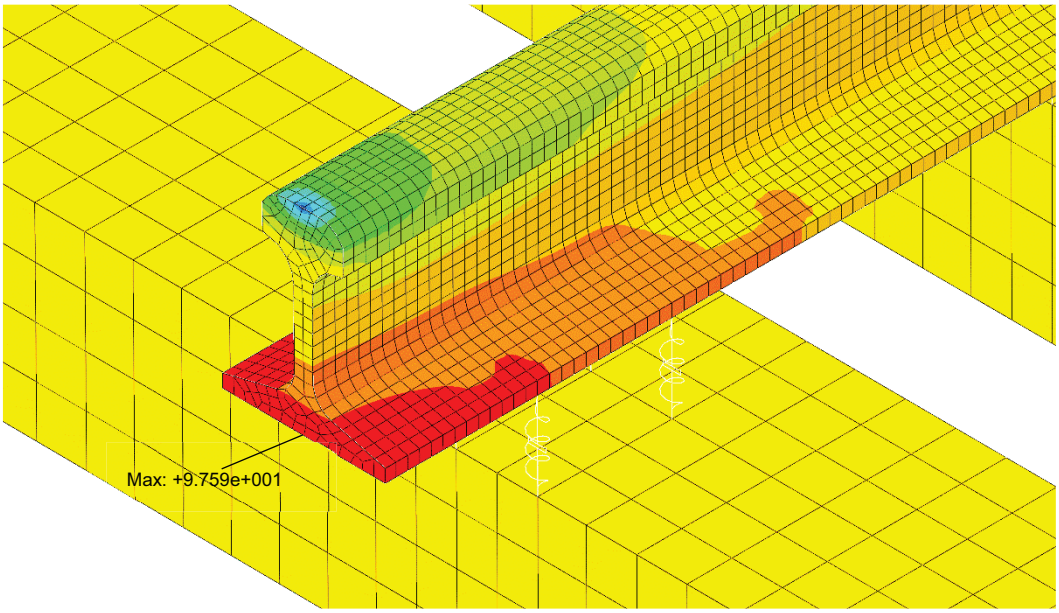

Figure 3.26. Contour plot of the rail bending stress at the wheel load location from the Rail on Two layers of Discrete Spring Supports Model (scale shown in Figure 3.24)

3.2.4 The Rail on Continuum Foundation Model

The established Rail on Continuum Foundation Model is shown in Figure 3.27. In the Rail on Continuum Foundation Model, the track components below crossties were modelled using solid elements instead of discrete springs, getting a continuum foundation which is more realistic.

Since half of the track is modelled, symmetric boundary conditions were applied to the longitudinal center plane of the continuum foundation. In addition, a fixed boundary condition was assigned to the bottom surface of the continuum foundation. The continuum foundation was composed of three layers that represent ballast, subballast and subgrade respectively. The mesh of ballast is fine since it is directly in contact with crossties and the mesh size is 100 mm. The mesh of the other two layers is non-uniform, which is less fine when the distance from crossties increases. The mesh of the rail, wheels and crossties are the same as that in the Rail on Two layers of Discrete Spring Supports Model, thus not described again here. The mesh view at the cross section for the Rail on Continuum Foundation Model is shown in Figure 3.28.

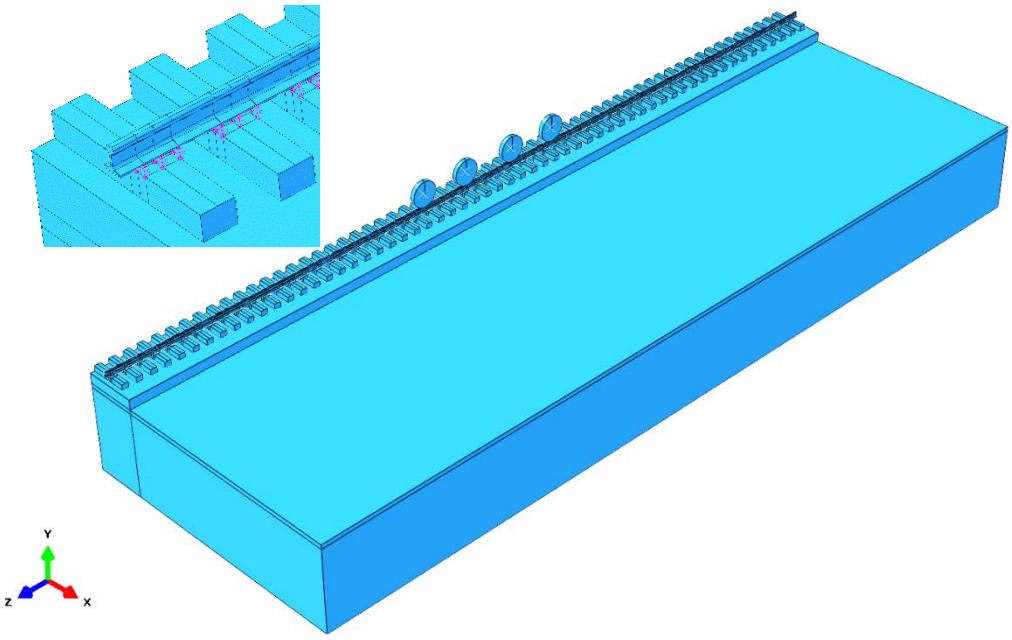

Figure 3.27. The established three dimensional Rail on Continuum Foundation Model and the detail view of the discrete spring supports between the rail bottom surface and the crosstie top surfaces (upper left corner)

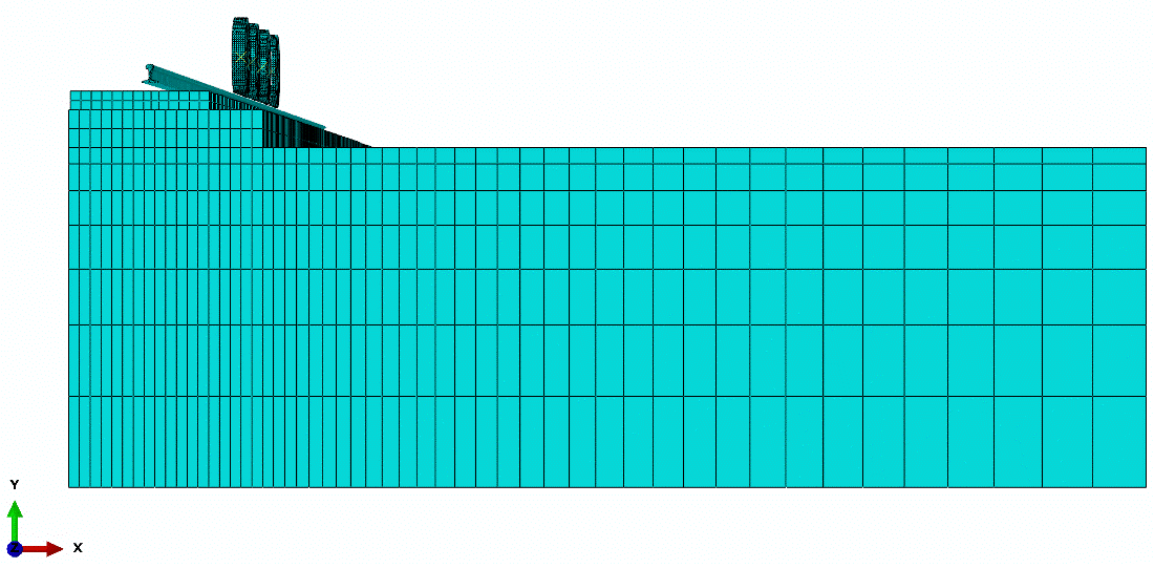

Figure 3.28. Mesh view at the cross section of the Rail on Continuum Foundation Model

A sensitivity analysis on the width and boundary condition of the continuum foundation was conducted. Three widths of the continuum foundation, 10 m, 15 m, and 20 m were used, corresponding to Model A, Model B and Model C respectively. In Model D, the foundation width is 10 m, but a symmetric boundary condition (SBC) was assigned to the outer plane of the continuum foundation. The outer plane here represents the plane parallel to the longitudinal center plane but on the other side of the continuum foundation. The results from Model A to Model D under the track modulus of 13.79 MPa are listed in Table 3.5. In Table 3.5, E1 is the error between the results from Model B and Model C. It can be seen that, when the foundation width increases from 15 m to 20 m, the solution is already convergent. E2 is the error between the results of Model A and Model C, which shows that for stress parameters, the results from the model with 10 m width foundation are quite close to that from the model with 20 m width foundation, with a maximum error of 0.26%. However, for deflection response, the error is 9.54%. E3 is the error between the results of Model D and Model C, which shows that the stress response also does not vary much when the symmetric boundary condition was added to the outer plane of the continuum foundation, with a maximum error of 0.27%. In addition, the error of deflection results is larger, which is -5.74%.

Table 3.5. Sensitivity analysis results from the Rail on Continuum Foundation Model for U=13.79 MPa

Parameter	Model A	Model B	Model C	Model D	E1 (%)	E2 (%)	E3 (%)
Width of foundation (m)	10	15	20	10			
SBC on the outer plane	N	N	N	Y			
Von Mises stress (MPa)	376.60	376.60	376.60	376.60	0.00	0.00	0.00
Maximum bending stress at the rail head (MPa)	70.66	70.71	70.71	70.90	0.00	-0.07	0.27
Maximum bending stress at the rail base (MPa)	116.00	115.70	115.70	115.60	0.00	0.26	-0.09
Mean bending stress at the rail head (MPa)	59.74	59.89	59.79	59.95	0.17	-0.08	0.27
Maximum deflection (mm)	12.40	11.13	11.32	10.67	-1.68	9.54	-5.74

Table 3.6 and Table 3.7 below are the sensitivity analysis results from the Rail on Continuum Foundation Model under the track modulus of 27.58 MPa and 41.37 MPa, respectively. Similar conclusions can be obtained from the results in Table 3.6 and Table 3.7 with that from Table 3.5. For example, when the continuum foundation width increases from 15 m to 20 m, the solution is already convergent, indicated by a maximum error of 0.00% under the track modulus of 27.58 MPa and 0.01% under the track modulus of 41.37 MPa shown in E1 columns.

The E2 columns show that, for stress parameters, the results from the 10 m width foundation model and the 20 m width foundation model are quite close, with a maximum error of -0.15% under the track modulus of 27.58 MPa and 0.10% under the track modulus of 41.37 MPa. For deflection, the error is larger, 7.17% and 1.34%, respectively.

The E3 columns indicate that, for stress parameters, the results from the 10 m width foundation model and the model with symmetric boundary condition on the outer plane of the continuum foundation are also quite close, with a maximum error of 0.21% for the track modulus of both 27.58 MPa and 41.37 MPa. For deflection results, the error is -3.24% and -3.21% respectively.

Table 3.6. Sensitivity analysis results from the Rail on Continuum Foundation Model for *U*=27.58 MPa

Parameter	Model A	Model B	Model C	Model D	E1 (%)	E2 (%)	E3 (%)
Width of foundation (m)	10	15	20	10			
SBC on the outer plane	N	N	N	Y			
Von Mises stress (MPa)	375.60	375.60	375.60	375.60	0.00	0.00	0.00
Maximum bending stress at the rail head (MPa)	38.69	38.69	38.69	38.77	0.00	0.00	0.21
Maximum bending stress at the rail base (MPa)	97.66	97.54	97.54	97.49	0.00	0.12	-0.05
Mean bending stress at the rail head (MPa)	32.71	32.76	32.76	32.78	0.00	-0.15	0.06
Maximum deflection (mm)	6.28	5.86	5.86	5.67	0.00	7.17	-3.24

Table 3.7. Sensitivity analysis results from the Rail on Continuum Foundation Model for *U*=41.37 MPa

Parameter	Model A	Model B	Model C	Model D	E1 (%)	E2 (%)	E3 (%)
Width of foundation (m)	10	15	20	10			
SBC on the outer plane	N	N	N	Y			
Von Mises stress (MPa)	375.60	375.60	375.60	375.60	0.00	0.00	0.00
Maximum bending stress at the rail head (MPa)	28.16	28.15	28.15	28.21	0.00	0.04	0.21
Maximum bending stress at the rail base (MPa)	91.74	91.66	91.65	91.62	0.01	0.10	-0.03
Mean bending stress at the rail head (MPa)	23.88	23.87	23.87	23.92	0.00	0.04	0.21
Maximum deflection (mm)	4.55	4.49	4.49	4.35	0.00	1.34	-3.12

When comparing the results from Table 3.5 to Table 3.7 together, it shows that, with the track modulus increasing, the error of deflection results indicates a pattern of decreasing, i.e. an error of 9.54% under the track modulus of 13.79 MPa, 7.17% under the track

modulus of 27.58 MPa, and 1.34% under the track modulus of 41.37 MPa. This pattern indicates that when the track becomes harder, the deflection response is less sensitive to the width and boundary conditions on the outer plane of the continuum foundation.

The main focus in our thesis is on the rail bending stress behavior; thus, Model A with a 10 m width foundation is suitable for our investigation, since it can achieve sufficient accuracy and meanwhile, be more time and cost effective.

The Poisson's ratio for the continuum foundation is 0.49. Under a single wheel load, the Young's modulus of the continuum foundation is adjusted to produce an overall stiffness equivalent to each level of track modulus. Figure 3.29 and Figure 3.30 provide examples for the comparison of the deflection and bending moment responses along the rail under the track modulus of 27.58 MPa from the Rail on Continuum Foundation Model and other types of models including the Winkler model results.

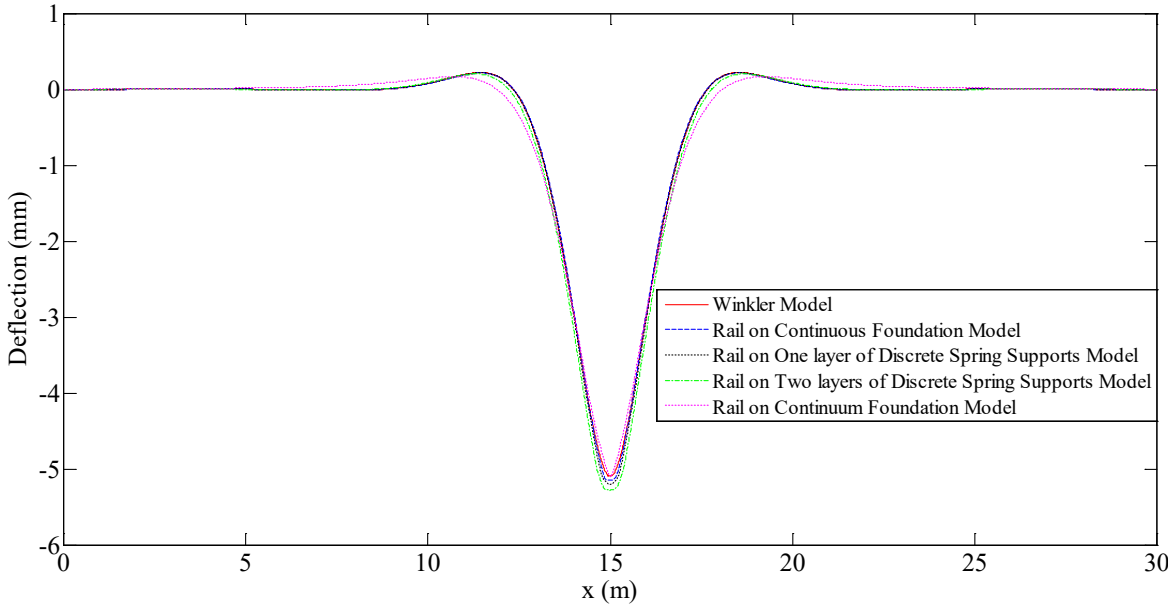

Figure 3.29. The deflection responses of the rail from different types of models under the track modulus of 27.58 MPa

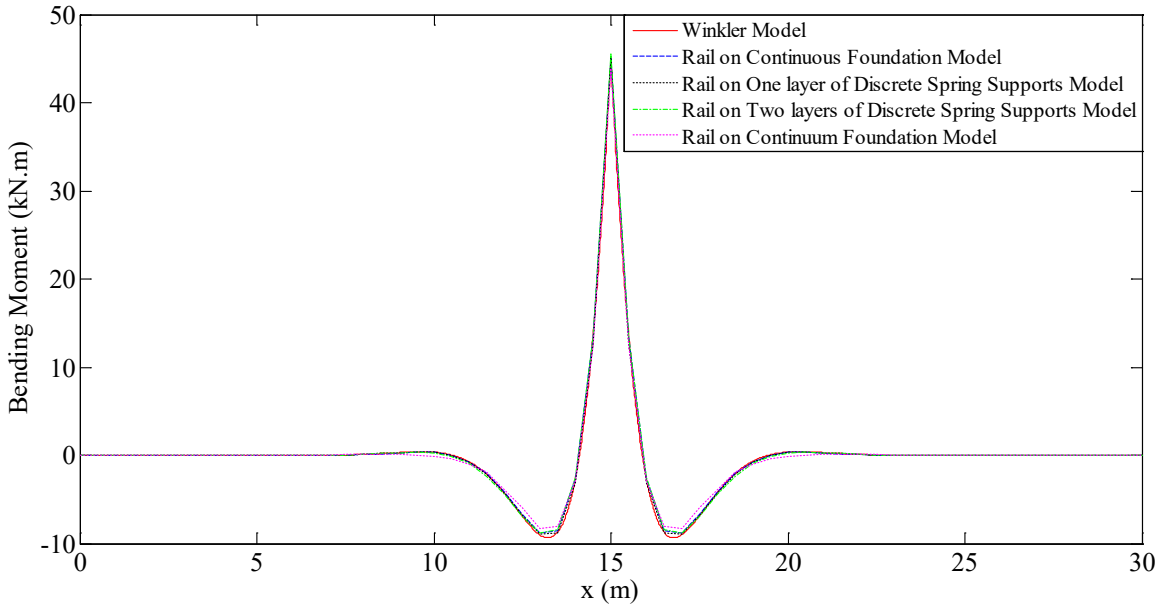

Figure 3.30. The bending moment responses of the rail from different types of models under the track modulus of 27.58 MPa

From Figure 3.29 and Figure 3.30, it can be seen that, the deflection and bending moment responses along the rail from the Rail on Continuum Foundation Model match well with that from all other types of models, indicating that the Rail on Continuum Foundation Model has an equivalent track modulus of 27.58 MPa as in other types of models. For the track modulus of 13.79 MPa and 41.37 MPa, the Young's modulus of the continuum foundation was adjusted in the same way and will not be repeated here.

In the Rail on Continuum Foundation Model, the wheel loads were configured along the rail as shown in Figure 3.31.

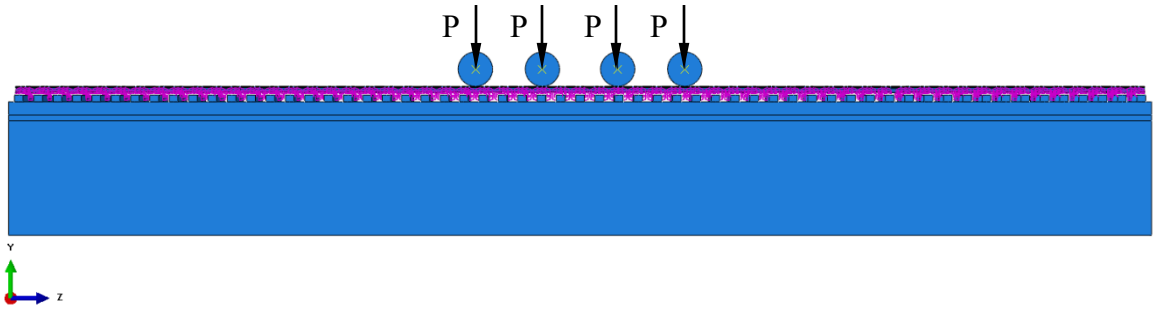

Figure 3.31. Load distribution along the rail in the Rail on Continuum Foundation Model

Under the track modulus is 27.58 MPa, when the axle spacing L1 is 2.0 m, for the 115 RE rail, the deflection response along the rail from the Rail on Continuum Foundation Model is shown in Figure 3.32. The maximum deflection of the rail is 6.63 mm.

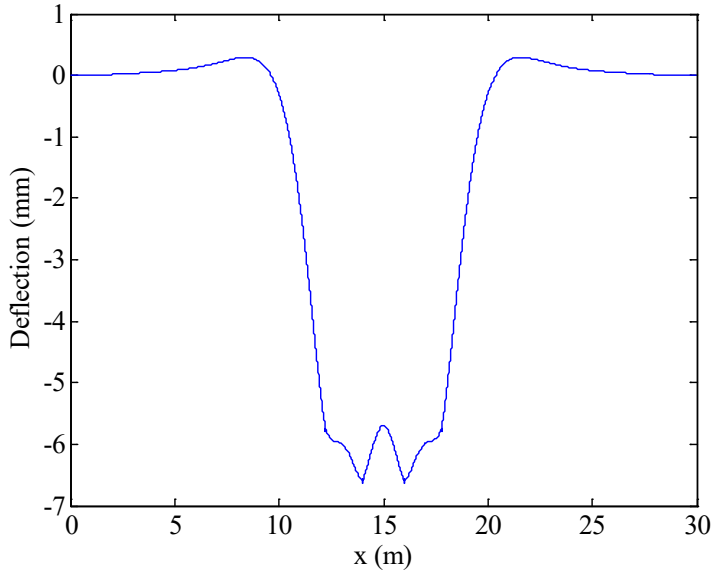

Figure 3.32. Deflection of the rail when the track modulus is 27.58 MPa at the axle spacing L1=2.0 m from the Rail on Continuum Foundation Model

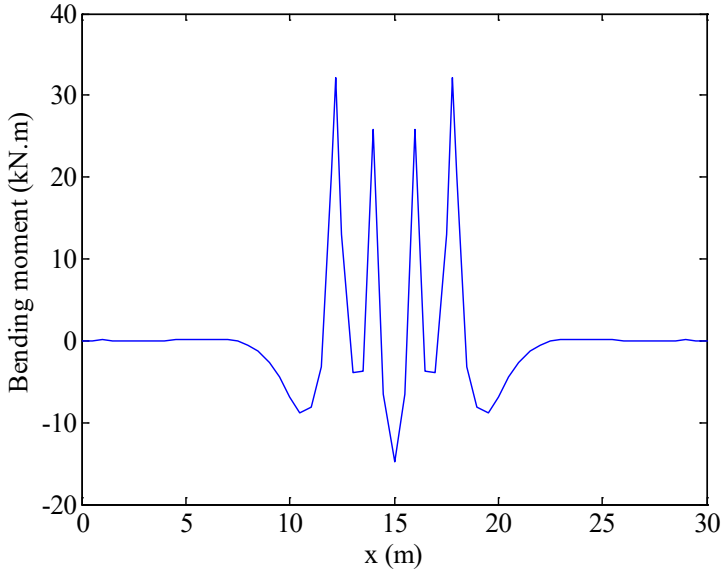

Figure 3.33. The bending moment distribution along the rail when the track modulus is 27.58 MPa at the axle spacing L1=2.0 m from the Rail on Continuum Foundation Model

The bending moment response along the rail is shown in Figure 3.33. The maximum positive bending moment of the rail is 32.11 kN.m and the maximum negative bending moment of the rail is -14.76 kN.m.

The Von Mises stress distribution along the rail is shown in Figure 3.34. It can be seen that the maximum Von Mises stress of the rail is 375.6 MPa. At the right corner in Figure 3.34 are detail views of the Von Mises stress distribution of the rail at the outer wheel location (DC1) and inner wheel location (DC2) respectively.

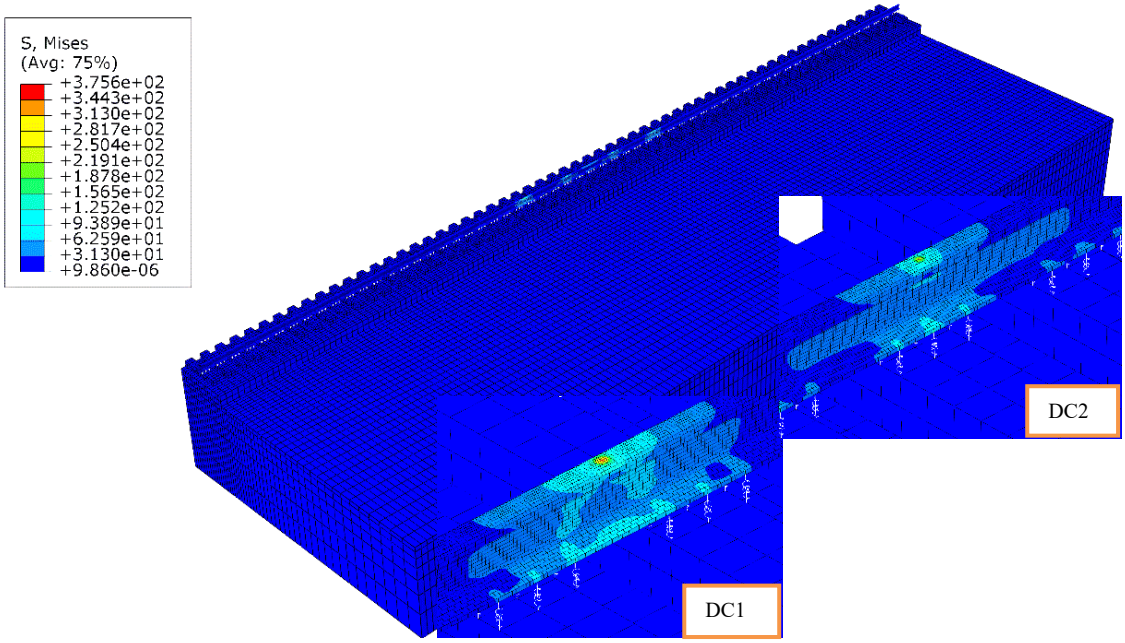

Figure 3.34. Von Mises stress distribution of the rail from the Rail on Continuum Foundation Model. DC1-Von Mises stress distribution of the rail at the outer wheel location; DC2-Von Mises stress distribution of the rail at the inner wheel location

The bending stress distribution along the rail is shown in Figure 3.35. The maximum bending stress of the rail is 91.30 MPa which is tensile and the minimum bending stress of the rail is -324.4 MPa, which is compression. At the right corner in Figure 3.35 are detail views of the bending stress distribution of the rail at the outer wheel location (DC3) and inner wheel location (DC4) respectively.

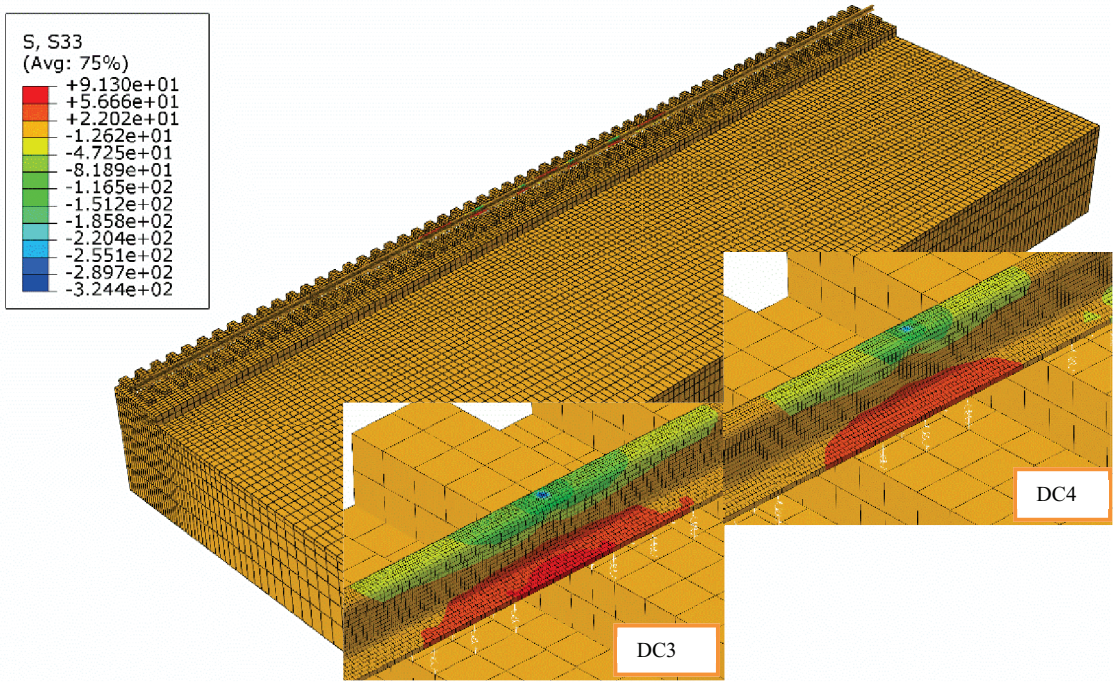

Figure 3.35. Bending stress distribution of the rail from the Rail on Continuum Foundation Model. DC3-Bending stress distribution of the rail at the outer wheel location; DC4-Bending stress distribution of the rail at the inner wheel location

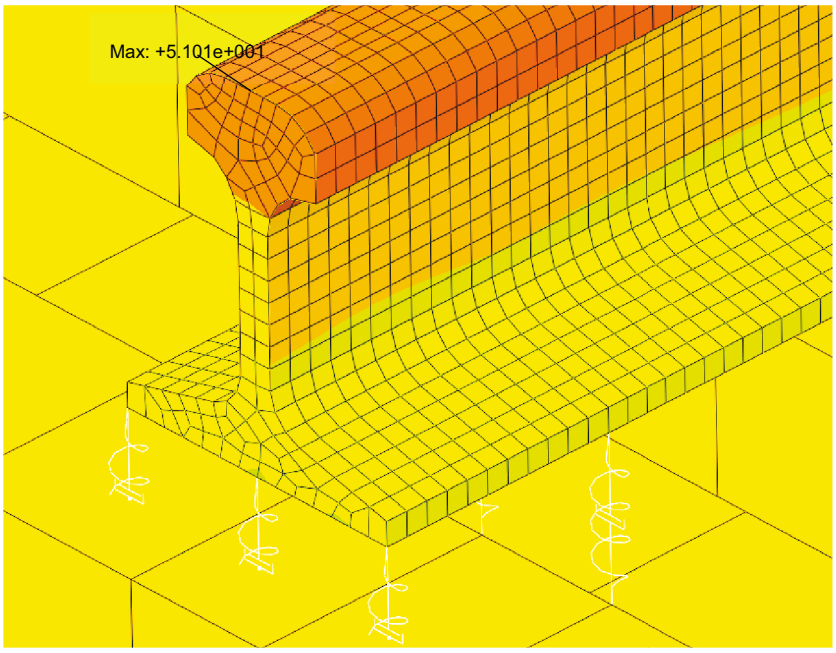

Figure 3.36. Contour plot of the rail bending stress at the maximum negative bending location from the Rail on Continuum Foundation Model (scale shown in Figure 3.35)

The contour plot of bending stress at the location corresponding to the maximum negative bending in the rail is shown in Figure 3.36. The maximum bending stress at the rail head is 51.01 MPa, occurring at the middle element node of the rail head surface. The contour plot of bending stress at one of the wheel locations is shown in Figure 3.37 and the maximum tensile stress of the rail is 91.30 MPa, occurring at the middle element node of the rail base.

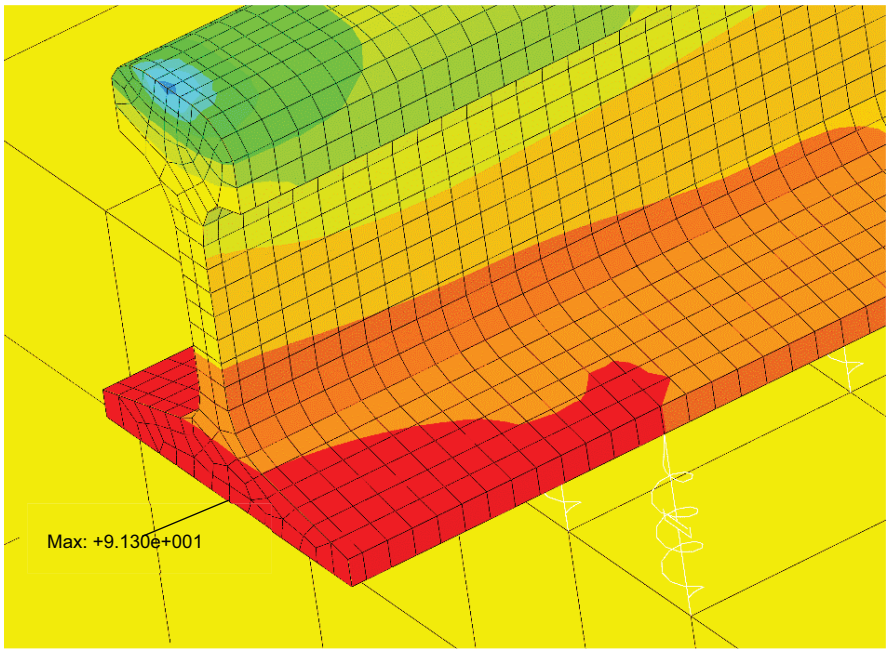

Figure 3.37. Contour plot of the rail bending stress at the wheel load location from the Rail on Continuum Foundation Model (scale shown in Figure 3.35)

3.3 Model validation and comparison

From the Winkler model, the deflection and bending moment responses of the rail can be obtained using Equation 2.2 to Equation 2.4. Under four wheel loads, when the axle spacing L1 is 2.0 m, the deflection responses of the rail from the Winkler model and four types of finite element models described in the Section 3.2 at each track modulus are shown in Figure 3.38 below in which the horizontal axis is the longitudinal coordinate along the rail. From Figure 3.38, it shows that, under each track modulus, the deflection responses from the Winkler model, the Rail on Continuous Foundation Model, the Rail on One layer of Discrete Spring Supports Model and the Rail on Continuum Foundation Model all match well both in shape and values. However, the Rail on Two layers of Discrete Spring

Supports Model seems to produce higher deflections than other types of models, which is reasonable since the crossties are modelled using deformable bodies in the Rail on Two layers of Discrete Spring Supports Model, making the system more flexible. The comparison of the deflection responses under each track modulus from different types of models when the axle spacing L1 varies show similar phenomenon, thus will not be repeated here.

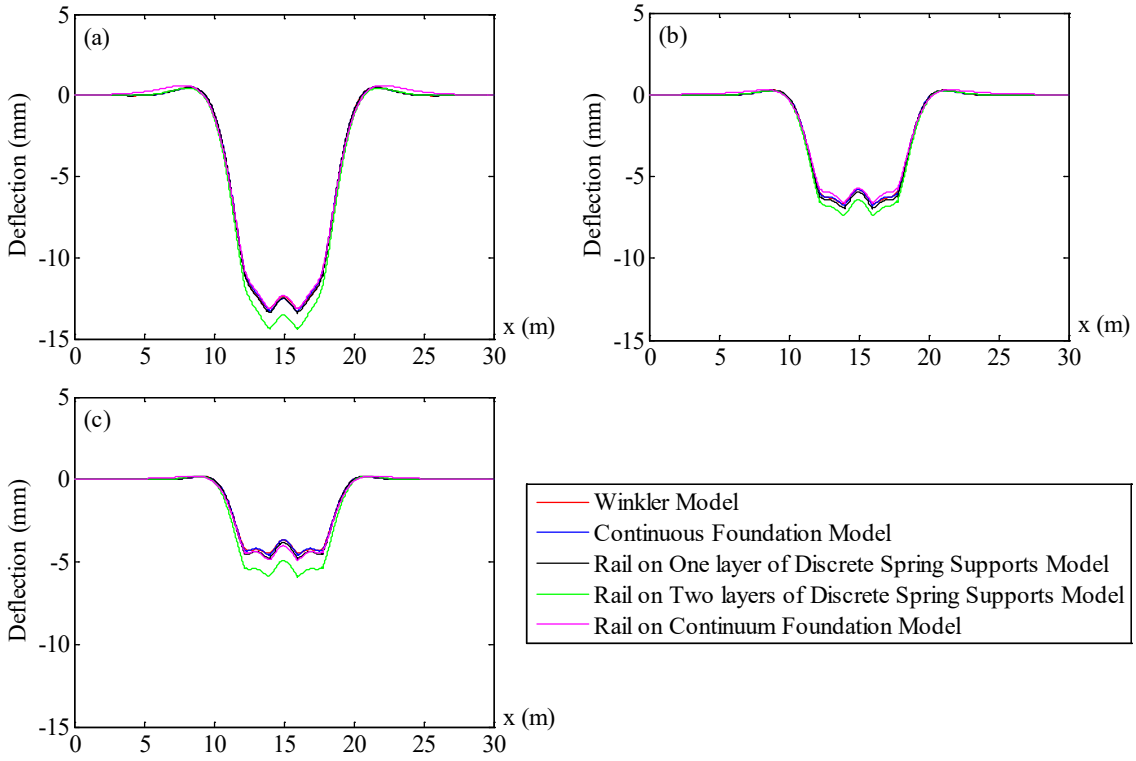

Figure 3.38. Deflection of the rail from different types of models at the axle spacing L1=2.0 m under the track modulus of (a) U=13.79 MPa (b) U=27.58 MPa and (c) U=41.37 MPa

Under four wheel loads, at the axle spacing L1 of 2.0 m, the bending moment responses of the rail from the Winkler model and four types of finite element models under each track modulus are shown in Figure 3.39. It can be seen that, at each track modulus, the bending moment responses from the Winkler model, the Rail on Continuous Foundation Model, the Rail on One layer of Discrete Spring Supports Model, the Rail on Two layers of Discrete Spring Supports Model, and the Rail on Continuum Foundation model all match well. The comparison of the bending moment responses under each track modulus from different

types of models when the axle spacing L1 varies shows similar phenomenon and thus will not be repeated here.

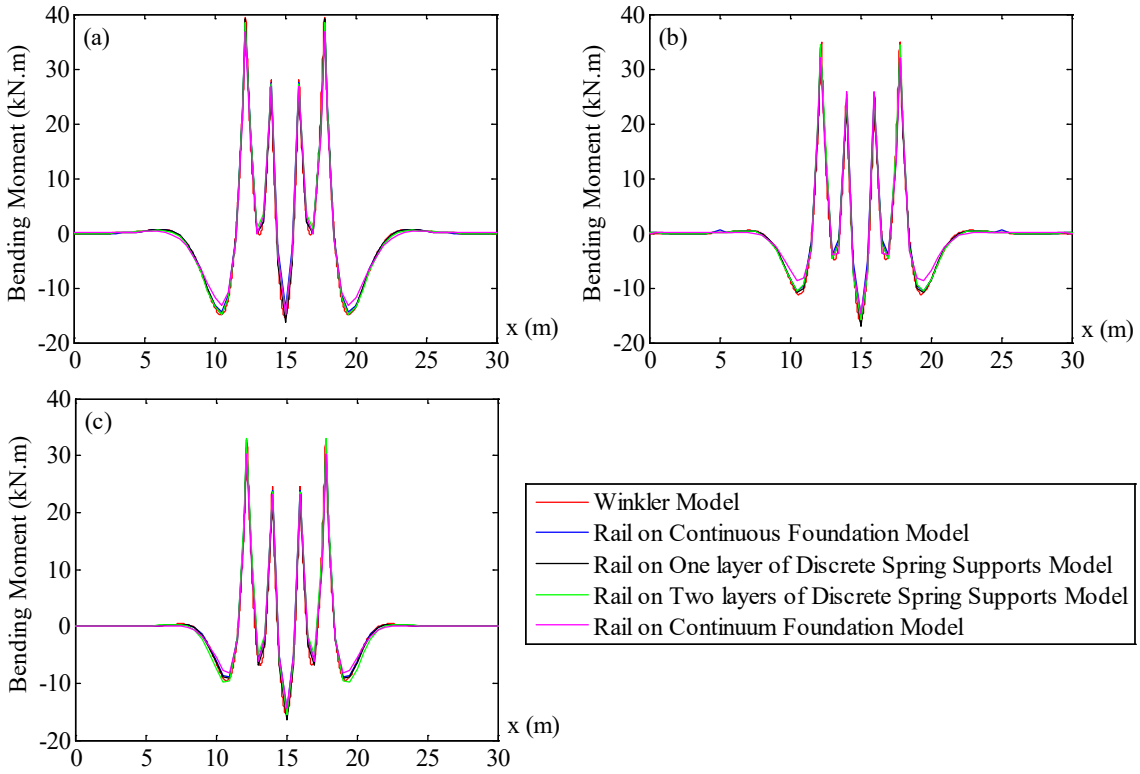

Figure 3.39. The bending moment responses of the rail from different types of models at the axle spacing L1=2.0 m under the track modulus of (a) U=13.79 MPa (b) U=27.58 MPa and (c) U=41.37 MPa

3.4 Establishment of the railway track system model when relative locations of wheel loads to crossties vary

In our former models described in Section 3.2, the wheel loads are configured symmetrically in the longitudinal direction of the rail. However, the relative locations of wheel loads to crossties may also have effects on the rail bending stress behaviour. For example, when the track modulus is 27.58 MPa and under one wheel load, the deflection responses along the rail when the wheel load is applied right above the crosstie (Case 1) and in the middle of the crosstie span (Case 2) are shown in Figure 3.40 as follows. Figure 3.40 shows that the deflections in Case 1 and Case 2 are quite close while the maximum

deflection in Case 2, which is 5.29 mm, is slightly larger than that in Case 1, which is 5.20 mm, with a difference of 0.09 mm.

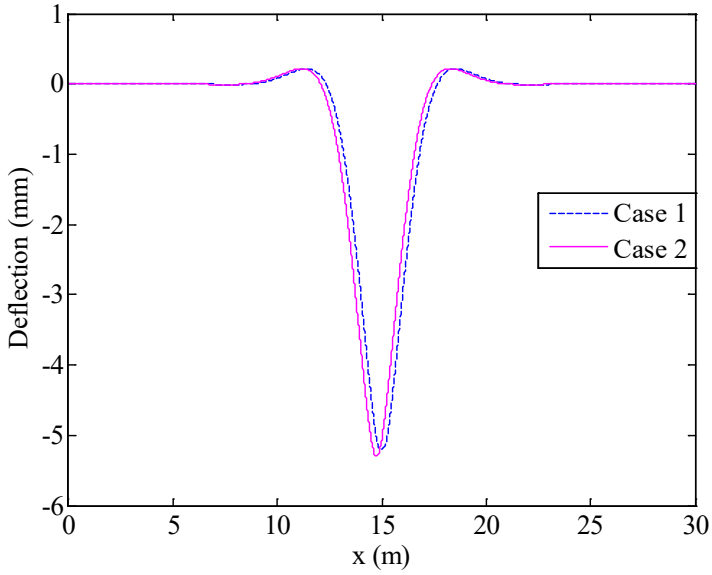

Figure 3.40. Comparison of the deflection of the rail in Case 1 (wheel load applied right above the crosstie) and Case 2 (wheel load applied at the middle of the crosstie span) from the Rail on One layer of Discrete Spring Supports Model

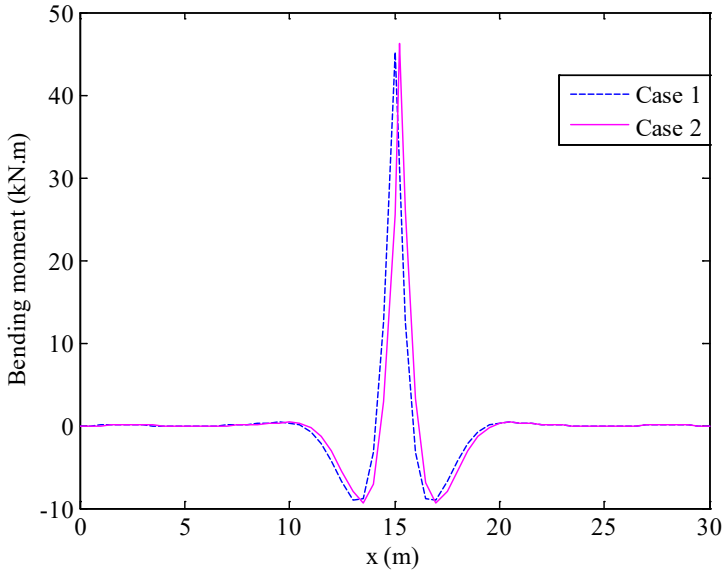

Figure 3.41. Comparison of the bending moment responses along the rail in Case 1 (wheel load applied right above the crosstie) and Case 2 (wheel load applied at the middle of the crosstie span) from the Rail on One layer of Discrete Spring Supports Model

Under the track modulus of 27.58 MPa, the bending moment responses along the rail in Case 1 and Case 2 are shown in Figure 3.41. From Figure 3.41, it can be seen that, for both cases, the bending moment responses along the rail are quite close. However, the peak moment in Case 2 is 46.25 MPa, which is slightly larger than that in Case 1, which is 45.18 MPa, with a difference of 1.07 kN.m. This difference indicates that a larger bending moment can be obtained when the wheel load is applied in the middle of the crosstie span than when the wheel load is applied right on the crosstie. In addition, the maximum bending stress at the rail head in Case 1 is 30.69 MPa, lower than that in Case 2 which is 31.52 MPa, with a difference of 0.83 MPa. The maximum bending stress at the rail base in Case 1 is 117.5 MPa lower than that in Case 2, which is 124.5 MPa, with a difference of 7 MPa.

From the above results, we can see that, when the wheel load is applied at different relative locations to crossties, the rail bending responses can vary. To consider how the relative locations of wheel loads to crossties will influence the rail bending stress behaviour, a finite element analysis was conducted using the Rail on One layer of Discrete Spring Supports Model, which can represent the discrete property of crossties under the rail and meanwhile is efficient in calculation. In the model, wheel loads were moved along the rail to get different relative locations of wheel loads to crossties and a section of 10 m in the middle of the rail was used for latter data analysis.

3.5 Establishment of the railway track system model when wheel loads are applied at the rail gauge corner

Due to the geometry property of the rail and the wheel, the wheel load location is usually deviated from the middle point of the rail head surface, which can bring lateral bending and torsional bending to the rail apart from the dominant bending component in the vertical direction, as described in Section 2.3. Considering this, a finite element model analysis in which wheel loads are applied at the rail gauge corner was conducted; thus lateral and torsional loads will be introduced into the rail. The established finite element model is shown in Figure 3.42.

The material properties, mesh properties, boundary conditions and other parameters are the same as that in the Rail on Continuous Foundation Model described in Section 3.2.1, thus not repeated here. The wheels were sketched based on the profile of D36 wheel commonly

used in heavy haul railways of North America. The shape of the wheel surface in contact with the rail is a cone, as shown in the detail view on the up left corner in Figure 3.42.

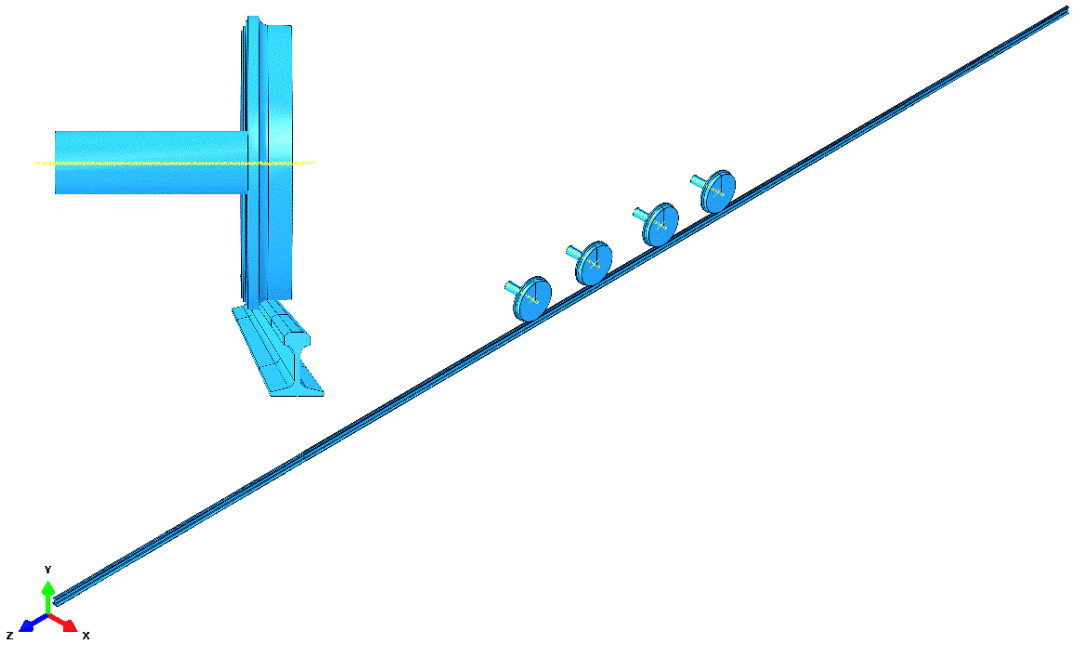

Figure 3.42. The established three dimensional Rail on Continuous Foundation Model with wheel loads applied at the rail gauge corner and the detail view of wheel rail configuration (upper left corner)

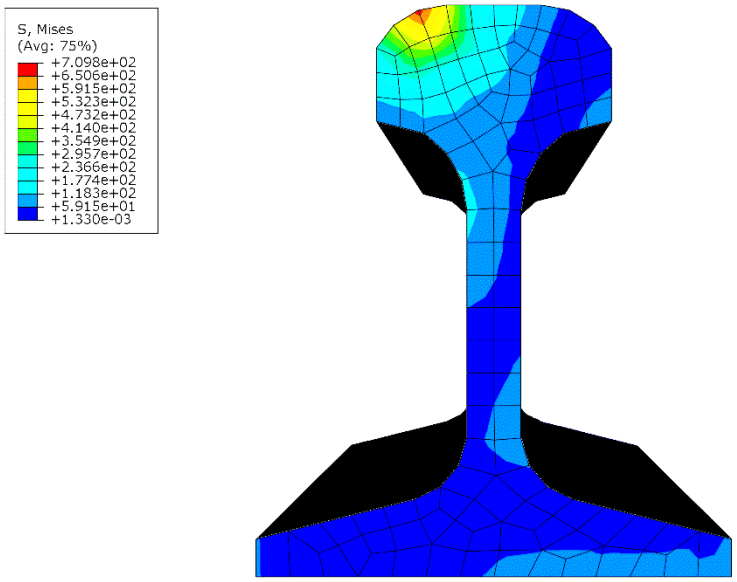

Figure 3.43. The Von Mises stress distribution at the rail cross section from the Rail on Continuous Foundation Model with wheel loads applied at the rail gauge corner

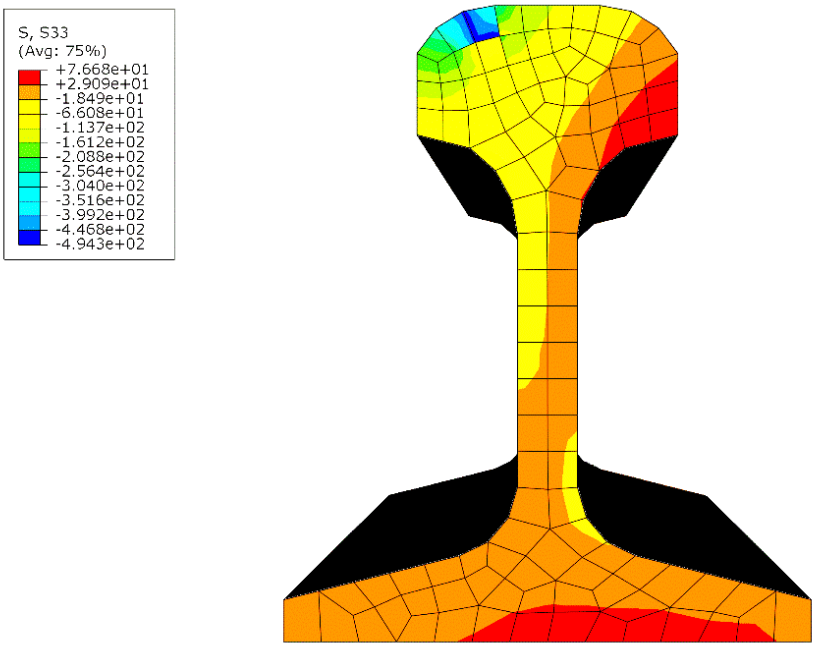

Figure 3.44. The bending stress distribution at the rail cross section from the Rail on Continuous Foundation Model with wheel loads applied at the rail gauge corner

Under the track modulus of 27.58 MPa and at the axle spacing L1 of 2.0 m, the Von Mises stress distribution of the rail is shown in Figure 3.43. It can be seen that, the maximum Von Mises stress occurs at the rail gauge corner area instead of the middle area at the top layer of the rail head.

The bending stress distribution at the rail cross section is shown in Figure 3.44, which indicates that the maximum bending stresses at the rail head and rail base occur at one side of the rail cross section instead of at the middle area of the rail head and rail base.

Under the track modulus of 27.58 MPa, when the axle spacing is 2.0 m, the deflection and bending moment responses along the rail are shown in Figure 3.45 and Figure 3.46 respectively. In Figure 3.45, the maximum deflection is 6.67 mm. In Figure 3.46, the maximum positive bending moment is 21.92 kN.m and the maximum negative bending moment is -6.27 kN.m.

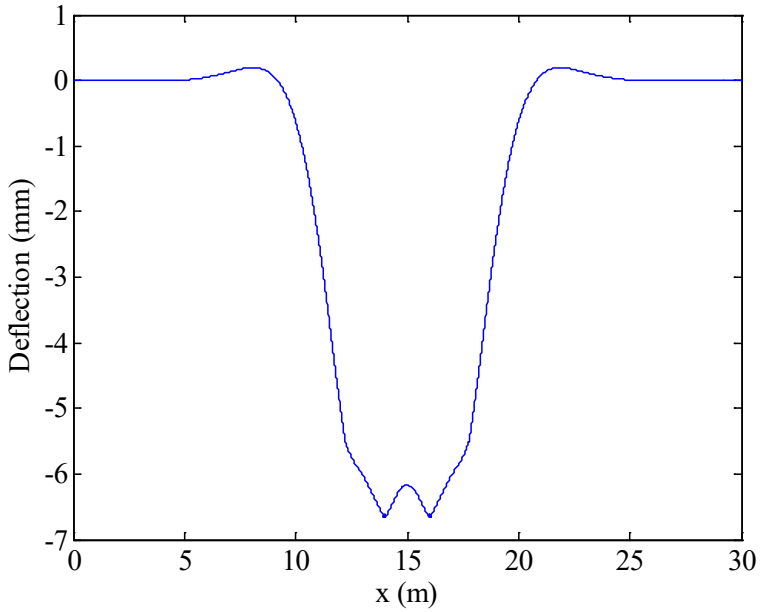

Figure 3.45. Deflection of the rail under the track modulus of 27.58 MPa at the axle spacing L1=2.0 m from the Rail on Continuous Foundation Model with wheel loads applied at the rail gauge corner

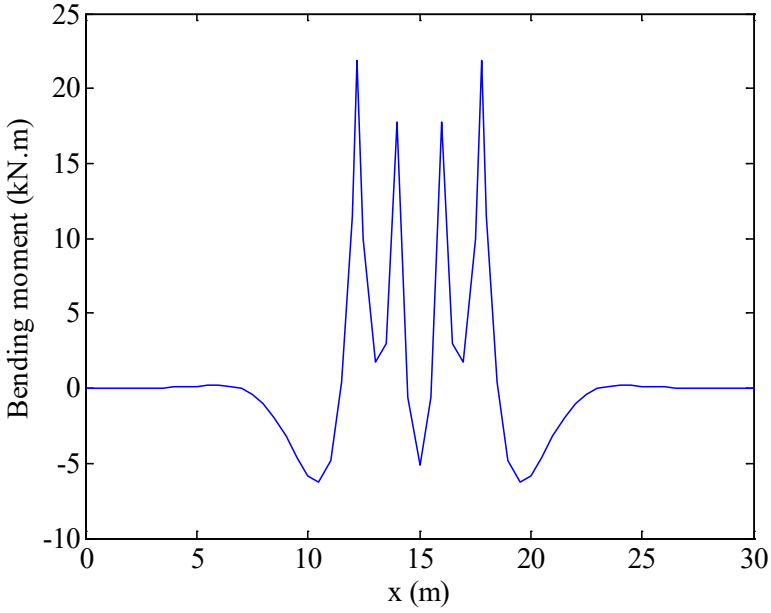

Figure 3.46. The bending moment response along the rail under the track modulus of 27.58 MPa at the axle spacing L1=2.0 m from the Rail on Continuous Foundation Model with wheel loads applied at the rail gauge corner

3.6 Summary

In this chapter, four types of finite element models of different complexities were established and described in detail: which are the Rail on Continuous Foundation Model, the Rail on One layer of Discrete Spring Supports Model, the Rail on Two layers of Discrete Spring Supports Model, and the Rail on Continuum Foundation Model. The deflection and bending moment responses of these models were given and compared together with the results from the Winkler Model for validation. Since the relative locations of wheel loads to crossties may have influence on the rail bending stress behaviour, a finite element model in which wheel loads were moved along the rail was established. In addition, since the wheel load is usually deviated from the middle point of the rail head surface due to the geometry of the wheel and the rail profiles, a finite element model in which wheel loads were applied at the rail gauge corner was established.

CHAPTER 4:PARAMETRIC STUDY OF THE RAIL BENDING STRESS BEHAVIOR WHEN THE AXLE SPACING L1 VARIES

4.1 Selection of the axle spacing L1 range for analysis

From Section 2.2.4, it has been stated that an axle spacing L1 range of 2.0-4.0 m may be suitable for our investigation since it covered the axle spacing L1 variation range of most types of railcars accounting for 66% in North America freight railways including the three dominant types of railcars which accounts for 59%. Figure 4.1 shows the maximum bending stresses at the rail head from the Rail on One layer of Discrete Spring Supports Model under the track modulus of 13.79 MPa. From Figure 4.1 (a), it can be seen that the maximum bending stress at the rail head first increases and then shows a tendency to decrease at the axle spacing L1 of 3.5 m.

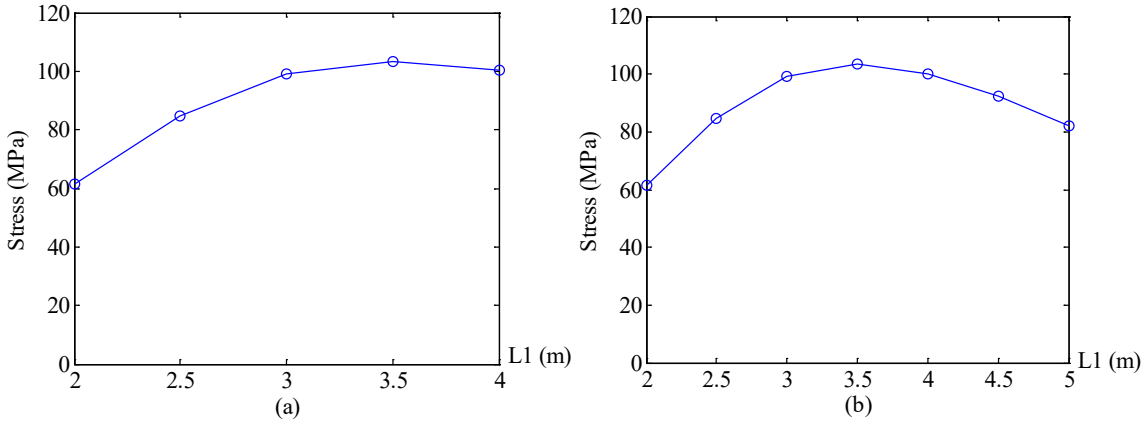

Figure 4.1. The maximum bending stress at the rail head vs. axle spacing L1 from the Rail on One layer of Discrete Spring Supports Model under the track modulus of 13.79 MPa. (a) When the axle spacing L1 range is 2.0-4.0 m; (b) When the axle spacing L1 range is 2.0-5.0 m.

However, the decreasing pattern seems to be not quite complete until the axle spacing L1 of 4.0 m. The range of the axle spacing L1 was then extended to 5.0 m for a clearer pattern and the relationship between the maximum bending stress at the rail head and the axle

spacing L1 is shown in Figure 4.1 (b). From Figure 4.1 (b), it clearly shows that the maximum bending stress at the rail head first increases and then decreases with the axle spacing L1 increases from 2.0 m to 5.0 m. The maximum bending stress at the rail head starts to decrease when the axle spacing L1 is 3.5 m. For latter data analysis, the range 2.0 m to 5.0 m will be used for the axle spacing L1 variation.

4.2 Track modulus effects

4.2.1 The maximum bending stress at the rail head

Under each track modulus, when the axle spacing L1 varies from 2.0 m to 5.0 m, the maximum bending stresses at the rail head were obtained from different types of models, i.e. the Winkler Model, the Rail on Continuous Foundation Model, the Rail on One layer of Discrete Spring Supports Model, the Rail on Two layers of Discrete Spring Supports Model and the Rail on Continuum Foundation Model. These results are shown in Figure 4.2 in which the red line with "×" markers represents the results under the track modulus of 13.79 MPa, the blue line with "○" markers represents the results under the track modulus of 27.58 MPa and the magenta line with "□" markers represents the results under the track modulus of 41.37 MPa. Figure 4.2 (a) to Figure 4.2 (e) correspond to the results from the Winker Model, the Rail on Continuous Foundation Model, the Rail on One layer of Discrete Spring Supports Model, the Rail on Two layers of Discrete Spring Supports Model and the Rail on Continuum Foundation Model respectively.

From Figure 4.2, it shows that, when the track is in the soft condition, corresponding to the track modulus U=13.79 MPa, with the axle spacing L1 increasing from 2.0 m to 5.0 m, the maximum bending stress at the rail head first increases and then starts to decrease at the axle spacing L1=3.5 m. Results from different types of models show the same pattern. When the track is in the medium and hard conditions, corresponding to the track modulus U=27.58 MPa and U=41.37 MPa, respectively, when the axle spacing L1 increases, the maximum bending stress at the rail head first increases and then starts to decrease at the axle spacing L1=3.0 m, which is earlier than that in the soft track condition. The results from different types of models also demonstrate the same pattern.

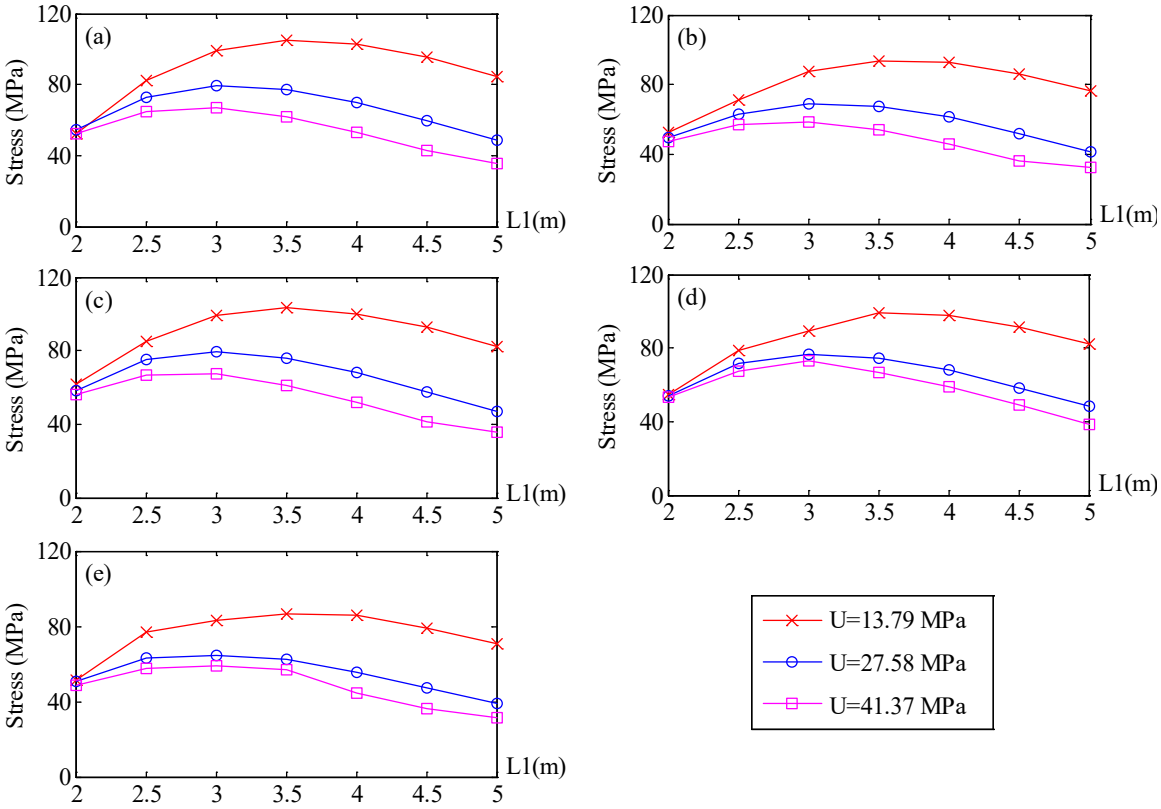

Figure 4.2. The maximum bending stress at the rail head vs. axle spacing L1 under each track modulus from the (a) Winkler Model (b) Rail on Continuous Foundation Model (c) Rail on One layer of Discrete Spring Supports Model (d) Rail on Two layers of Discrete Spring Supports Model and (e) Rail on Continuum Foundation Model

The cause of the curve pattern shown in Figure 4.2 can be explained with the Winkler model and the summation of the bending moments generated from individual wheel loads. The bending moment under a single wheel load is shown in Figure 4.3 (a), from two wheel loads in Figure 4.3 (b), and from four wheel loads in Figure 4.3 (c). From these figures, it can be seen that the peak bending moments can be decreased, after superimposition, due to the alignment of the peak maximum and minimum bending moments from adjacent wheel loads; conversely, the magnitude of these peaks increase as they are moved out of alignment.

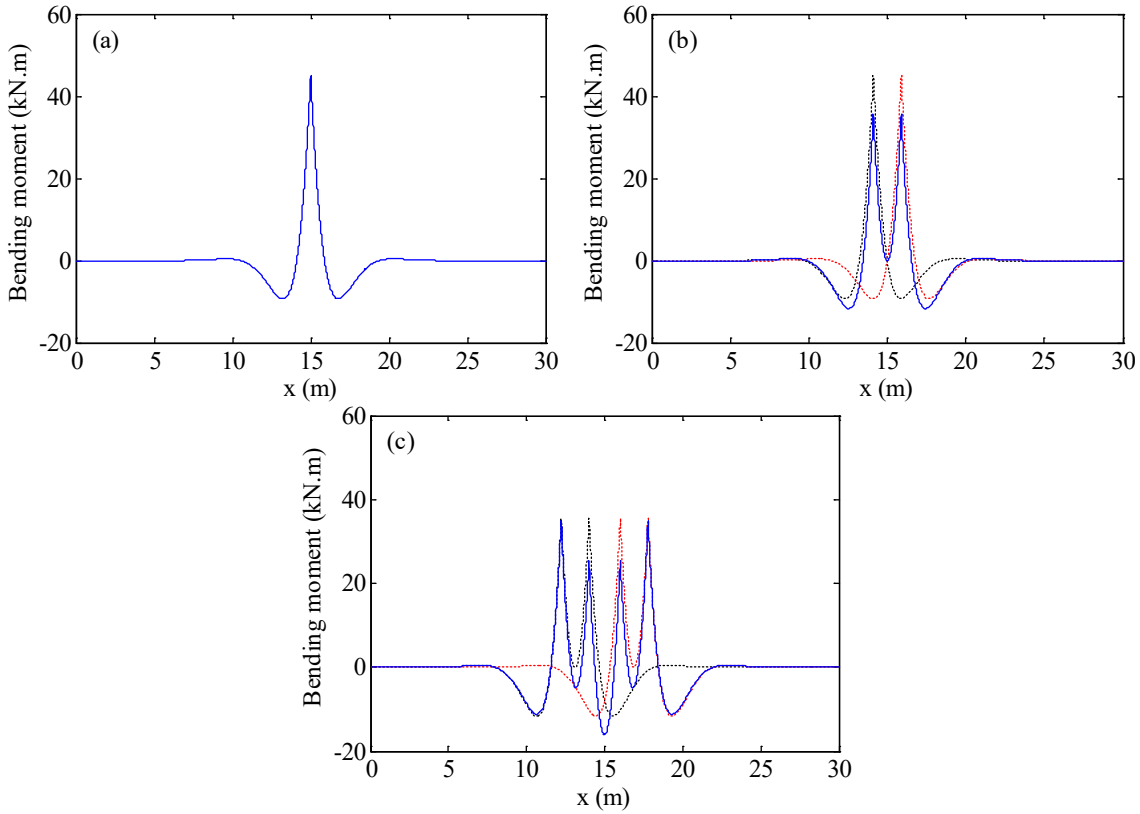

Figure 4.3. Superimposition of bending moment responses under wheel loads from the Winkler Model. (a) Single wheel load (b) Two wheel loads (c) Four wheel loads.

Figure 4.4 presents a comparison of the maximum bending stress results at the rail head from different types of models under each track modulus. Figure 4.4 (a) to Figure 4.4 (c) present the results under the track modulus of 13.79 MPa, 27.58 MPa and 41.37 MPa respectively. The red line with "◇" markers represents the results from the Winkler Model. The blue line with "◁" markers represents the results from the Rail on Continuous Foundation Model. The black line with "▷" markers represents the results from the Rail on One layer of Discrete Spring Supports Model. The green line with "△"represents the results from the Rail on Two layers of Discrete Spring Supports Model. The magenta line with "▽"represents the results from the Rail on Continuum Foundation Model.

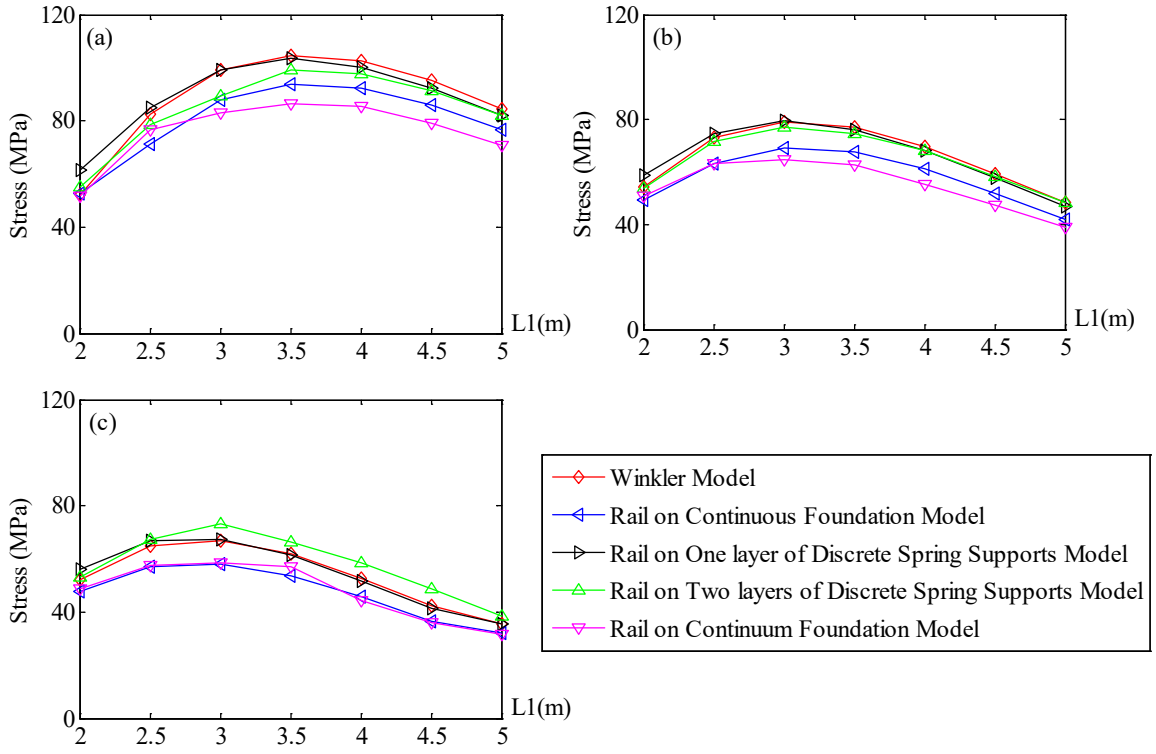

Figure 4.4. Comparison of the maximum bending stress at the rail head from different types of models under the track modulus of (a) U=13.79 MPa (b) U=27.58 MPa and (c) U=41.37 MPa

From Figure 4.4, it can be seen that, under each track modulus, the patterns of the maximum bending stress at the rail head when the axle spacing L1 varies are the same, although the bending stress values vary from model to model. Under the track modulus of 13.79 MPa and 27.58 MPa, when the axle spacing L1 varies, the Rail on Continuum Foundation Model seems to give lower maximum bending stress at the rail head than the other types of models. Under the track modulus of 41.37 MPa, the maximum bending stresses at the rail head from the Rail on Continuum Foundation Model are close to that from the Rail on Continuous Foundation Model. In addition, the maximum bending stresses at the rail head from the Rail on One layer of Discrete Spring Supports Model are quite close to that from the Winkler Model under each track modulus. When the track is in the hard condition, with the axle spacing L1 increasing, the Rail on Two layers of Discrete Spring Supports Model gives the highest maximum bending stress at the rail head than other types of models. However, for soft and medium track conditions, when the axle spacing L1 increases, the

maximum bending stresses at the rail head from the Rail on Two layers of Discrete Spring Supports Model fall in the middle of the results from other types of models.

4.2.2 The maximum bending stress at the rail base

Under each track modulus, the maximum bending stresses at the rail base from different types of models were obtained and presented in Figure 4.5.

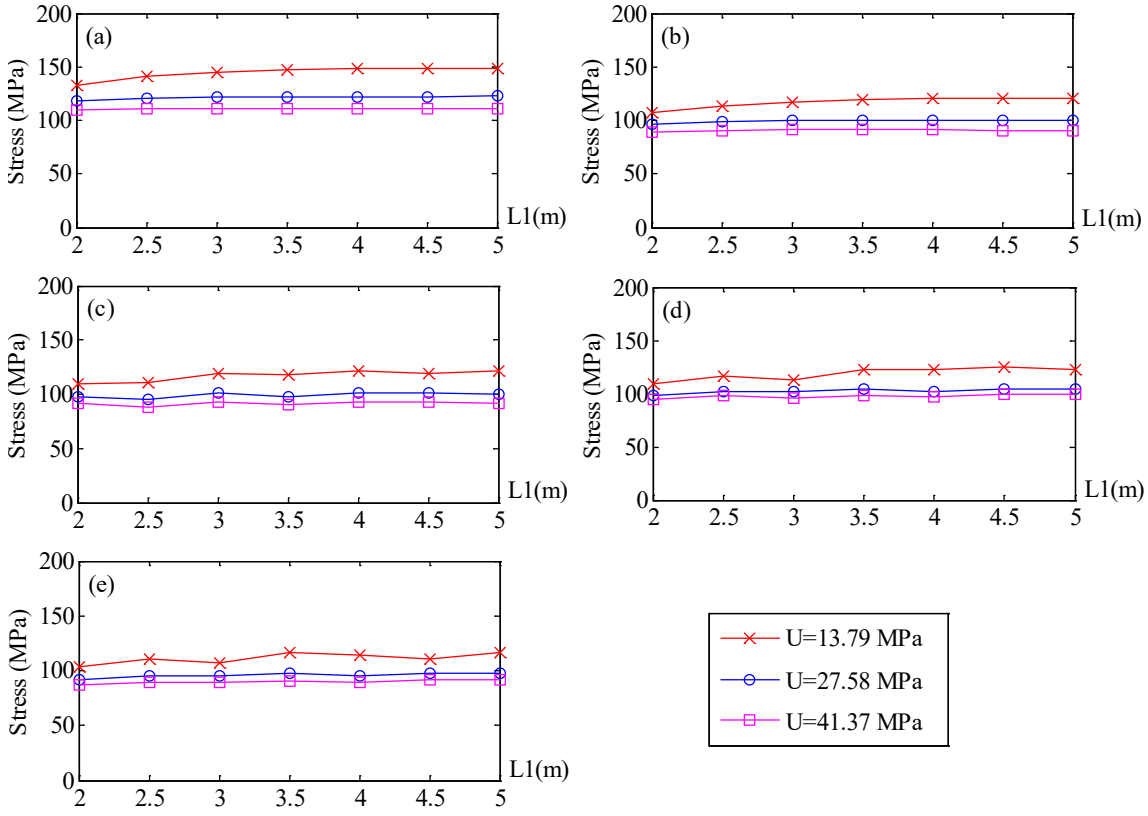

Figure 4.5. The maximum bending stress at the rail base vs. axle spacing L1 under each track modulus from the (a) Winkler Model (b) Rail on Continuous Foundation Model (c) Rail on One layer of Discrete Spring Supports Model (d) Rail on Two layers of Discrete Spring Supports Model and (e) Rail on Continuum Foundation Model

From Figure 4.5, it shows that, in general, with the axle spacing L1 increasing, the maximum bending stress at the rail base does not vary as much as that of the maximum bending stress at the rail head. From Figure 4.3 (c), it can be seen that, when the bending moment responses from two wheel loads were superimposed together, the peaks at the outer wheel locations in the final response corresponding to the maximum bending stress at the rail base were almost not affected, although the peaks at the inner wheel locations

were clearly affected. This may be the reason why the maximum bending stress at the rail base does not vary much when the axle spacing L1 varies. In addition, the bending moment at the middle of the rail, which is corresponding to the maximum bending stress at the rail head were increased obviously due to the superimposition. Thus the maximum bending stress at the rail head varies obviously when the axle spacing L1 varies. From Figure 4.5, it shows that, under each track modulus, when the axle spacing increases, the maximum bending stresses at the rail base from all types of models are nearly constant.

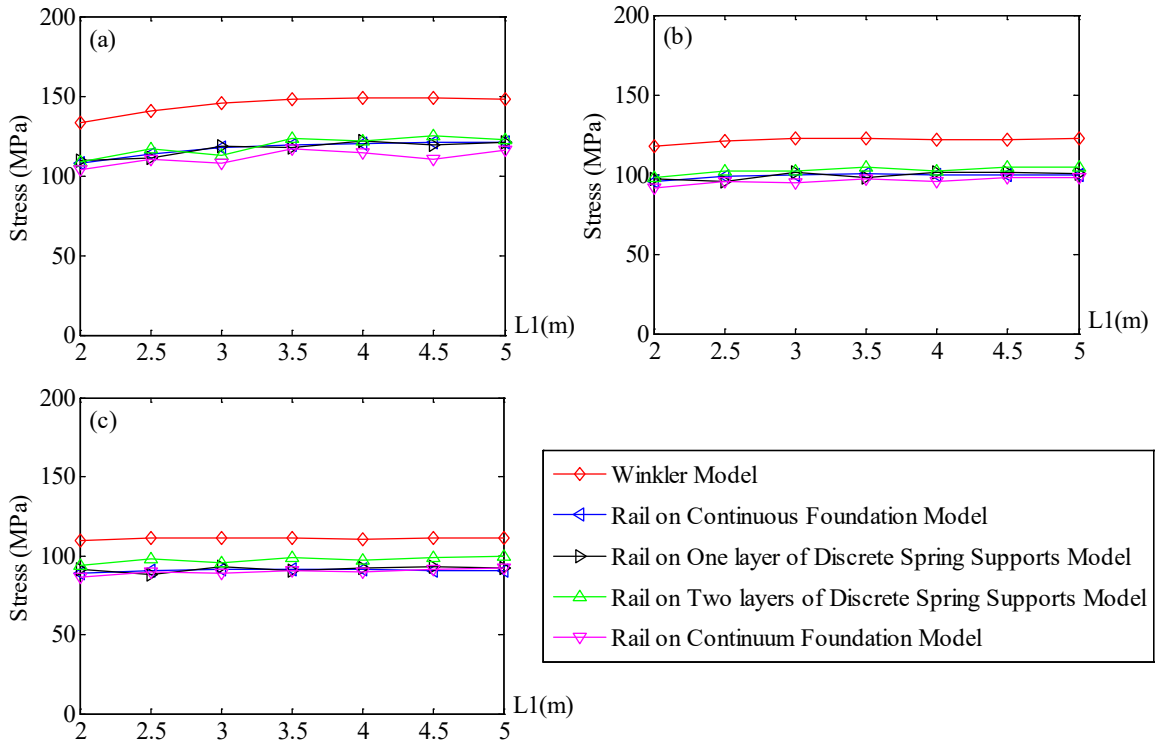

Figure 4.6. Comparison of the maximum bending stresses at the rail base from different types of models under the track modulus of (a) U=13.79 MPa (b) U=27.58 MPa and (c) U=41.37 MPa

A comparison of the results from different types of models is shown in Figure 4.6. From Figure 4.6, it can be seen that, under each track modulus, when the axle spacing L1 increases, the Winkler Model yields higher maximum bending stress at the rail base than other types of models. In addition, the Rail on Two layers of Discrete Spring Supports Model gives the second highest maximum bending stress at the rail base except for two points when the axle spacing L1=2.0 m and L1=3.0 m under the track modulus of 13.79

MPa. The Rail on Continuum Foundation still gives the lowest maximum bending stress at the rail base than other types of models when the track is in the soft and medium conditions. When the track is in the hard condition, the maximum bending stresses at the rail base from the Rail on Continuum Foundation Model are close to that from the Rail on One layer of Discrete Spring Supports Model and the Rail on Continuous Foundation Model.

4.2.3 The mean bending stress at the rail head

Under each track modulus, the mean and maximum bending stresses at the rail head at different axle spacing L1 from the Rail on Continuum Foundation Model were obtained and are shown in Figure 4.7 in which the red line with "○"markers stands for the maximum bending stress at the rail head and the blue line with "Δ" markers represents the mean bending stress at the rail head. The bending stresses at each node in the rail head area were extracted and divided by the number of nodes to get the mean bending stress at the rail head.

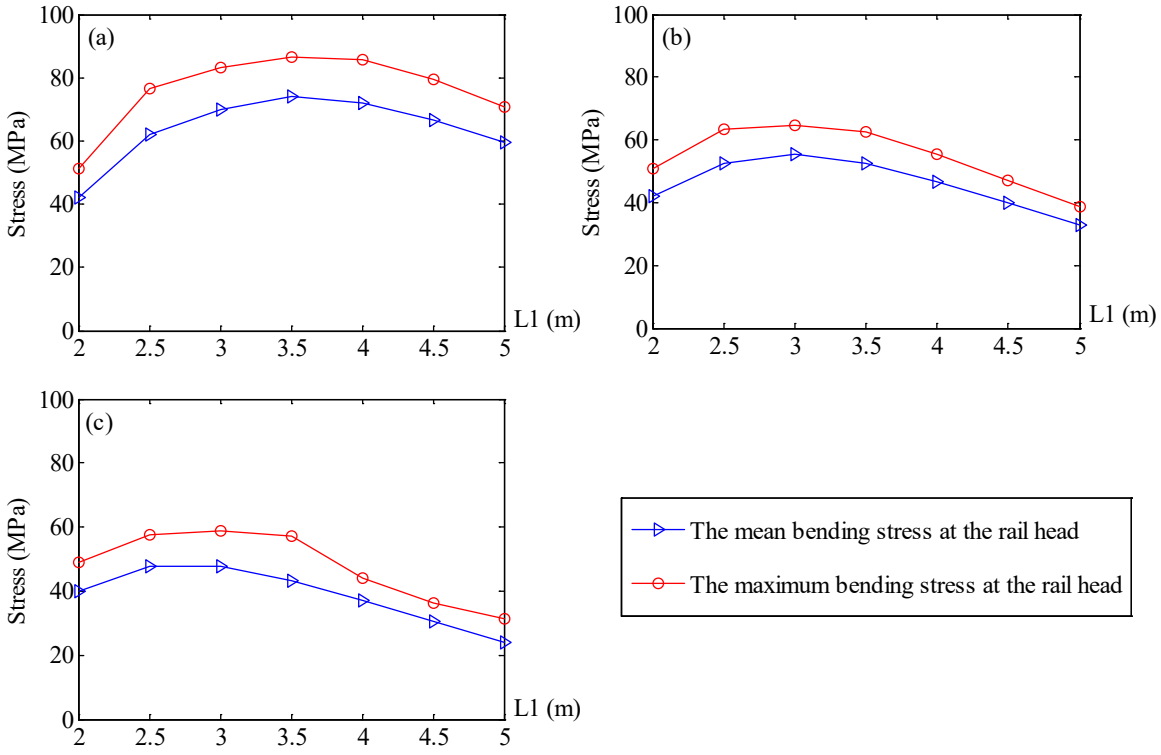

Figure 4.7. The bending stress at the rail head under the track modulus of (a) U=13.79 MPa (b) U=27.58 MPa and (c) U=41.37 MPa

Figure 4.7 (a) to Figure 4.7 (c) represents the results under the track modulus of 13.79 MPa, 27.58 MPa and 41.37 MPa respectively. It shows that, under each track modulus, the mean bending stresses at the rail head follow exactly the same pattern as that of the maximum bending stresses at the rail head when the axle spacing L1 increases from 2.0 m to 5.0 m under each track modulus.

4.3 Rail section effects

4.3.1 The maximum bending stress at the rail head

Under the track modulus of 13.79 MPa, when the axle spacing L1 varies, the maximum bending stresses at the rail head of the 115 RE rail and the 136 RE rail from each type of model can be obtained and are shown in Figure 4.8.

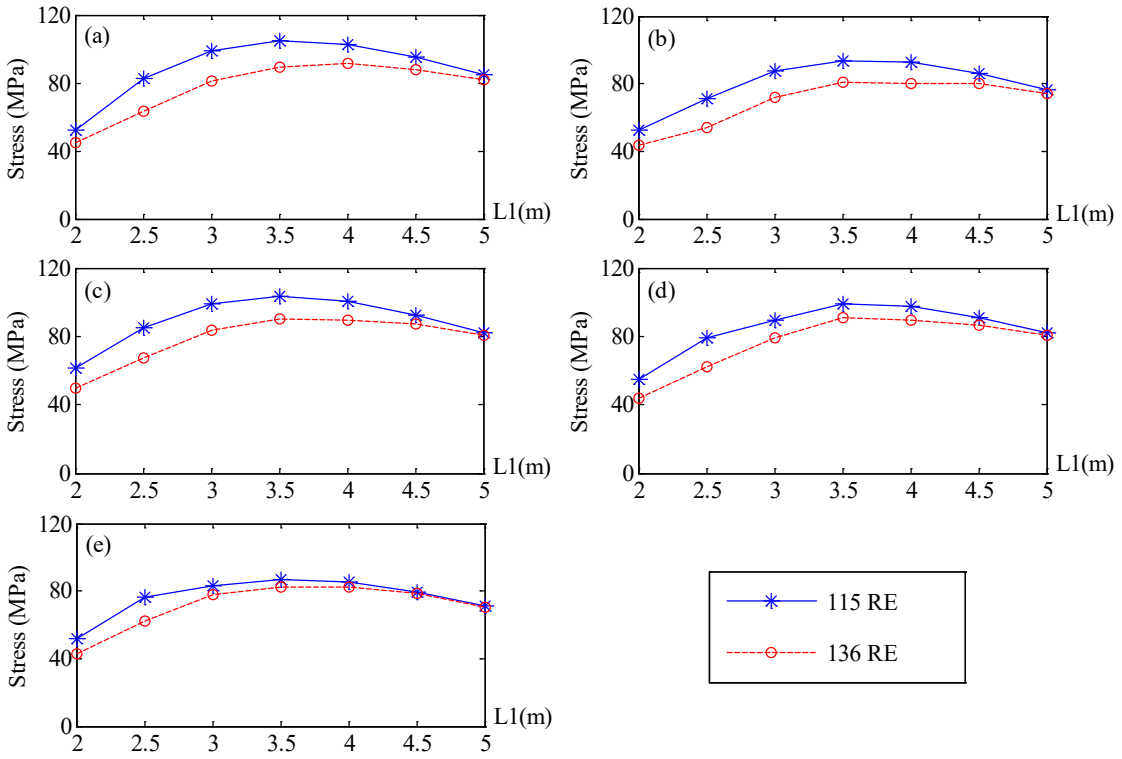

Figure 4.8. The maximum bending stresses at the rail head of the 115 RE rail and the 136 RE rail under the track modulus of 13.79 MPa from the (a) Winkler Model (b) Rail on Continuous Foundation Model (c) Rail on One layer of Discrete Spring Supports Model (d) Rail on Two layers of Discrete Spring Supports Model and (e) Rail on Continuum Foundation Model

In Figure 4.8, the blue line with "*" markers represents the maximum bending stress at the rail head of the 115 RE rail and the red dash line with "○" markers represents the maximum bending stress at the rail head of the 136 RE rail. Figure 4.8 (a) to Figure 4.8 (e) present the results from the Winker Model, the Rail on Continuous Foundation Model, the Rail on One layer of Discrete Spring Supports Model, the Rail on Two layers of Discrete Spring Supports Model and the Rail on Continuum Foundation Model respectively. It shows that, under the track modulus of 13.79 MPa, when the axle spacing L1 varies, the maximum bending stress at the rail head of the 136 RE rail is always lower than that of the 115 RE rail, which is consistent with the fact that the bending stress is decreased due to larger section properties. When the axle spacing L1 increases, the difference between the maximum bending stresses at the rail head of the 115 RE rail and of those at the 136 RE rail decreases.

In addition, when the axle spacing L1 increases, the maximum bending stresses at the rail head of both the 115 RE rail and the 136 RE rail from different types of models show a pattern of first increasing and then decreasing. For the 115 RE rail, the maximum bending stress at the rail head starts to decrease at the point of axle spacing L1=3.5 m from all types of models. However, for the 136 RE rail, the maximum bending stress starts to decrease later at the point of axle spacing L1=4.0 m based on the results from the Winkler Model and the Rail on Continuum Foundation Model. The maximum bending stress of the 136 RE rail starts to decrease at the point of L1=3.5 m based on the results from the Rail on Two layers of Discrete Spring Supports Model. The maximum bending stress at the rail head in the axle spacing L1 range of 3.5-4.5 m seems to be constant and afterwards it decreases based on the results from the Rail on Continuous Foundation Model and the Rail on One layer of Discrete Spring Supports Model. In general, when the rail section changes from the 115 RE rail to the 136 RE rail, the maximum bending stress at the rail head has a smaller variation range when the axle spacing L1 increases from 3.5 m to 4.5 m, indicating that the maximum bending stress at the rail head become less sensitive to the variation of axle spacing L1 in this range.

Under the track modulus of 27.58 MPa, when the axle spacing L1 varies, the maximum bending stresses at the rail head from different types of models can be obtained and shown in Figure 4.9.

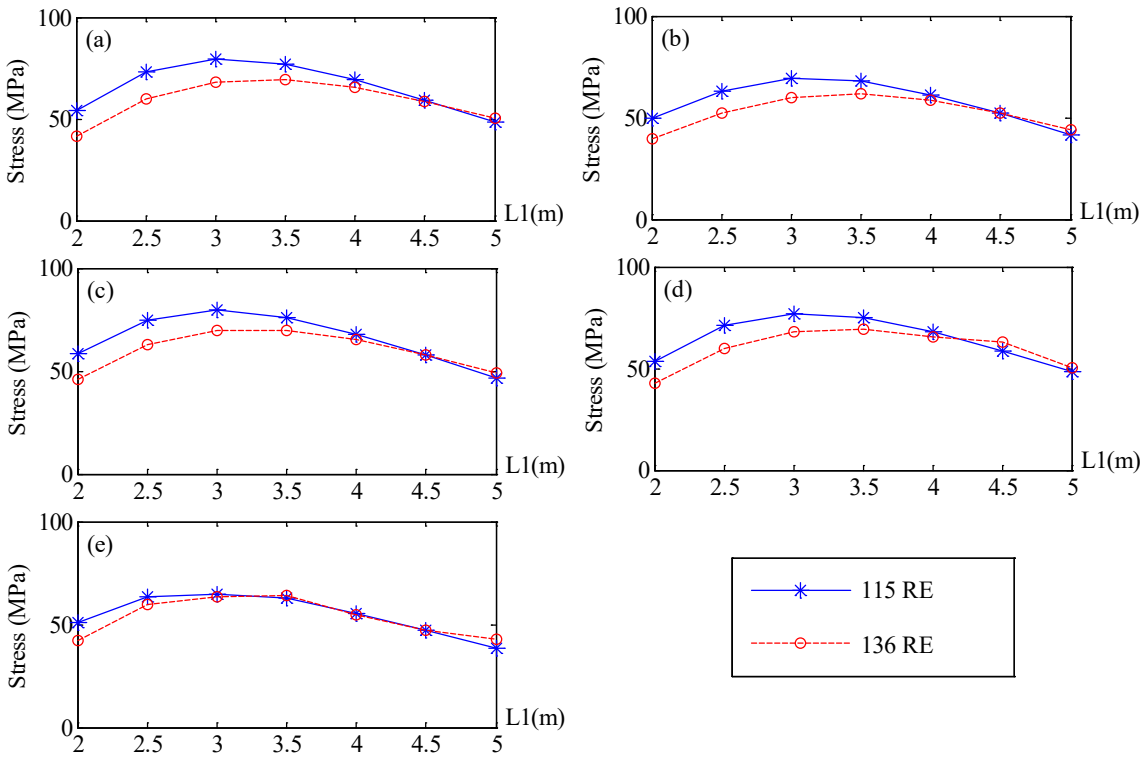

Figure 4.9. The maximum bending stresses at the rail head of the 115 RE rail and the 136 RE rail under the track modulus of 27.58 MPa from the (a) Winkler Model (b) Rail on Continuous Foundation Model (c) Rail on One layer of Discrete Spring Supports Model (d) Rail on Two layers of Discrete Spring Supports Model and (e) Rail on Continuum Foundation Model

From Figure 4.9, it shows that, the maximum bending stresses at the rail head of the 136 RE rail are lower than that of the 115 RE rail in the axle spacing L1 range of 2.0 m to 4.5 m for all types of models except at one point of the axle spacing L1=4.5 m in the Rail on Two layers of Discrete Spring Supports Model. When the axle spacing L1 increases from 4.5 m to 5.0 m, the maximum bending stresses of the 136 RE rail are higher than those from the 115 RE rail from all types of models. In addition, under the track modulus of 27.58 MPa, when the axle spacing L1 increases, the maximum bending stresses at the rail head of both the 115 RE rail and the 136 RE rail show a pattern of first increasing and then decreasing from all types of models. However, the maximum bending stress of the 115 RE rail starts to decrease at the axle spacing L1=3.0 m while that of the 136 RE rail starts to decrease later at the axle spacing L1=3.5 m.

Under the track modulus of 41.37 MPa, when the axle spacing L1 varies, the maximum bending stresses at the rail head of the 115 RE rail and the 136 RE rail from different types of models can be obtained and shown in Figure 4.10.

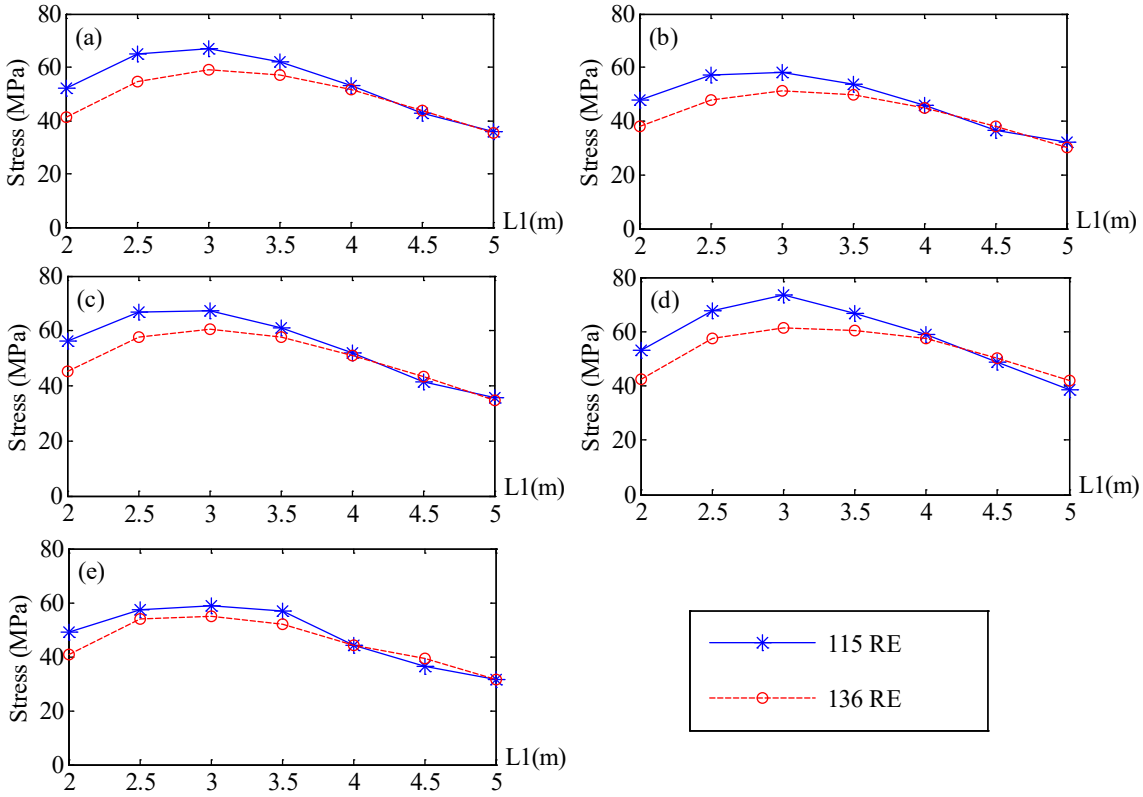

Figure 4.10. The maximum bending stresses at the rail head of the 115 RE rail and the 136 RE rail under the track modulus of 41.37 MPa from the (a) Winkler Model (b) Rail on Continuous Foundation Model (c) Rail on One layer of Discrete Spring Supports Model (d) Rail on Two layers of Discrete Spring Supports Model and (e) Rail on Continuum Foundation Model

It can be seen that, when the axle spacing L1 increases from 2.0 m to 4.0 m, the maximum bending stresses at the rail head of the 136 RE rail are lower than that of the 115 RE rail from all types of models. When the axle spacing L1 increases to 4.5 m, the maximum bending stresses at the rail head of the 136 RE rail become higher than that of the 115 RE rail. When the axle spacing L1 increases to 5.0 m, the maximum bending stresses of the 136 RE rail become lower than that of the 115 RE rail from all types of models except the Rail on Two layers of Discrete Spring Supports Model.

In addition, when the axle spacing L1 increases from 2.0 m to 5.0 m, under the track modulus of 41.37 MPa, the maximum bending stresses at the rail head of both the 115 RE rail and the 136 RE rail show a pattern of first increasing and then decreasing from all types of models. In addition, the maximum bending stresses at the rail head of both the 115 RE rail and the 136 RE rail start to decrease at the axle spacing L1=3.0 m.

4.3.2 The maximum bending stress at the rail base

Under the track modulus of 13.79 MPa, when the axle spacing L1 varies, the maximum bending stresses at the rail base of the 115 RE rail and the 136 RE rail from different types of models can be obtained and shown in Figure 4.11.

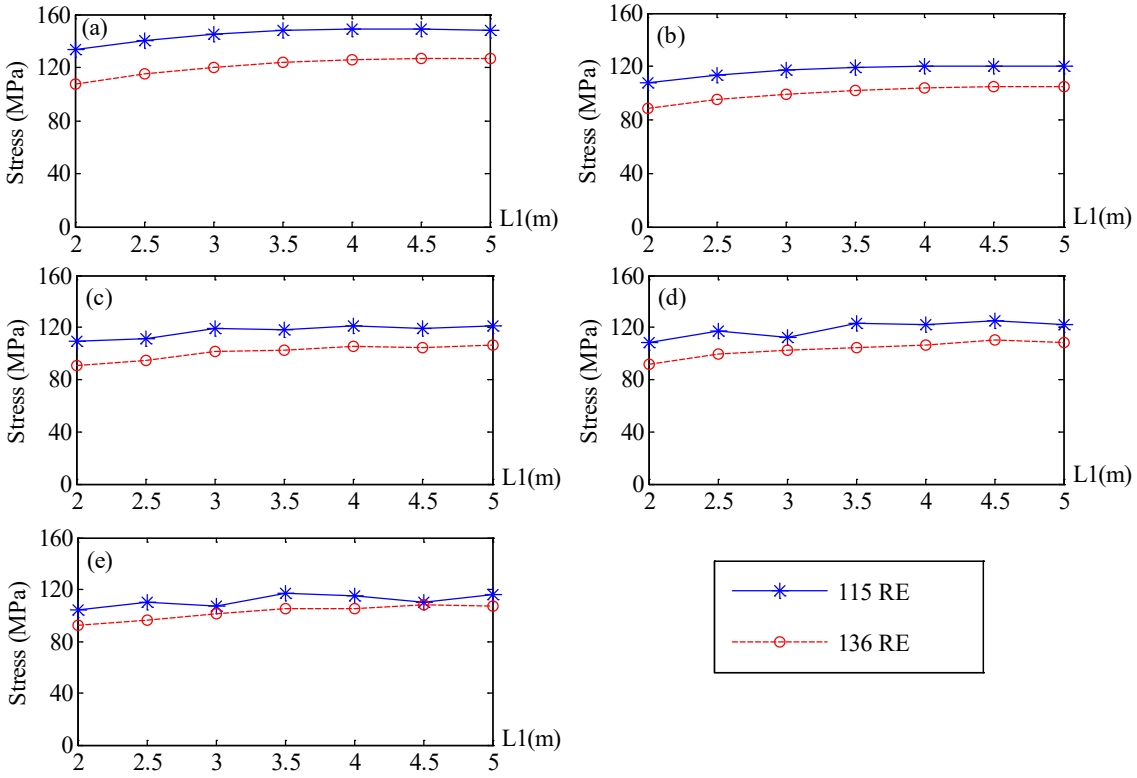

Figure 4.11. The maximum bending stresses at the rail base of the 115 RE rail and the 136 RE rail under the track modulus of 13.79 MPa from the (a) Winkler Model (b) Rail on Continuous Foundation Model (c) Rail on One layer of Discrete Spring Supports Model (d) Rail on Two layers of Discrete Spring Supports Model and (e) Rail on Continuum Foundation Model

From Figure 4.11, it shows that, under the track modulus of 13.79 MPa, when the axle spacing L1 varies, the maximum bending stresses at the rail base of the 136 RE rail are lower than that of the 115 RE rail from all types of models. The maximum bending stresses at the rail base for both the 115 RE rail and the 136 RE rail from the Winkler Model and the Rail on Continuous Foundation Model seem to be increasing when the axle spacing L1 increases from 2.0 m to 4.0 m and afterwards remain almost constant. The maximum bending stresses at the rail base from the other types of models seem to fluctuate with the axle spacing L1 increasing from 2.0 m to 5.0 m. In addition, under the track modulus of 13.79 MPa, when the axle spacing L1 varies from 2.0 m to 5.0 m, the maximum bending stress at the rail base varies less than that of the maximum bending stress at the rail head. The largest variation for the maximum bending stress at the rail base of the 115RE rail and the 136 RE rail are 16.2 MPa and 18.7 MPa, respectively, while the variation at the rail head is 52.7 MPa and 46.6 MPa, respectively.

Under the track modulus of 27.58 MPa, when the axle spacing L1 varies, the maximum bending stresses at the rail base of the 115 RE rail and the 136 RE rail from different types of models can be obtained, as shown in Figure 4.12.

From Figure 4.12, it can also be seen that, under the track modulus of 27.58 MPa, the maximum bending stresses at the rail base of the 136 RE rail are always lower than that of the 115 RE rail when the axle spacing L1 varies based on the results of all types of models. In addition, the largest variation range of the maximum bending stresses at the rail base for the 115 RE rail and the 136 RE rail is 7.2 MPa and 8.3 MPa, respectively. This variation range is less than half of that under the track modulus of 13.79 MPa, indicating that when the track modulus increases, the maximum bending stress at the rail base becomes less sensitive to the axle spacing L1 variation.

In addition, the largest variation for the maximum bending stresses at the rail head under the track modulus of 27.58 MPa for the 115 RE rail and the 136 RE rail manifests as 32.8 MPa and 28.2 MPa, respectively. This variation is more than three times that at the rail base under the same track condition, indicating that the maximum bending stress at the rail head is more sensitive to the variation of the axle spacing L1.

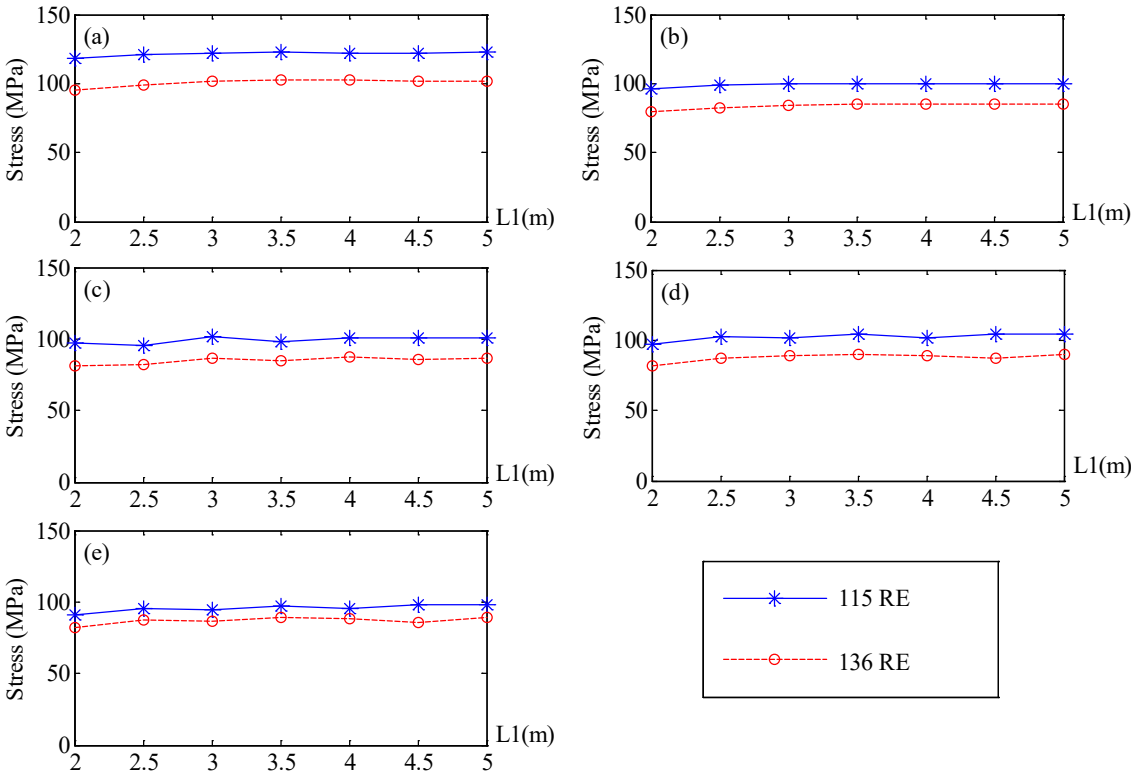

Figure 4.12. The maximum bending stress at the rail base of the 115 RE rail and 136 RE rail under the track modulus of 27.58 MPa from the (a) Winkler Model (b) Rail on Continuous Foundation Model (c) Rail on One layer of Discrete Spring Supports Model (d) Rail on Two layers of Discrete Spring Supports Model and (e) Rail on Continuum Foundation Model

Under the track modulus of 41.37 MPa, when the axle spacing L1 varies, the maximum bending stresses at the rail base of the 115 RE rail and the 136 RE rail from different types of models can be obtained, as shown in Figure 4.13.

Similarly, we can see that, under the track modulus of 41.37 MPa, when the axle spacing L1 varies, the maximum bending stresses at the rail base of the 136 RE rail are lower than those of the 115 RE rail from all types of models. When the axle spacing L1 varies, the maximum bending stresses at the rail base of both the 115 RE rail and the 136 RE rail are nearly constant, with a maximum variation range of 5.7 MPa and 6.7 MPa respectively, while that for the maximum rail bending stress at the rail head are 34.8 MPa and 26.0 MPa respectively.

In addition, the largest variation range of the maximum bending stress at the rail base for two rail sections under the track modulus of 41.37 MPa is 6.7 MPa, which is less than that under the track modulus of 13.79 MPa which is 18.7 MPa maximum and that under the track modulus of 27.58 MPa which is 8.3 MPa maximum, indicating that, with the track modulus increasing, the maximum bending stress at the rail base becomes less sensitive to the axle spacing L1 variation.

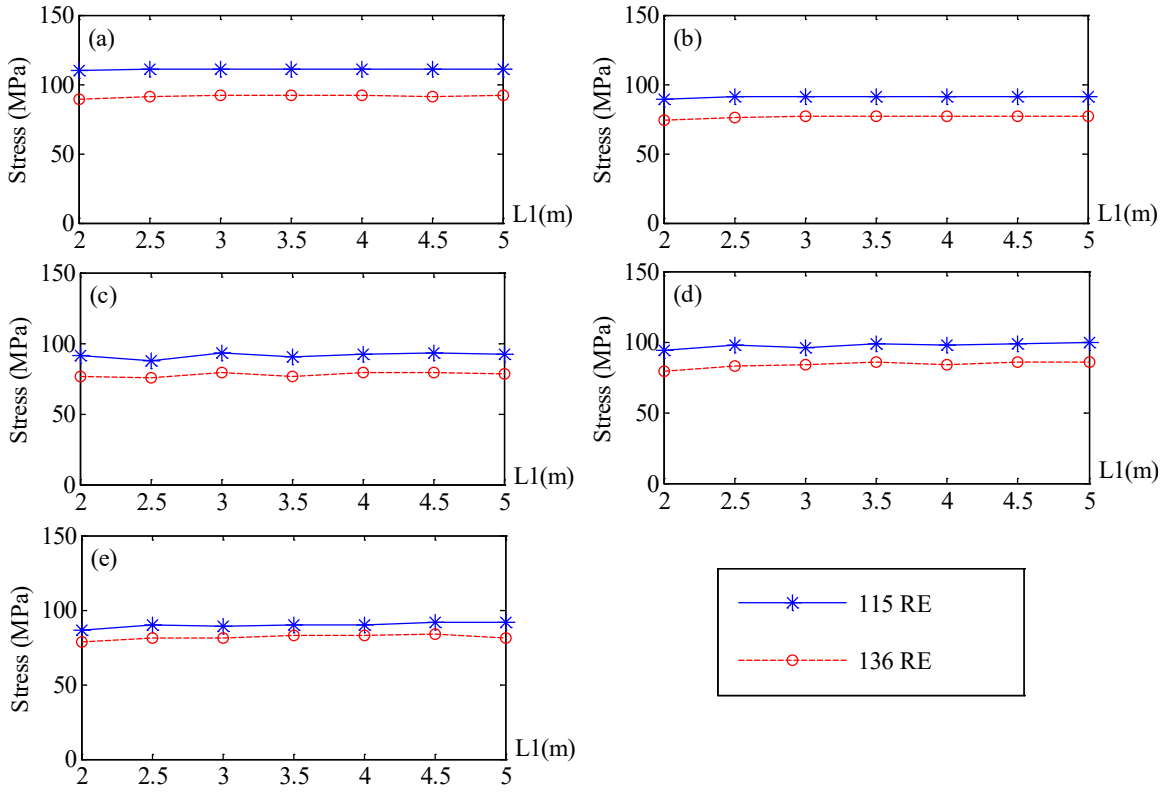

Figure 4.13. The maximum bending stress at the rail base of the 115 RE rail and 136 RE rail under the track modulus of 41.37 MPa from the (a) Winkler Model (b) Rail on Continuous Foundation Model (c) Rail on One layer of Discrete Spring Supports Model (d) Rail on Two layers of Discrete Spring Supports Model and (e) Rail on Continuum Foundation Model

4.3.3 The mean bending stress at the rail head

Under each track modulus, the mean bending stresses at the rail head of the 115 RE rail and the 136 RE rail were obtained from the Rail on Continuum Foundation Model and

shown in Figure 4.14. Figure 4.14 (a) to Figure 4.14 (c) represent the results under the track modulus of 13.79 MPa, 27.58 MPa and 41.37 MPa respectively.

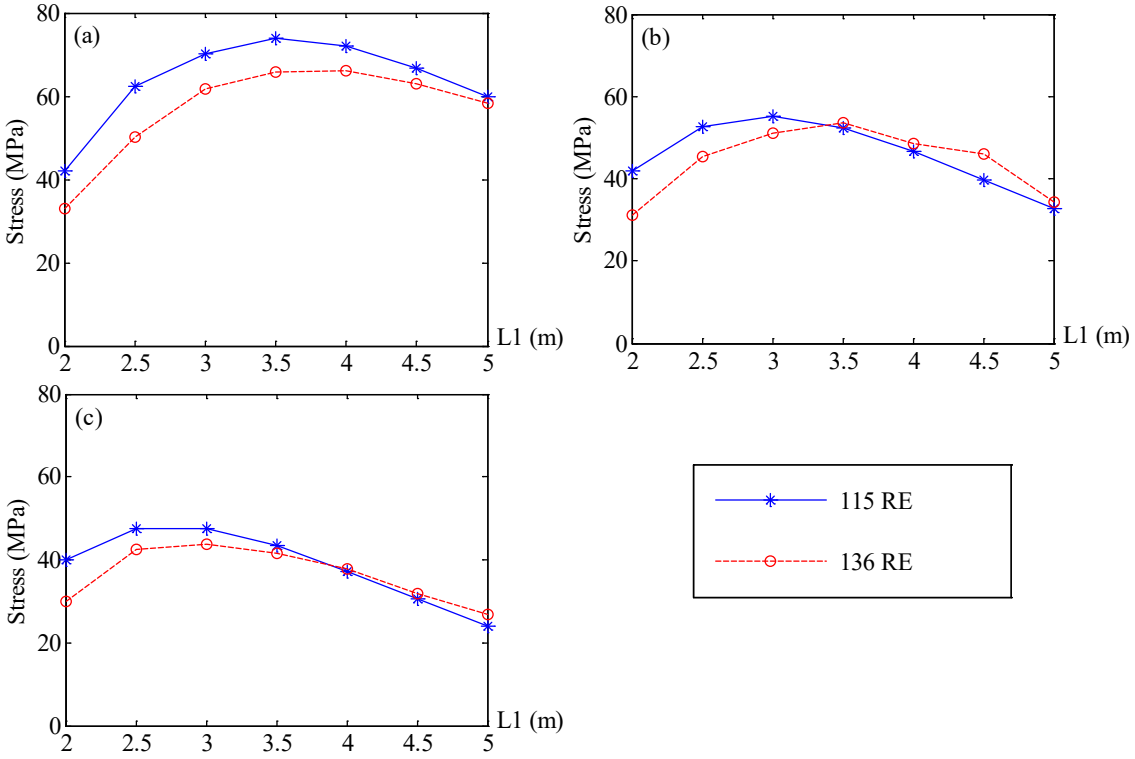

Figure 4.14. The mean bending stress at the rail head of the 115 RE rail and the 136 RE rail under the track modulus of (a) U=13.79 MPa (b) U=27.58 MPa and (c) U=41.37 MPa

It can be seen that, under each track modulus, the mean bending stresses at the rail head of both the 115 RE rail and the 136 RE rail also follow a pattern of first increasing and then decreasing with the axle spacing L1 increasing. In addition, the mean bending stress at the rail head of the 136 RE rail starts to decrease at the axle spacing L1=4.0 m under the track modulus of 13.79 MPa, later than that of the 115 RE rail which is 3.5 m.

Under the track modulus of 27.58 MPa, the mean bending stress at the rail head of the 136 RE rail starts to decrease at the axle spacing L1=3.5 m, also later than that of the 115 RE rail which is 3.0 m. Under the track modulus of 41.37 MPa, the mean bending stress at the rail head of the 136 RE rail starts to decrease at the axle spacing L1=3.0 m, which is the same as that of the 115 RE rail.

4.4 Load location effects

4.4.1 Case I—The relative locations of wheel loads to crossties vary

When the wheel loads move along the rail, the relative locations of wheel loads to crossties can vary, which may affect the rail bending stress behaviour. Under the track modulus of 13.79 MPa, when the wheel loads pass a section of 10 m of the rail, the maximum bending stresses at the rail head when wheel loads were at different locations were extracted, as the Figure 4.15 shows. The rail used in this section is the 115 RE rail.

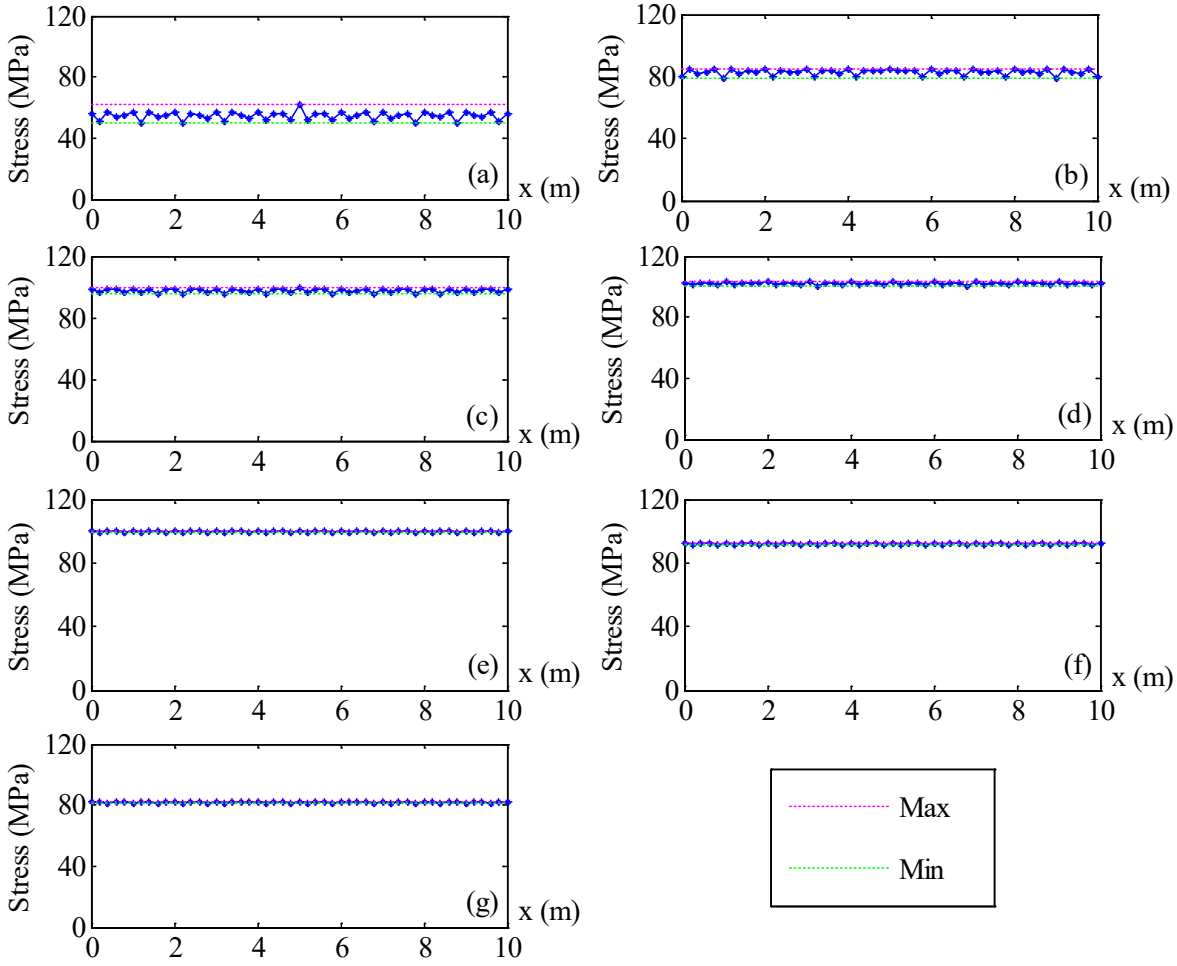

Figure 4.15. The maximum bending stress at the rail head under the track modulus of 13.79 MPa when relative locations of wheel loads to crossties vary at the axle spacing of (a) L1=2.0 m (b) L1=2.5 m (c) L1=3.0 m (d) L1=3.5 m (e) L1=4.0 m (f) L1=4.5 m and (g) L1=5.0 m

Figure 4.15 (a) to Figure 4.15 (f) represent the results under the axle spacing of 2.0 m, 2.5 m, 3.0 m, 3.5 m, 4.0 m, 4.5 m and 5.0 m respectively. In each figure, the horizontal axis denoted by "x (m)" represents the distance from the left end of the 10 m section of the rail. The magenta dot line provides an upper limit of the maximum bending stress at the rail head when wheel loads were at different locations on the rail. The green dot line provides a lower limit of the maximum bending stress at the rail head when the wheel loads were at different locations on the rail.

From Figure 4.15 (a) to Figure 4.15 (f), it can be seen that, the difference between the upper limit stress and the lower limit stress decreases when the axle spacing L1 increases, which can be seen from the narrower width between two dotted lines in each figure. In addition, the maximum bending stress at the rail head does not vary much when wheel loads move along the rail. The maximum variation occurs when the axle spacing L1=2.0 m, with a value of 11.96 MPa.

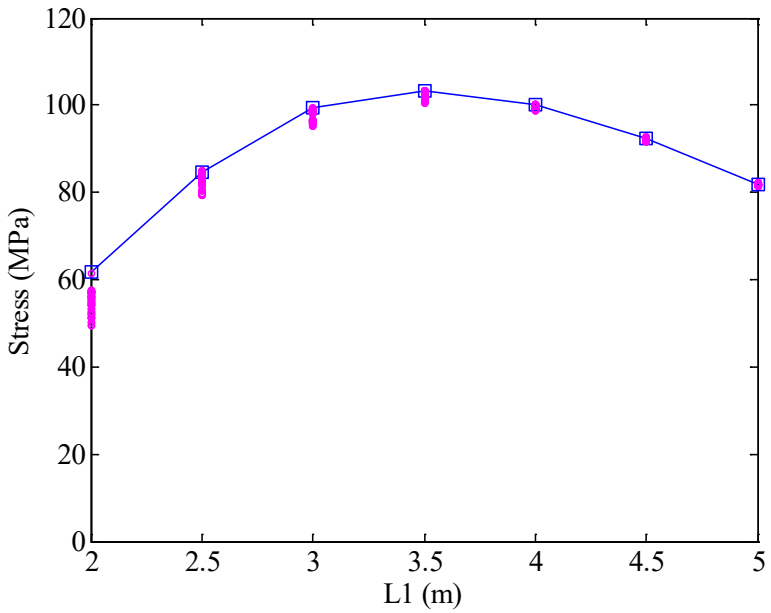

Figure 4.16. The maximum bending stress at the rail head vs. axle spacing L1 under the track modulus of 13.79 MPa

When all these stresses in Figure 4.14 are plotted together with the former maximum bending stress at the rail head vs. axle spacing L1 curve under the same track condition, Figure 4.16 can be presented. The blue line with "□" markers represents the maximum bending stress at the rail head when the locations of the wheel loads are not moved and the

magenta circles represent the points in Figure 4.15. It clearly shows that the curve pattern remains the same as that in the case of wheel loads not moved.

In general, under the track modulus of 13.79 MPa, when the relative locations of wheel loads to crossties vary, the maximum bending stress at the rail head varies, but does not have a large variation range. The maximum variation occurs at the axle spacing L1=2.0 m, and with the axle spacing L1 increasing, the variation decreases. The curve pattern representing the relationship of the maximum bending stress at the rail head vs. the axle spacing L1 under the track modulus of 13.79 MPa remains unaffected, indicating that the relative locations of wheel loads to crossties have negligible effects on it.

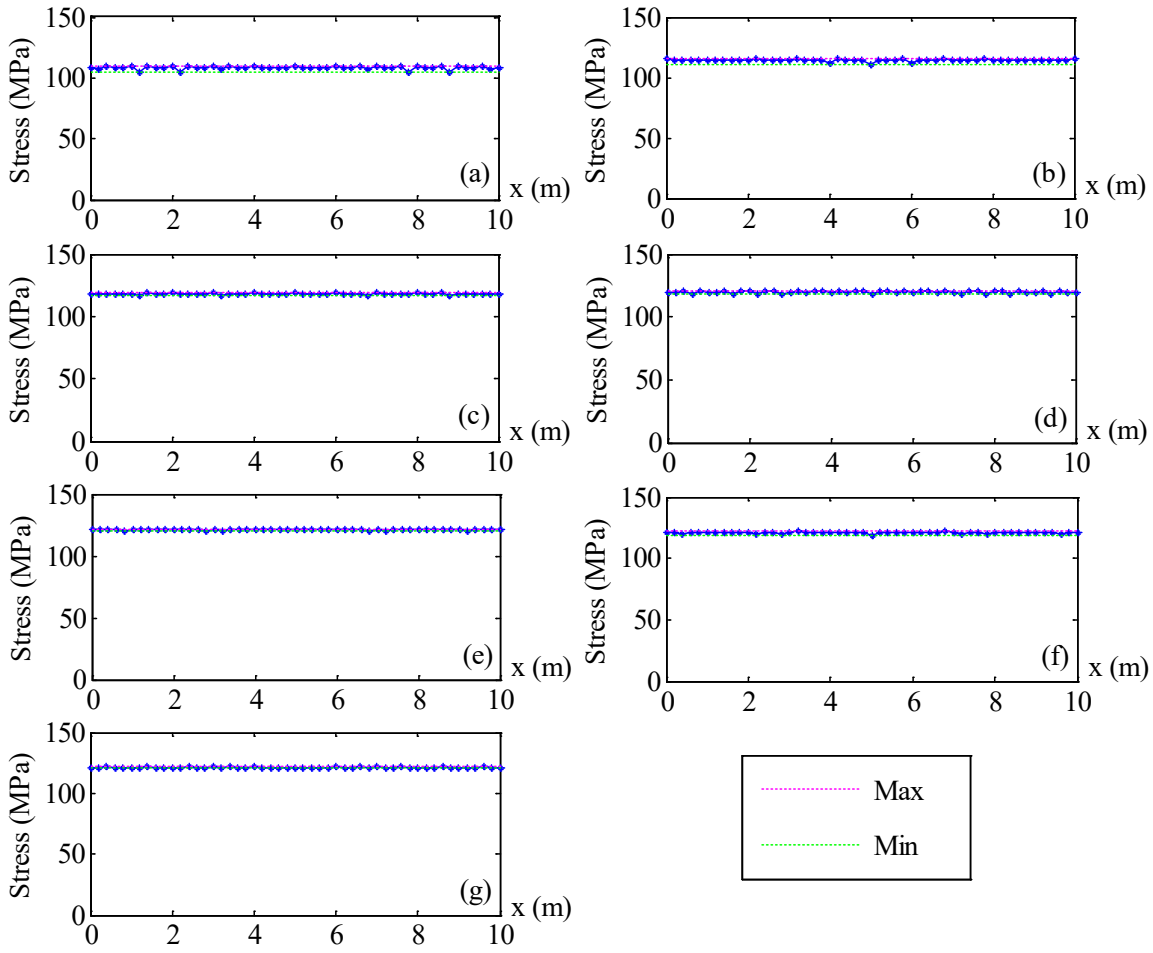

Figure 4.17. The maximum bending stress at the rail base under the track modulus of 13.79 MPa when relative locations of wheel loads to crossties vary at the axle spacing of (a) L1=2.0 m (b) L1=2.5 m (c) L1=3.0 m (d) L1=3.5 m (e) L1=4.0 m (f) L1=4.5 m and (g) L1=5.0 m

The maximum bending stresses at the rail base under the track modulus of 13.79 MPa when the relative locations of wheel loads to crossties vary were shown in Figure 4.17. Similar conclusions can be obtained from Figure 4.17 as those from Figure 4.15. The difference between the upper limit and lower limit of the maximum bending stress at the rail base decreases when the axle spacing increases, which can be seen from the narrower width between two dotted lines in each figure. In addition, the maximum bending stress at the rail base does not vary much when the wheel loads moved along the rail. The maximum variation occurs when the axle spacing L1=2.0 m, with a value of 4.20 MPa.

When all these stresses in Figure 4.17 are plotted on the maximum bending stress at the rail base vs. axle spacing L1 curve, Figure 4.18 can be obtained. It shows that, the maximum bending stresses at the rail base when axle spacing L1 increases fluctuate but still within a small range that cannot affect the curve pattern.

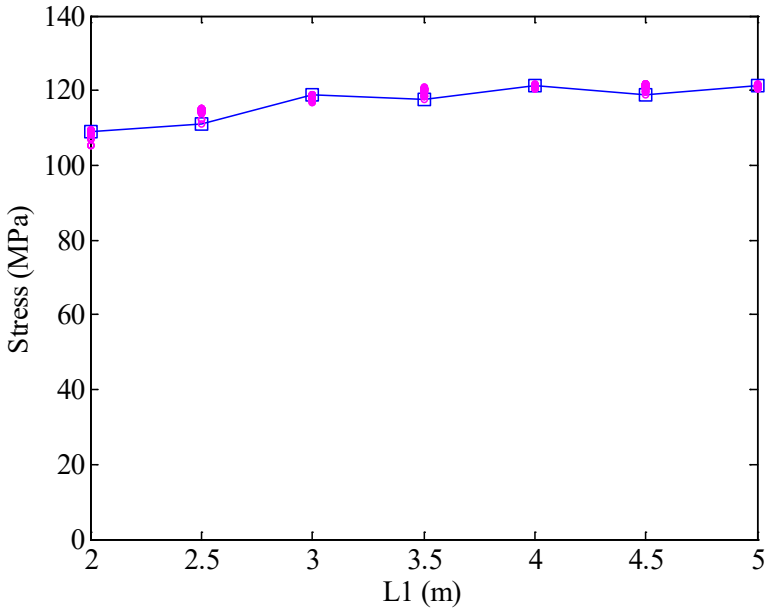

Figure 4.18. The maximum bending stress at the rail base vs. axle spacing L1 under the track modulus of 13.79 MPa

In general, under the track modulus of 13.79 MPa, when the relative locations of wheel loads to crossties vary, the maximum bending stress at the rail base varies, but does not have a large variation range. The maximum variation occurs at the axle spacing L1=2.0 m, and with the axle spacing L1 increasing, the variation decreases. The relationship of the maximum bending stress at the rail base vs. the axle spacing L1 under the track modulus

of 13.79 MPa remains unaffected, indicating that the relative locations of wheel loads to crossties have negligible effects on it.

Under the track modulus of 27.58 MPa, when the wheel loads pass a section of 10 m in the middle of the rail, the maximum bending stresses at the rail head when wheel loads were at different locations were extracted, as shown in Figure 4.19.

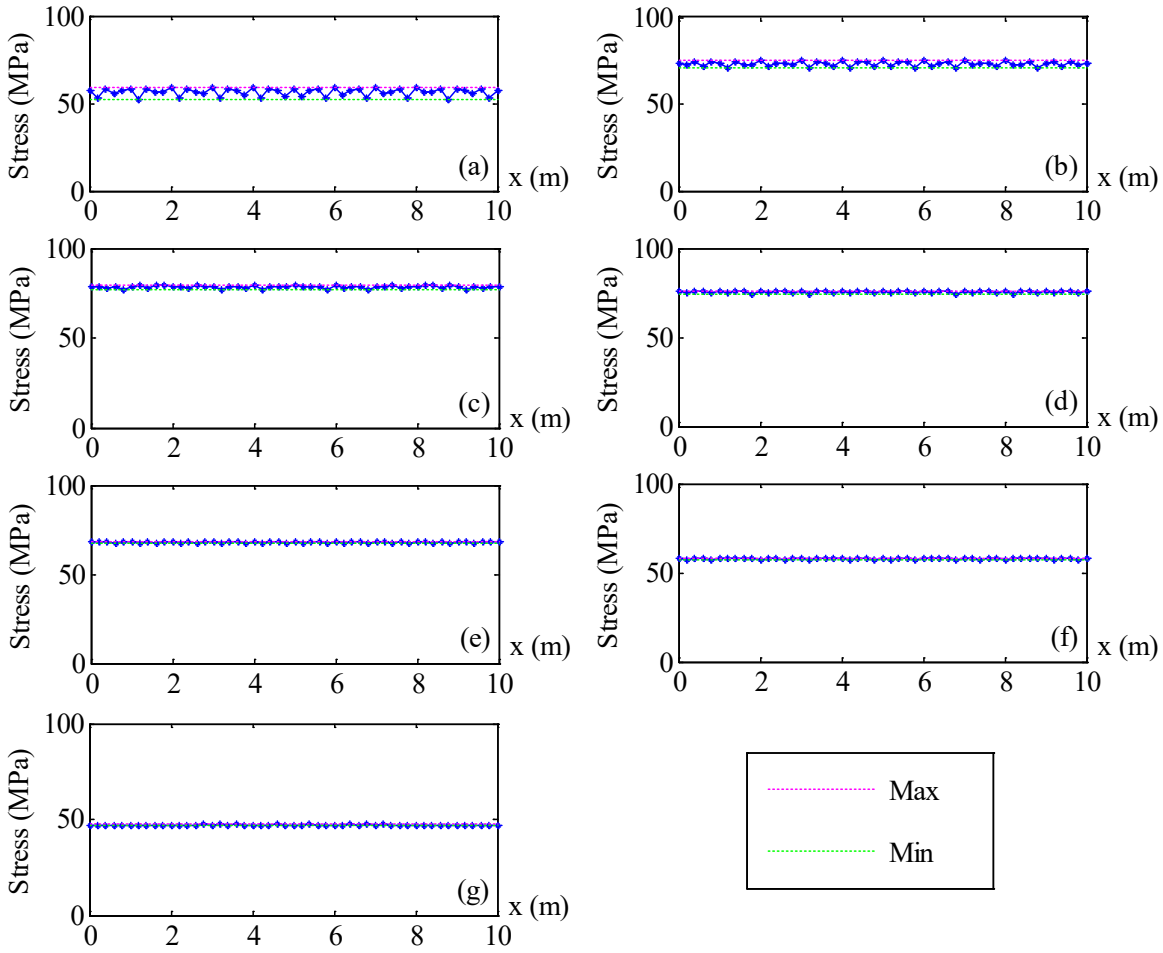

Figure 4.19. The maximum bending stress at the rail head under the track modulus of 27.58 MPa when relative locations of wheel loads to crossties vary at the axle spacing of (a) L1=2.0 m (b) L1=2.5 m (c) L1=3.0 m (d) L1=3.5 m (e) L1=4.0 m (f) L1=4.5 m and (g) L1=5.0 m

From Figure 4.19 (a) to Figure 4.19 (f), it can be seen that, the difference between the upper limit and lower limit of the maximum bending stress at the rail head decreases when the axle spacing L1 increases, which can be seen from the narrower width between two dotted lines in each figure. In addition, the maximum bending stress at the rail head does not vary

much when the wheel loads move along the rail. The maximum variation occurs when the axle spacing L1=2.0 m, with a value of 6.70 MPa.

When all these stresses in Figure 4.19 are plotted on the maximum bending stress at the rail head vs. axle spacing L1 curve, Figure 4.20 can be obtained. It shows that, the curve pattern representing the relationship of the maximum bending stress at the rail head vs. the axle spacing L1 under the track modulus of 27.58 MPa remains the same, indicating that the variation of relative locations of wheel loads to crossties has negligible effects on it.

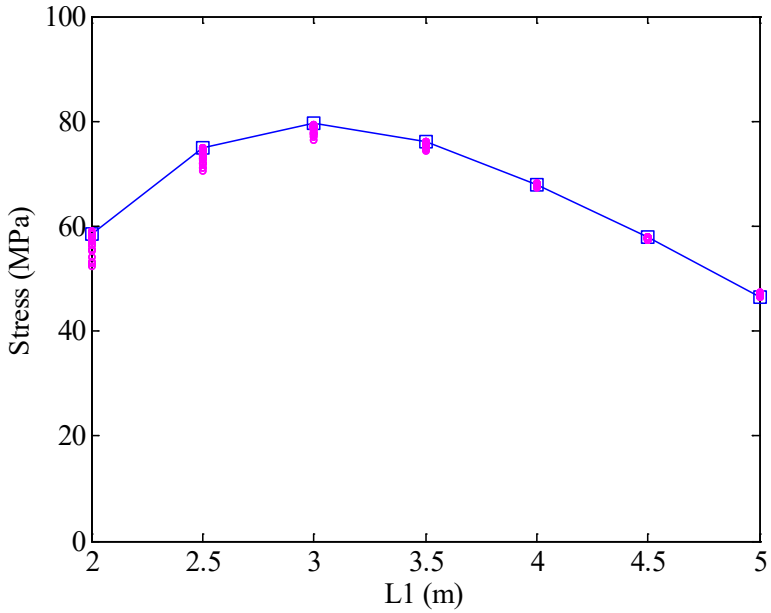

Figure 4.20. The maximum bending stress at the rail head vs. axle spacing L1 under the track modulus of 27.58 MPa

Under the track modulus of 27.58 MPa, when the wheel loads pass a section of 10 m in the middle of the rail, the maximum bending stresses at the rail base when wheel loads were at different locations were extracted, as shown in Figure 4.21.

Similar conclusions can be obtained from Figure 4.21 as that from Figure 4.19. The difference between the upper limit stress and the lower limit stress decreases when the axle spacing increases, which can be seen from the narrower width between two dotted lines in each figure. In addition, the maximum bending stress at the rail base does not vary much when the wheel loads moved along the rail. The maximum variation occurs when the axle spacing L1=2.0 m, with a value of 4.74 MPa.

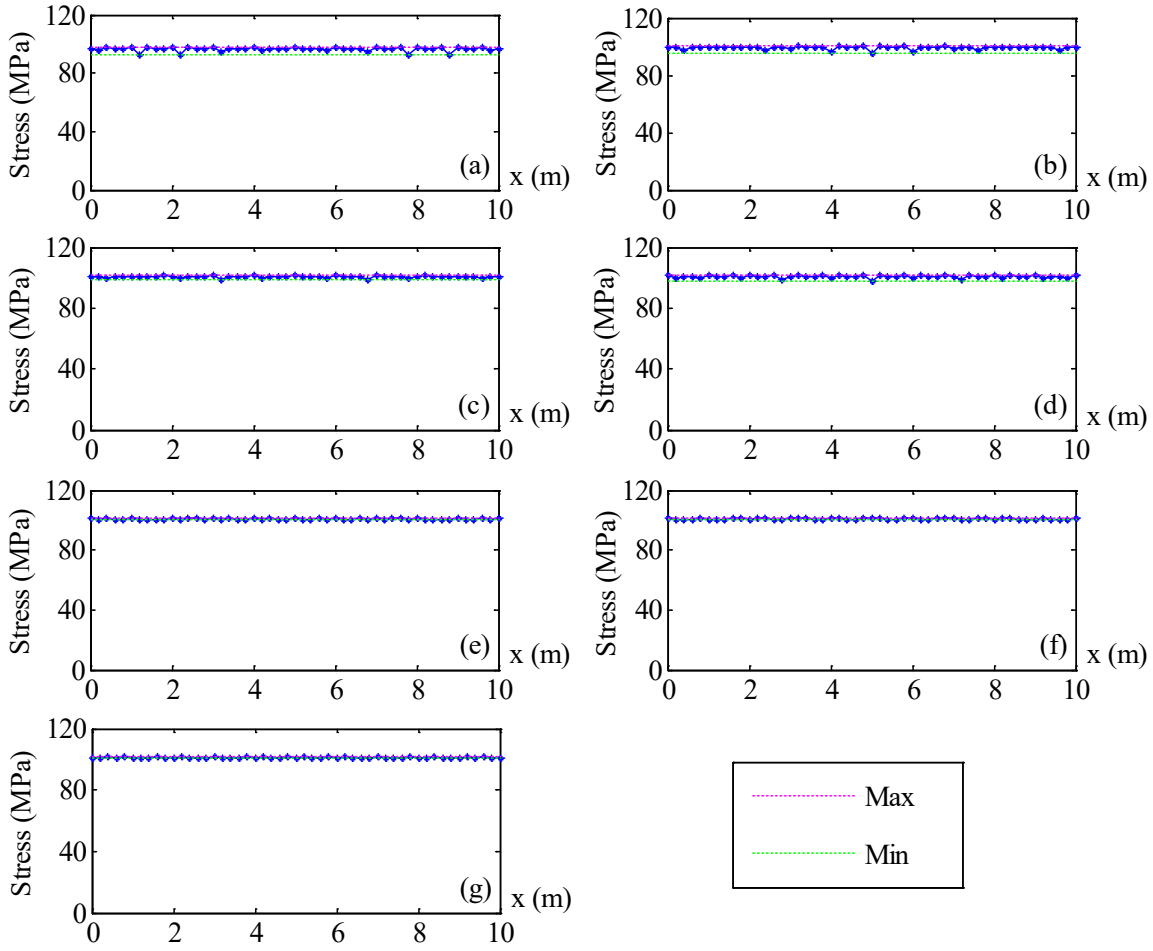

Figure 4.21. The maximum bending stress at the rail base under the track modulus of 27.58 MPa when relative locations of wheel loads to crossties vary at the axle spacing of (a) L1=2.0 m (b) L1=2.5 m (c) L1=3.0 m (d) L1=3.5 m (e) L1=4.0 m (f) L1=4.5 m and (g) L1=5.0 m

When all these stresses in Figure 4.21 are plotted on the maximum bending stress at the rail base vs. axle spacing L1 curve, Figure 4.22 can be obtained. It can be seen that, the maximum bending stress at the rail base when axle spacing increases fluctuates but within a small range. In general, under the track modulus of 27.58 MPa, when the locations of wheel loads relative to crossties vary, the maximum bending stress at the rail base varies, but does not have a large variation range. The maximum variation occurs at the axle spacing L1=2.0 m, and with the axle spacing L1 increasing, the variation decreases. The curve pattern representing the relationship of the maximum bending stress vs. axle spacing L1

under the track modulus of 27.58 MPa remains as before, indicating that the variation of relative locations of wheel loads to crossties has negligible effects on the relationship.

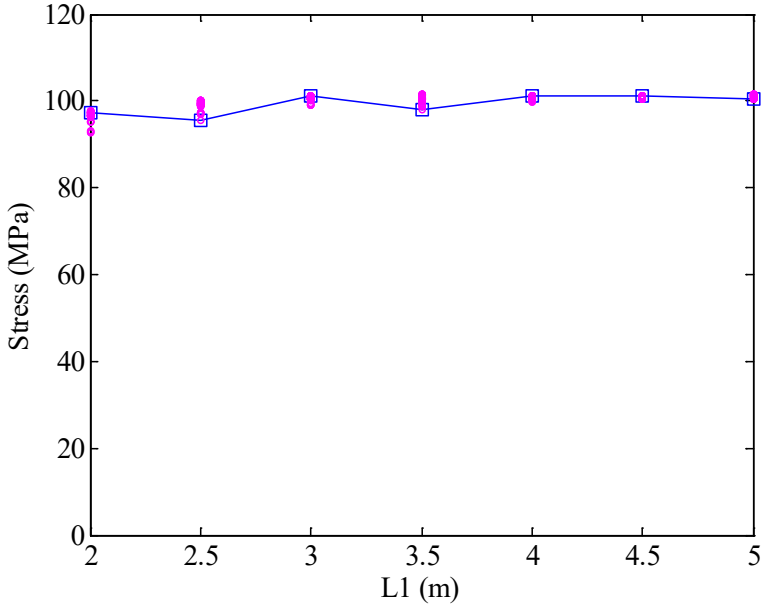

Figure 4.22. The maximum bending stress at the rail base vs. axle spacing L1 under the track modulus of 27.58 MPa

Under the track modulus of 41.37 MPa, when the wheel loads pass a section of 10 m of the rail, the maximum bending stresses at the rail head with wheel loads at different locations were extracted and appear in Figure 4.23.

From Figure 4.23 (a) to Figure 4.23 (f), it can be seen that, the difference between the upper limit stress and the lower limit stress decreases when the axle spacing increases, which can be seen from the narrower width between two dotted lines in each figure. In addition, the maximum bending stress at the rail head does not vary much when the wheel loads moved along the rail. The maximum variation occurs at the axle spacing L1=2.0 m, with a value of 6.30 MPa.

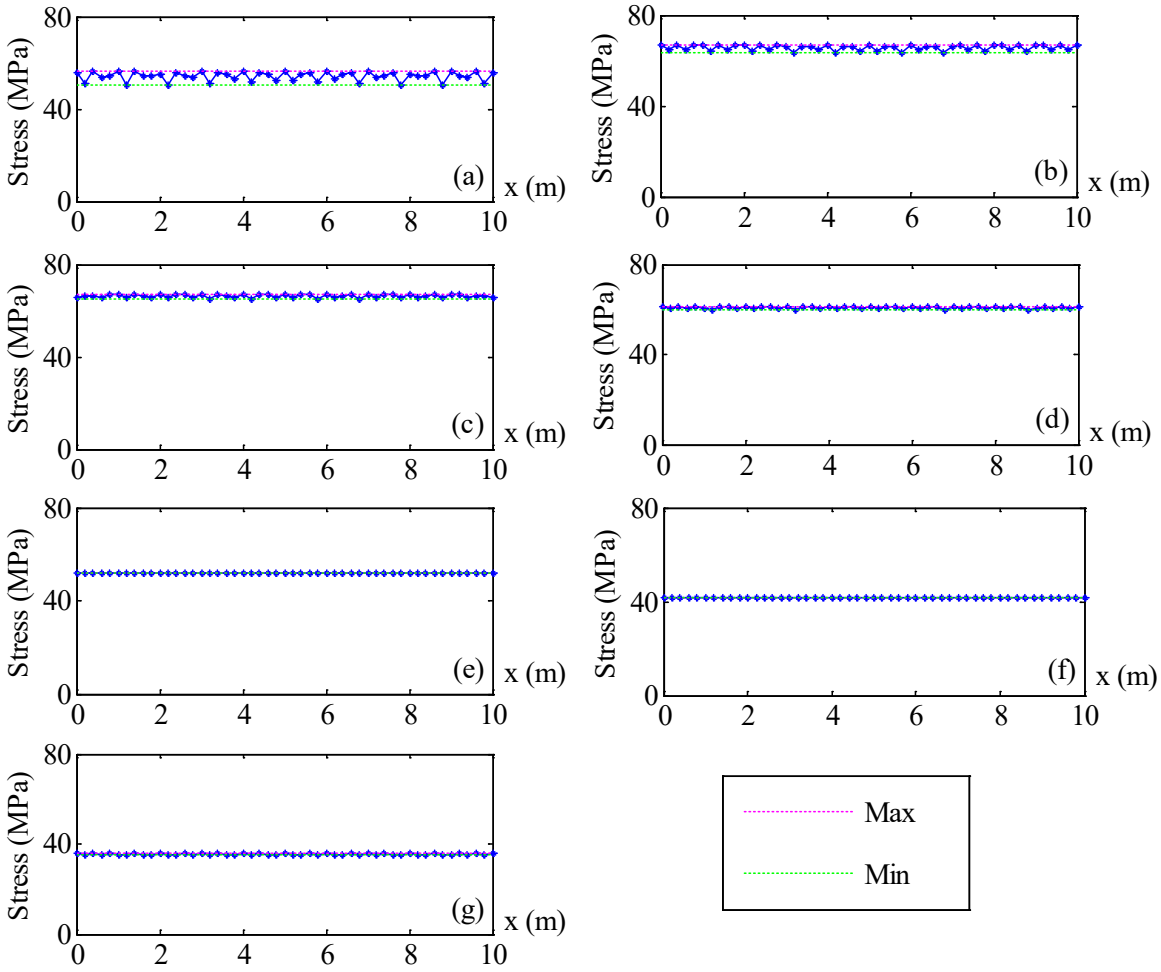

Figure 4.23. The maximum bending stress at the rail head under the track modulus of 41.37 MPa when relative locations of wheel loads to crossties vary at the axle spacing of (a) L1=2.0 m (b) L1=2.5 m (c) L1=3.0 m (d) L1=3.5 m (e) L1=4.0 m (f) L1=4.5 m and (g) L1=5.0 m

When all these points are plotted on the maximum bending stress vs. axle spacing L1 curve, as shown in Figure 4.24, it can be seen obviously that, the curve pattern remains the same.

In general, under the track modulus of 41.37 MPa, when the relative locations of wheel loads to crossties vary, the maximum bending stress at the rail base varies, but does not have a large variation range. The maximum variation occurs at the axle spacing L1=2.0 m, and with the axle spacing L1 increasing, the variation decreases. The curve pattern representing the relationship of the maximum bending stress at the rail head vs. the axle

spacing L1 under the track modulus of 41.37 MPa remains the same, indicating that the relative locations of wheel loads to crossties have negligible effects on it.

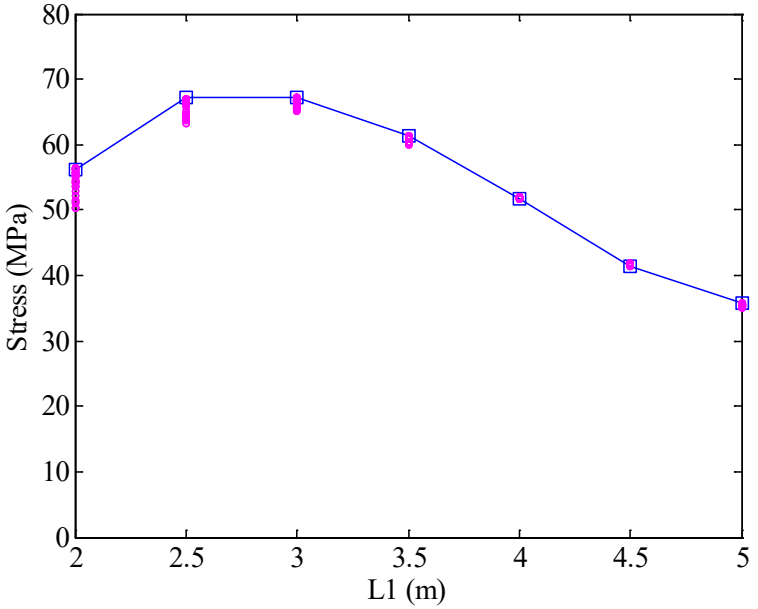

Figure 4.24. The maximum bending stress at the rail head vs. axle spacing L1 under the track modulus of 41.37 MPa

Under the track modulus of 41.37 MPa, when the wheel loads pass a section of 10 m in the middle of the rail, the maximum bending stresses at the rail base when wheel loads were at different locations on the rail were extracted and shown in Figure 4.25.

Similar conclusions can be obtained from Figure 4.25 as those from Figure 4.23. The difference between the upper limit stress and the lower limit stress decreases when the axle spacing increases, which can be seen from the narrower width between two dotted lines in each figure. In addition, the maximum bending stress at the rail base does not vary much when the wheel loads move along the rail. The maximum variation occurs when the axle spacing L1=2.0 m, with a value of 5.04 MPa.

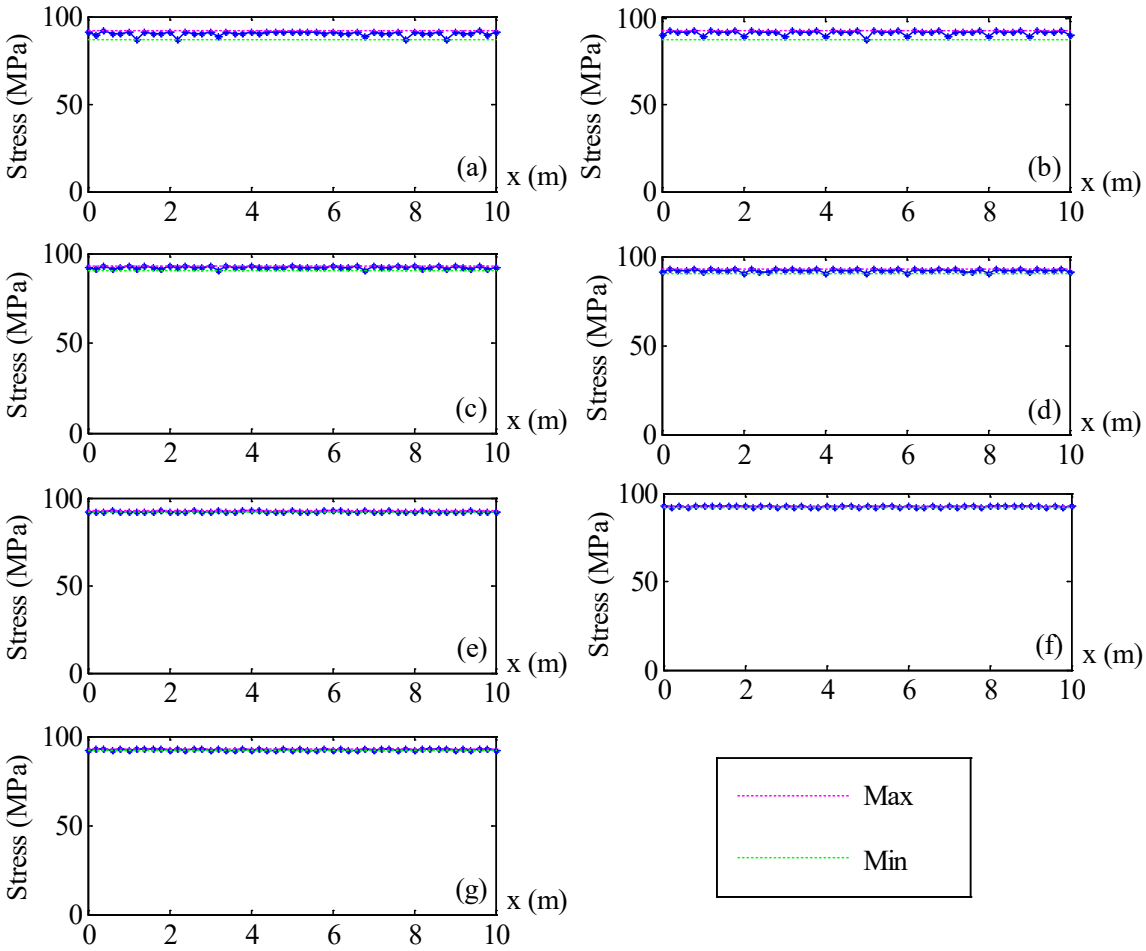

Figure 4.25. The maximum bending stress at the rail base under the track modulus of 41.37 MPa when relative locations of wheel loads to crossties vary at the axle spacing of (a) L1=2.0 m (b) L1=2.5 m (c) L1=3.0 m (d) L1=3.5 m (e) L1=4.0 m (f) L1=4.5 m and (g) L1=5.0 m

When all these stresses in Figure 4.25 are plotted on the maximum bending stress at the rail base vs. axle spacing L1 curve, Figure 4.26 can be obtained. It shows that, the maximum bending stress at the rail base when the axle spacing L1 increases fluctuates in a small range.

In general, under the track modulus of 41.37 MPa, when the relative locations of the wheel loads to crossties vary, the maximum bending stress at the rail base varies, but does not have a large variation range. The maximum variation occurs at the axle spacing L1=2.0 m, and with the axle spacing L1 increasing, the variation decreases. The curve pattern representing the relationship of the maximum bending stress vs. the axle spacing L1 under

the track modulus of 41.37 MPa remains as before, indicating that the relative locations of wheel loads to crossties have negligible effects on the relationship.

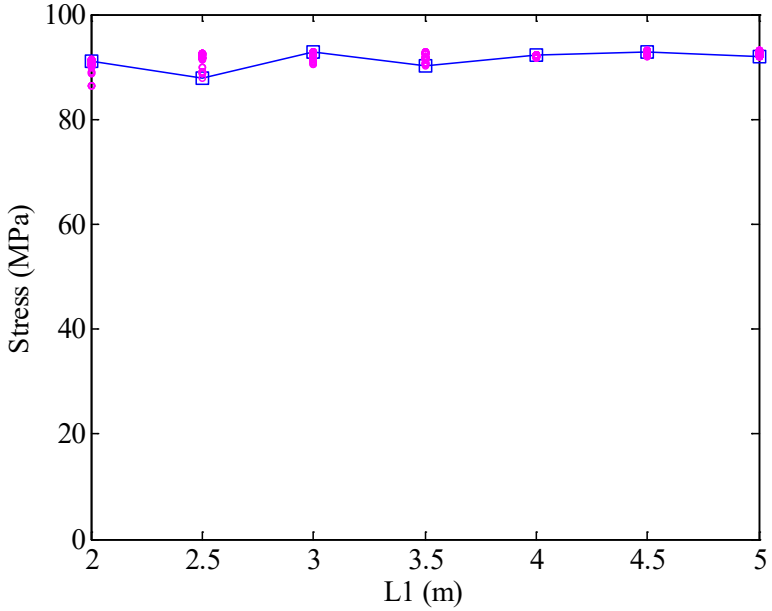

Figure 4.26. The maximum bending stress at the rail base vs. axle spacing L1 under the track modulus of 41.37 MPa

4.4.2 Case II—The wheel loads were applied at the rail gauge corner

When the wheel loads were applied at the rail gauge corner, as described in Section 3.5, under each track modulus, the maximum bending stresses at the rail head at different axle spacing L1 can be obtained and plotted in Figure 4.27 as follows. In this figure, the blue line with "*" markers represents the results from the finite element model described in the Section 3.2.1 in which wheel loads were applied at the middle of the rail head surface, denoted by "Case A". The magenta line with "○" markers represents the results from the finite element model described in the Section 3.5 in which wheel loads were applied at the rail gauge corner, denoted by "Case B".

From Figure 4.27, it shows that, under the track modulus of 13.79 MPa and 27.58 MPa, the maximum bending stress at the rail head in Case B first increases and then decreases with the axle spacing L1 increasing, the same as that in Case A. However, the points when the maximum bending stress at the rail head starts to decrease are different in two cases. In Case B, the maximum bending stress at the rail head seems to decrease later than that in

Case A. For example, under the track modulus of 13.79 MPa, the maximum bending stress at the rail head decreases from the point of axle spacing L1=4.5 m in Case B while that in Case A is at the axle spacing L1=3.5 m. Under the track modulus of 27.58 MPa, the maximum bending stress at the rail head starts to decrease at the axle spacing L1=3.5 m in Case B while that in Case A is at the axle spacing L1=3.0 m.

Under the track modulus of 41.37 MPa, the patterns of the maximum bending stress at the rail head vs. axle spacing L1 are different for two cases. In Case A, the curve pattern first increases and then decreases, while the curve pattern in Case B decreases only with the axle spacing L1 increasing.

In addition, for the medium and stiff track conditions, the maximum bending stresses at the rail head in Case B are higher than those in Case A. For the soft track condition, the maximum bending stresses at the rail head interlace for two cases.

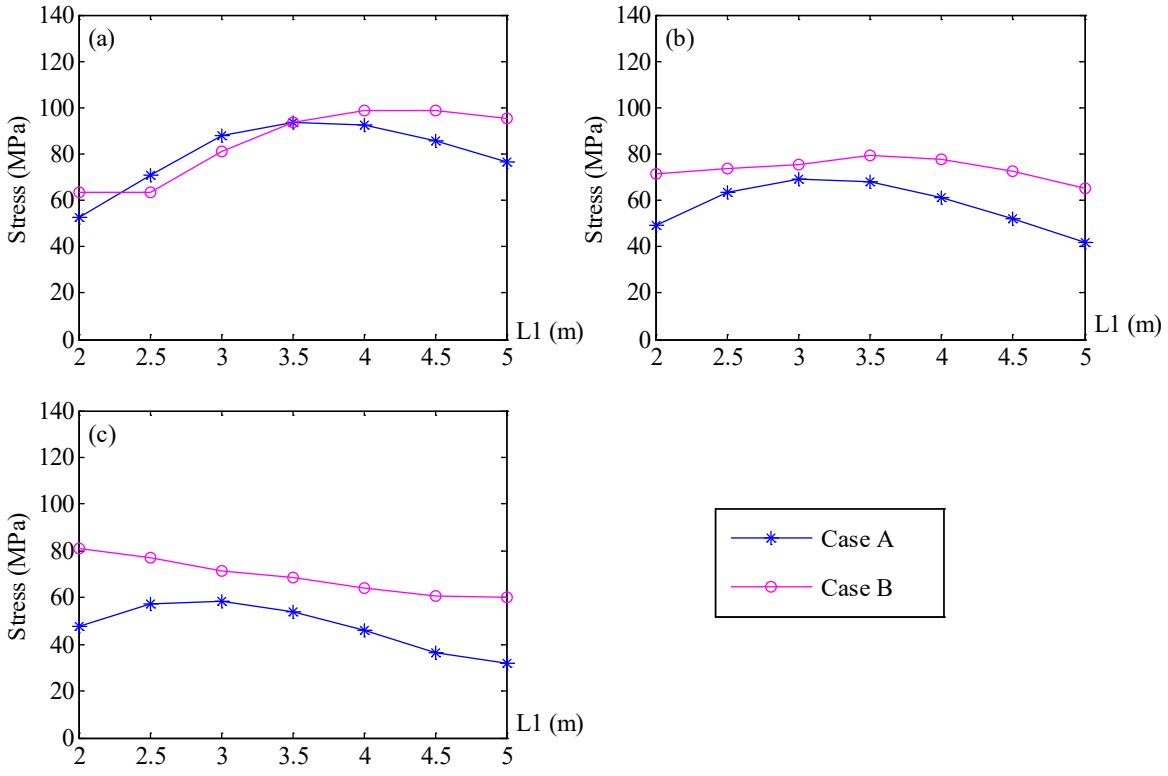

Figure 4.27. The maximum bending stress at the rail head under the track modulus of (a) U=13.79 MPa (b) U=27.58 MPa and (c) U=41.37 MPa. Case A-Wheel loads are applied at the middle of the rail head surface; Case B-Wheel loads are applied at the rail gauge corner.

In general, when wheel loads were applied at the rail gauge corner, the curve pattern of the maximum bending stress at the rail head vs. axle spacing L1 keeps first increasing and then decreasing for the soft and medium track conditions, while for the stiff track condition, the curve pattern decreases only.

Under each track modulus, the maximum bending stresses at the rail base at different axle spacing L1 were plotted in Figure 4.28 as follows.

From Figure 4.28, it shows that, the maximum bending stresses at the rail base in Case B are lower than that in Case A. In addition, the maximum bending stresses at the rail base in both two cases do not have a large variation with the axle spacing L1 increasing. In particular, the curve in Case B is nearly constant for each track modulus, with a maximum variation of 1.64 MPa.

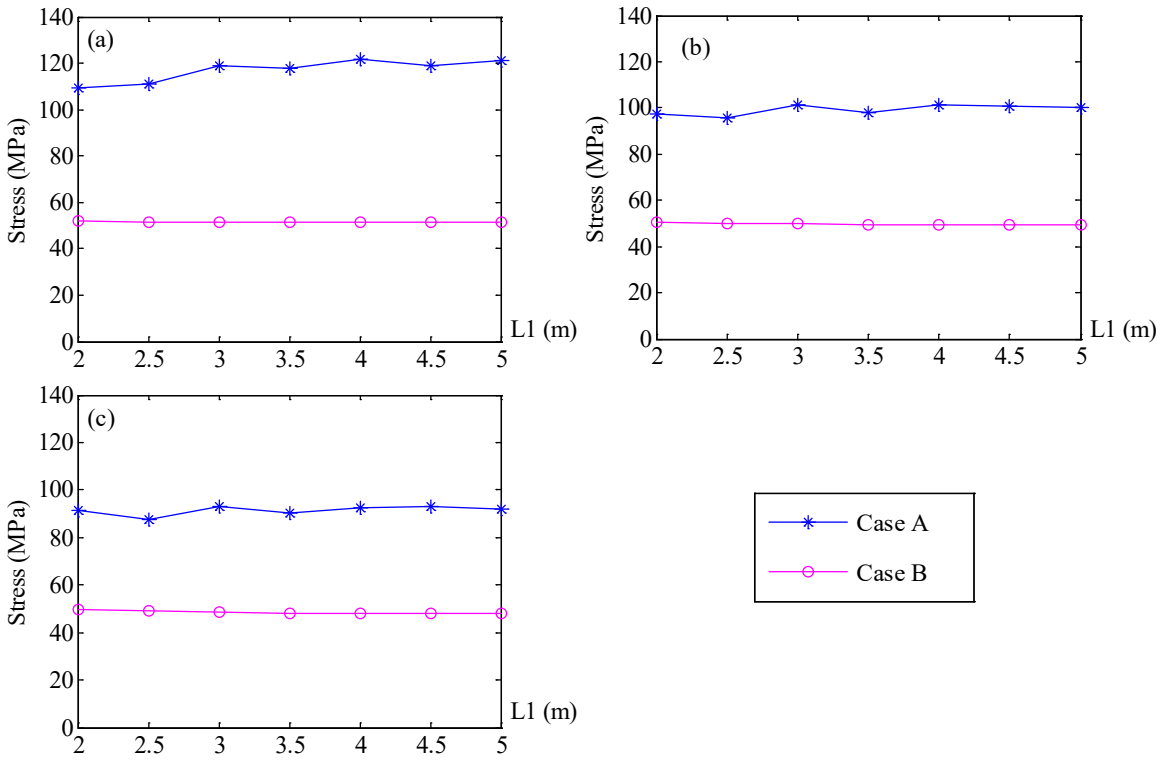

Figure 4.28. The maximum bending stress at the rail base under the track modulus of (a) U=13.79 MPa (b) U=27.58 MPa and (c) U=41.37 MPa. Case A-Wheel loads are applied at the middle of the rail head surface; Case B-Wheel loads are applied at the rail gauge corner.

4.5 Summary

In this chapter, the relationship between the maximum bending stress at the rail head and the axle spacing L1, the relationship between the maximum bending stress at the rail base and the axle spacing L1, and the relationship between the mean bending stress at the rail head and the axle spacing L1 were investigated under the soft, medium and stiff track conditions respectively. Under each track condition, the relationship was discussed and compared in detail. In general, under each track modulus, the maximum bending stress at the rail head first increases and then decreases when the axle spacing L1 increases from 2.0 m to 5.0 m.

The 115 RE rail and the 136 RE rail were investigated to see how the rail section will influence the relationship between the rail bending stresses and the axle spacing L1. In general, the maximum bending stresses at the rail head of both rail sections first increase and then decrease when the axle spacing L1 increases, but the point at which the decrease begins can be different for the two rail sections.

When the relative locations of wheel loads to crossties vary, the relationship of the maximum bending stress at the rail head vs. axle spacing L1 and the relationship of the maximum bending stress at the rail base vs. axle spacing L1 were investigated under each track modulus using the 115 RE rail. The results shows that the variation of the relative locations of wheel loads to crossties has negligible effects on the overall curve pattern representing the relationship.

When the wheel loads were moved to the rail gauge corner instead of the middle of the rail head surface, the relationship of the maximum bending stress at the rail head vs. axle spacing L1 and the relationship of the maximum bending stress at the rail base vs. axle spacing L1 were investigated under each track modulus using the 115 RE rail. Under the soft and medium track conditions, the maximum bending stress at the rail head first increases and then decreases when the axle spacing L1 increases from 2.0 m to 5.0 m. However, for the stiff track condition, the maximum bending stress at the rail head decreases only when the axle spacing L1 increases.

CHAPTER 5: SUMMARY AND CONCLUSIONS

In this thesis, finite element analysis methods combined with Winkler model analysis were used to investigate the effects of axle spacing L1 on the rail bending stress behavior. The main body of the thesis can be summarized as two parts: 1) Numerical model analysis of the railway track system; 2) Analysis of the rail bending stress behavior under different track and loading conditions, including track modulus, rail section and load locations.

In the first part, four types of finite element models of different complexities, which are the Rail on Continuous Foundation Model, the Rail on One layer of Discrete Spring Supports Model, the Rail on Two layers of Discrete Spring Supports Model and the Rail on Continuum Foundation Model, were established and described in detail. The results from these models were compared together with those from the Winker Model analysis for validation. In order to consider the effects of relative locations of wheel loads to crossties on the rail bending stress behavior, a finite element model in which wheel loads were moved to different locations along the rail was established. Since the wheel loads are usually deviated from the middle of the rail head surface, another finite element model in which wheel loads were applied at the rail gauge corner was established.

In the second part, the range of the axle spacing L1 was determined based on the rail bending stress results from numerical models in the first part combining with the data of railcars from CN, TTX, BNSF, etc. To make the relationship between the rail bending stresses and the axle spacing L1 clear and complete, a range of 2.0 m to 5.0 m was selected as the axle spacing L1 range for later analysis.

Three levels of track modulus, 13.79 MPa, 27.58 MPa and 41.37 MPa were used in the thesis to represent soft, medium and stiff track conditions, respectively. Under each track modulus, the relationship between the maximum bending stress at the rail head and the axle spacing L1, the relationship between the maximum bending stress at the rail base and the axle spacing L1, and the relationship between the mean bending stress at the rail head and the axle spacing L1 were analyzed. In addition, the patterns obtained from different types of models were compared.

Two rail sections, which are the 115 RE rail and the 136 RE rail were investigated in the thesis. Under each track modulus, the relationship between the maximum bending stress at the rail head and the axle spacing L1, the relationship between the maximum bending stress at the rail base and the axle spacing L1, and the relationship between the mean bending stress at the rail head and the axle spacing L1 from the 115 RE rail and the 136 RE rail were compared respectively to see how the rail section can affect these patterns.

When relative locations of wheel loads to crossties vary, under each track modulus, the maximum bending stresses at the rail head were obtained and these stresses were plotted on the former maximum bending stress at the rail head vs. axle spacing L1 curves to see how the curve patterns would be affected. The same procedure was conducted on the maximum bending stress at the rail base data.

When wheel loads were moved to the rail gauge corner, the maximum bending stress at the rail head and at the rail base were obtained and compared with that when wheel loads were applied at the middle of the rail head surface.

The work in this thesis provides some preliminary conclusions on the effects of axle spacing L1 on the rail bending stress behavior, which are meaningful for future study in this field and also helpful for railway operation and maintenance:

1. Under each track modulus, the maximum bending stress at the rail head first increases and then decreases when the axle spacing L1 increases from 2.0 m to 5.0 m. The critical spacing at which the stress starts to decrease is different for each track condition. For the soft track, the critical spacing L1 is 3.5 m and for the medium and stiff track, the critical spacing L1 is 3.0 m; the maximum bending stress at the rail base are nearly constant when the axle spacing L1 varies; the mean bending stress at the rail head follows the same pattern as that of the maximum bending stress at the rail head.
2. For the 115 RE rail and the 136 RE rail, when the axle spacing L1 varies from 2.0 m to 5.0 m, the maximum bending stresses at the rail head of both rail sections first increases and then decreases. However, the critical spacing for the two rail sections are different. The stress in the 136 RE rail decreases later than the 115 RE rail in the soft and medium track condition, while in the stiff track condition, the stresses of both rail sections start to decrease at the axle spacing L1=3.0 m. The maximum bending

stresses at the rail base of both the 115 RE rail and the 136 RE rail are nearly constant when the axle spacing L1 varies.

3. When relative locations of wheel loads to crossties vary, the maximum bending stress at the rail head (at the rail base) varies within a small range and the variation does not affect the general pattern of the relationship between the maximum bending stress at the rail head (at the rail base) and the axle spacing L1.
4. When wheel loads were moved to the rail gauge corner, the maximum bending stress at the rail head still follows a pattern of first increasing and then decreasing under the soft and medium track conditions. However, for the stiff track condition, the maximum bending stress at the rail head seems to decrease with the axle spacing L1 increasing. The maximum bending stress at the rail base seems to be constant under each track condition when the axle spacing L1 increases under each track modulus.

Based on these conclusions, it is suggested that the axle spacing L1 in the range of 3.0-3.5 m be avoided in railcar operation to reduce the bending stress generated in the rail under train passages. Special attention should be paid to the maximum bending stress at the rail head to ensure necessary maintenance is implemented before rail failure if the axle spacing L1 range of 3.0-3.5 m cannot be avoided in some cases.

5.1 Recommendation for future work

Four types of finite element models of different complexities combined with the Winkler model analysis were used for investigation in the thesis and the results from them match well. Despite the successful investigation on the relationship of the rail bending stress vs. axle spacing L1 under different track and loading conditions, there are some points that needs further study.

For future attempts, the first step can be a more thorough study to investigate the relationship of the rail bending stress vs. axle spacing L1 when wheel loads were applied at the rail gauge corner. For example, different rail sections can be used and the relative locations of wheel loads can also vary in this case.

Secondly, other factors, like temperature, can be taken into account to see their influence on the relationship between the rail bending stress and the axle spacing L1.

Thirdly, in addition to the rail bending stress, contact stress, the principal stress, etc., can be investigated to see how the variation of axle spacing L1 can affect them.

Finally, field tests or laboratory experiments should be conducted to obtain first hand data, thus providing comparison and guidance for future work.

The deflection results of the rail under different track and loading conditions from all types of numerical models were summarized and analyzed as attached in Appendix A at the end of the thesis. A dynamic analysis of the rail bending stress behavior when the axle spacing L1 varies is attached in Appendix B.

REFERENCES

Adin, M. A., Yankelevsky, D. Z., and Eisenberger, M. (1985). "Analysis of beams on bi-moduli elastic foundation." Computer methods in applied mechanics and engineering, 49(3), pp.319-330.

Aglan, H. A., and Fateh, M. (2006). "Fatigue damage tolerance of bainitic and pearlitic rail steels." International Journal of Damage Mechanics, 15(4), 393-410.

Ahlf, R. E. (1975). "M/W Costs: How they are affected by car weights and the track structure." Railway Track and Structures, 71(3).

Ali, A. H. A., Hameed, A. N., and Ibrahim, S. K. (2013). "Effect of railway track elements properties on stresses distribution." International Journal of Structural and Civil Engineering Research, 2 (2), pp.116-128.

American Railway Engineering Association. (1991). "Manual for railway engineering." Vol. I and Vol. II., Washington, DC.

American Railway Engineering & Maintenance-of-Way Association. (2003). "Practical Guide to Railway Engineering." American Railway Engineering & Maintenance-of-Way Association.

American Railway Engineering & Maintenance-of-way Association. (2006). "Economics of Railway Engineering and Operations—Construction and Maintenance Operations". Manual for Railway Engineering, Volume 4, Chapter 16, Part 10.

American Railway Engineering & Maintenance-of-way Association. (2009). AREMA Manual for Railway Engineering, Part 1, Design of rail.

American Railway Engineering & Maintenance-of-way Association. (2011). AREMA Manual for Railway Engineering, Volume 4.

Andersson, C., and Abrahamsson, T. (2002). "Simulation of interaction between a train in general motion and a track." Vehicle system dynamics, 38(6), pp.433-455.

Armstrong, J. H. (2008). "The Railroad: What it is, What it Does. The Introduction to Railroading." Simmons-Boardman Books, Inc., USA.

Biempica, C. B., del Coz Díaz, J. J., Nieto, P. G., et al. (2009). "Nonlinear analysis of residual stresses in a rail manufacturing process by FEM." Applied Mathematical Modelling, 33(1), pp.34-53.

Bowness, D., Lock, A. C., Powrie, W., et al. (2007). "Monitoring the dynamic displacements of railway track." Proceedings of the Institution of Mechanical Engineers, Part F: Journal of Rail and Rapid Transit, 221(1), pp.13-22.

Cannon, D. F., EDEL, K. O., Grassie, S. L., et al. (2003). "Rail defects: an overview." Fatigue & Fracture of Engineering Materials & Structures, 26(10), pp.865-886.

Clark, R. (2004). "Rail flaw detection: overview and needs for future developments." NDT & E International, 37(2), pp.111-118.

Connolly, D., Giannopoulos, A., and Forde, M. C. (2013). "Numerical modelling of ground borne vibrations from high speed rail lines on embankments." Soil Dynamics and Earthquake Engineering, 46, 13-19.

Cortie, M. B., and Garrett, G. G. (1988). "On the correlation between the C and m in the Paris equation for fatigue crack propagation." Engineering fracture mechanics, 30(1), 49-58.

Dahlberg, T. (2002). "Dynamic interaction between train and nonlinear railway track model." In *Proc. Fifth Euro. Conf. Struct. Dyn.*, Munich, Germany (pp. 1155-1160).

Dassault Systèmes Simulia Corp. "Abaqus 6.13 Analysis User's Guide, Chapter IV, Elements."

De Man, A. P. (2002). "DYNATRACK: A survey of dynamic railway track properties and their quality." Ph.D. Thesis, Delft University, Delft, Neitherlands.

Feng, H. (2011). "3D-models of railway track for dynamic analysis." MSc. Thesis, Royal Institute of Technology, Stockholm, Sweden.

Filonenko-Borodich, M. M. (1940). Some approximate theories of the elastic foundation. Uchenyie Zapiski Moskovskogo Gosudarstvennogo Universiteta Mekhanica, 46, pp.3-18.

Fowler G. and Don M. (2013). "Detail fracture defects, the Canadian TSB experience." Heavy haul seminar.

Gao Yin. (2013). “A 3D dynamic train-track interaction model to study track performance under trains running at a critical speed.” MSc. Thesis, Pennsylvania State University, USA.

Hay, W. W. (1982). “Railroad engineering (Vol. 1).” John Wiley & Sons.

Hibbeler, R. C. (2010). “Mechanics of materials (8th edition).” Pearson Prentice Hall, USA.

Hirao, M., Ogi, H., and Fukuoka, H. (1994). “Advanced ultrasonic method for measuring rail axial stresses with electromagnetic acoustic transducer.” Journal of Research in Nondestructive Evaluation, 5(3), 211-223.

Igwemezie, J. O., Kennedy, S. L., and Gore, N. R. (1993). “Residual stresses and catastrophic rail failure.” In Rail Quality and Maintenance for Modern Railway Operation (pp. 325-336). Springer Netherlands.

Iwnicki, S. (Ed.). (2006). “Handbook of railway vehicle dynamics.” CRC press.

Jeong, D. Y. (2001). “Progress in rail integrity research (No. DOT-VNTSC-FRA-01-03,).” Federal Railroad Administration, Office of Research and Development.

Jeong, D. Y., and Gordon, J. E. (2009). “Evaluation of rail test frequencies using risk analysis.” In *2009 Joint Rail Conference* (pp. 23-30). American Society of Mechanical Engineers.

Jeong, D. Y., and Perlman, A. B. (2011). “Estimating track capacity based on rail stresses and metal fatigue.” *Proceedings of the 2011 ASME Rail Transportation Division Fall Technical Conference*.

Jeong, D. Y., and Perlman, A. B. (2013). “Analysis of minimum rail size in heavy axle load Environment.” *2013 Joint Rail Conference. American Society of Mechanical Engineers*, pp.V001T01A001-V001T01A001.

John L. and Roy A.. (2015). “Guidelines to best practices for heavy haul railway operations: management of the wheel and rail interface.” IHHA.

Kennedy, J. (2011). “A full-scale laboratory investigation into railway track substructure performance and ballast reinforcement.” Ph.D. diss., Heriot-Watt University.

Kerr, A. D., & Shenton, H. W. (1985). “On the reduced area method for calculating the vertical track modulus.” American Railway Engineering Association Bulletin, 86(703), 416-429.

Kish, A., Samavedam, G. (2005). "Improved destressing of continuous welded rail for better management of rail neutral temperature." Transportation Research Record: Journal of the Transportation Research Board, (1916), 56-65.

Lewis, R., and Olofsson, U. (Eds.). (2009). Wheel-rail interface handbook. Elsevier.

Li, D., Hyslip, J., Sussmann, T., et al. (2002). Railway Geotechnics. CRC Press.

Lim, N. H., Park, N. H., and Kang, Y. J. (2003). "Stability of continuous welded rail track." Computers & Structures, 81(22), pp.2219-2236.

Liu, Y., Stratman, B., and Mahadevan, S. (2006). "Fatigue crack initiation life prediction of railroad wheels." International Journal of Fatigue, 28(7), 747-756.

Liu, Y., Liu, L., and Mahadevan, S. (2007). "Analysis of subsurface crack propagation under rolling contact loading in railroad wheels using FEM." Engineering fracture mechanics, 74(17), 2659-2674.

Lyons, M. L., Jeong, D. Y., and Gordon, J. E. (2009, January). "Fracture Mechanics Approach to Estimate Rail Wear Limits." In ASME 2009 Rail Transportation Division Fall Technical Conference (pp. 137-146). American Society of Mechanical Engineers.

Newman, J. C., Phillips, E. P., and Swain, M. H. (1999). "Fatigue-life prediction methodology using small-crack theory." International Journal of fatigue, 21(2), 109-119.

Newton, S. G., and Clark, R. A. (1979). "An investigation into the dynamic effects on the track of wheelflats on railway vehicles." Journal of Mechanical Engineering Science, 21(4), pp.287-297.

Nimbalkar, S., Indraratna, B., Dash, S. K., et al. (2012). "Improved performance of railway ballast under impact loads using shock mats." Journal of Geotechnical and Geoenvironmental Engineering, 138(3), pp.281-294.

Nordco Rail Services and Inspection Technologies (NRS&IT). "Nordco Rail Flaw Identification Handbook."

Nguyen Gia, K., Goicolea Ruigómez, J. M., and Gabaldón Castillo, F. (2011). "Dynamic Analysis of high Speed Railway Traffic Loads on Ballasted Track." *The Fifth International Symposium on Environmental Vibration*, Chengdu, China.

Nguyen, K., Goicolea, J. M., and Galbadon, F. (2012). "Comparison of dynamic effects of high-speed traffic load on ballasted track using a simplified two-dimensional and

full three-dimensional model." Proceedings of the Institution of Mechanical Engineers, Part F: Journal of Rail and Rapid Transit, 0954409712465710.

Orringer, O. (1988). "Crack propagation life of detail fractures in rails (No. DOT/FRA/ORD-88/13 FINAL REPO)."

Oscarsson, J. (2001). "Dynamic train-track interaction: linear and non-linear track models with property scatter." Ph.D. Thesis, Chalmers University of Technology, Gothenburg, Sweden.

Pasternak, P. L. (1954). "On a new method of analysis of an elastic foundation by means of two constants [Gosudarstvennoe Izdatelstvo Literaturi po Stroitelstvu I Arkhitekture]." Moscow: *USSR*.

Popp, K., Kruse, H., and Kaiser, I. (1999). "Vehicle-track dynamics in the mid-frequency range." Vehicle System Dynamics, 31(5-6), pp.423-464.

Powrie, W., Yang, L. A., and Clayton, C. R. (2007). "Stress changes in the ground below ballasted railway track during train passage." Proceedings of the Institution of Mechanical Engineers, Part F: Journal of Rail and Rapid Transit, 221(2), 247-262.

Raymond, G. P. (1985). "Analysis of track support and determination of track modulus." In Transportation Research Record 1022, TRB, National Research Council, Washington, D. C..

Reissner, E. (1958). "A note on deflections of plates on a viscoelastic foundation." Journal of Applied Mechanics, 25(1), pp.144-145.

Remennikov, A. M. and Kaewunruen, S. (2008). "A review of loading conditions for railway track structures due to train and track vertical interaction." Structural Control and Health Monitoring, 15(2), 207-234.

Roberts, T., and Talebzadeh, M. (2003). "Acoustic emission monitoring of fatigue crack propagation." Journal of Constructional Steel Research, 59(6), 695-712.

Sadeghi, J. and Barati, P.. (2010). "Evaluation of conventional methods in Analysis and Design of Railway Track System." International Journal of Civil Engineering, 8(1), pp.44-55.

Sadeghi, J., and Shoja, S. (2015). "Influences of track and rolling stock parameters on the railway load amplification factor." Proceedings of the Institution of Mechanical Engineers, Part F: Journal of Rail and Rapid Transit, 0954409715587731.

Selig, E. T., and Li, D. (1994). “Track modulus: Its meaning and factors influencing it.” Transportation Research Record, 1470, pp.47-54.

Seo, J., Kwon, S., Jun, H., et al. (2011). “Numerical stress analysis and rolling contact fatigue of White Etching Layer on rail steel.” International Journal of Fatigue, 33(2), pp.203-211.

Shahin, M. Y. (1986). “Development of the US Army Railroad Track Maintenance Management System (RAILER).” No. CERL-TR-M-86/01. Construction Engineering Research Lab (Army) Champaign IL.

Shahu, J. T., Kameswara Rao, N. S. V., and Yudhbir. (1999). “Parametric study of resilient response of tracks with a sub-ballast layer.” Canadian Geotechnical Journal, 36(6), 1137-1150.

Sheng, X., Thompson, D. J., Jones, C. J., et al. (2006). “Simulations of roughness initiation and growth on railway rails.” Journal of Sound and Vibration, 293(3), 819-829.

Simon Iwnicki. (2006). “Handbook of railway vehicle dynamics.” CRC Press, Taylor & Francis Group, New York, USA.

Skoglund, K. A. (2002). “A study of some factors in mechanistic railway track design.” Doctor of Engineering Thesis, Norwegian University of Science and Technology.

Steffens, D. M. (2005). “Identification and development of a model of railway track dynamic behaviour.” MSc. Thesis, Queensland University of Technology.

Stuart L Grassie, (1993). “Dynamic Models of the Track and Their Uses. Chapter Rail Quality and Maintenance for Modern Railway Operation”, pp 165-183.

Szelążek, J. (1992). “Ultrasonic measurement of thermal stresses in continuously welded rails.” NDT & E International, 25(2), 77-85.

Torstensson, P. T., Pieringer, A., and Nielsen, J. C. (2014). “Simulation of rail roughness growth on small radius curves using a non-Hertzian and non-steady wheel–rail contact model.” Wear, 314(1), 241-253.

Transportation Safety Board of Canada. Rail. Retrieved 8 February, 2013, from http://www.tsb.gc.ca/eng/rail/index.asp.

Transportation Safety Board of Canada. (2006). Railway investigation report, R06C0104.

Transportation Safety Board of Canada. (2008). Railway Investigation Report, R08C0164.

Transportation Safety Board of Canada. (2010). Railway Investigation Report, R10M0026.

Transportation Safety Board of Canada. Statistical summary-railway occurrences 2015. Retrieved 19 July, 2016, from http://www.tsb.gc.ca/eng/stats/rail/2015/sser-ssro-2015.asp?pedisable=true.

Vantuono, W. (2008). "John H. Armstrong's The Railroad What it is, What it does, the Introduction to Railroading." Simmons-Boardman Books Inc..

Vlasov, V. Z. (1949). "Structural mechanics of thin-walled three-dimensional systems." Stroiizdat, Moscow.

Vlasov, V. Z., and Leontiev, N. N. (1966). "Beams, plates, and shells on elastic foundations", translated from Russian by Israel program for scientific translations, NIST No. N67-14238.

Winkler, E. (1867). Die Lehre von der Elastizität und Festigkeit, Verlag H. Dominikus, Prague, Czechoslovakia.

Yang, L. A., Powrie, W., and Priest, J. A. (2009). "Dynamic stress analysis of a ballasted railway track bed during train passage." Journal of Geotechnical and Geoenvironmental Engineering, 135(5), pp.680-689.

Yujiang, Z., Jacinda, C., Kevin, K., et al. (2007). "Real Time Prediction of Rail Temperature." In *AREMA 2007 Annual Conference*, Chicago, USA.

Zerbst, U., Lundén, R., Edel, K. O., et al. (2009). "Introduction to the damage tolerance behaviour of railway rails–a review." Engineering fracture mechanics, 76(17), 2563-2601.

Zhao, X., Li, Z., and Liu, J. (2011). "Wheel–rail impact and the dynamic forces at discrete supports of rails in the presence of singular rail surface defects." Proceedings of the Institution of Mechanical Engineers, Part F: Journal of Rail and Rapid Transit, 0954409711413975.

APPENDIX A: DEFLECTION OF THE RAIL

Under the track modulus of 13.79 MPa, when the axle spacing L1 varies from 2.0 m to 5.0 m, the deflections along the rail from the Winkler Model, the Rail on Continuous Foundation Model, the Rail on One layer of Discrete Spring Supports Model, the Rail on Two layers of Discrete Spring Supports Model and the Rail on Continuum Foundation Model were shown in Figure A.1 as follows.

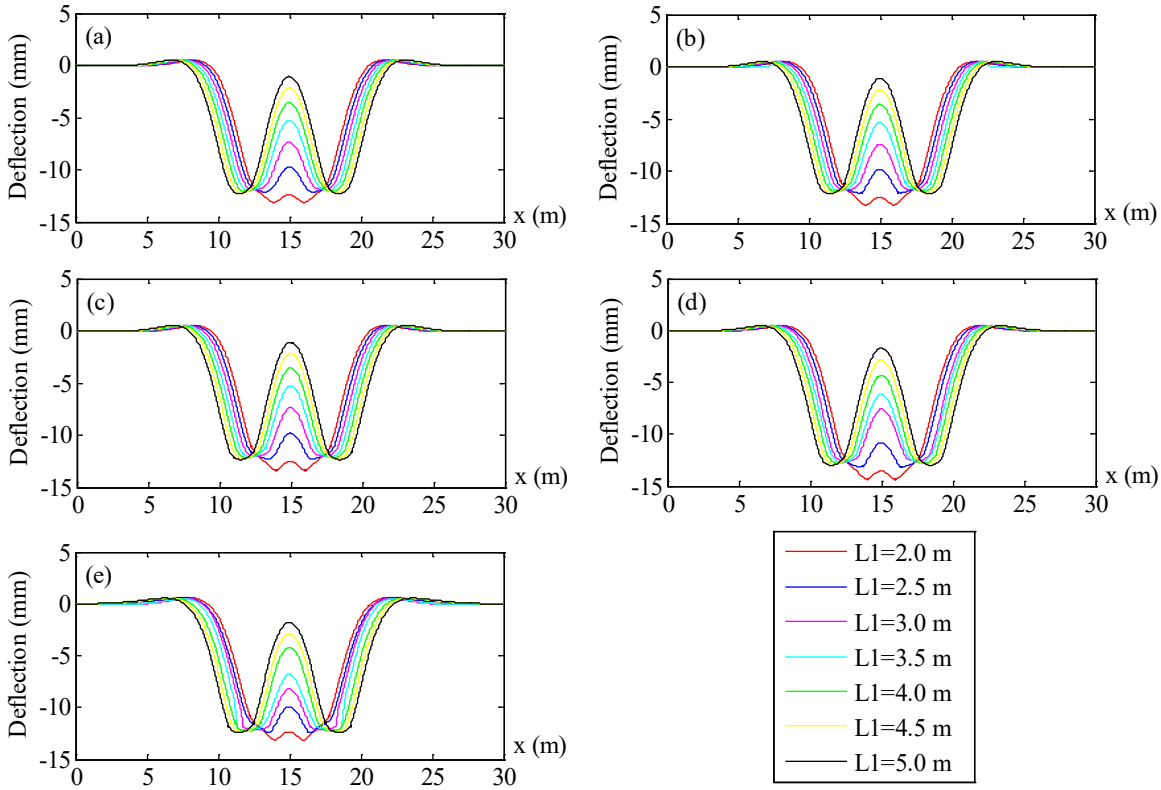

Figure A.1. Deflection along the rail under the track modulus of 13.79 MPa from the (a) Winkler Model (b) Rail on Continuous Foundation Model (c) Rail on One layer of Discrete Spring Supports Model (d) Rail on Two layers of Discrete Spring Supports Model and (e) Rail on Continuum Foundation Model when the axle spacing L1 varies

In Figure A.1, the horizontal axis represents the longitudinal coordinate along the rail and the vertical axis represents the deflection of the rail. The curves with different colors represent the results at the axle spacing L1 of 2.0 m (red line), 2.5 m (blue line), 3.0 m

(magenta line), 3.5 m (light blue line), 4.0 m (green line), 4.5 m (yellow line) and 5.0 m (black line).

From Figure A.1 (a) to Figure A.1 (e), it can be seen that, the deflection at the middle of the rail, i.e. x=15 m, varies obviously with the axle spacing L1 increasing from 2.0 m to 5.0 m, while the deflection at the wheel locations varies much less.

Under the track modulus of 27.58 MPa, when the axle spacing L1 varies from 2.0 m to 5.0 m, the deflections along the rail from the Winkler Model, the Rail on Continuous Foundation Model, the Rail on One layer of Discrete Spring Supports Model, the Rail on Two layers of Discrete Spring Supports Model and the Rail on Continuum Foundation Model were shown in Figure A.2 as follows.

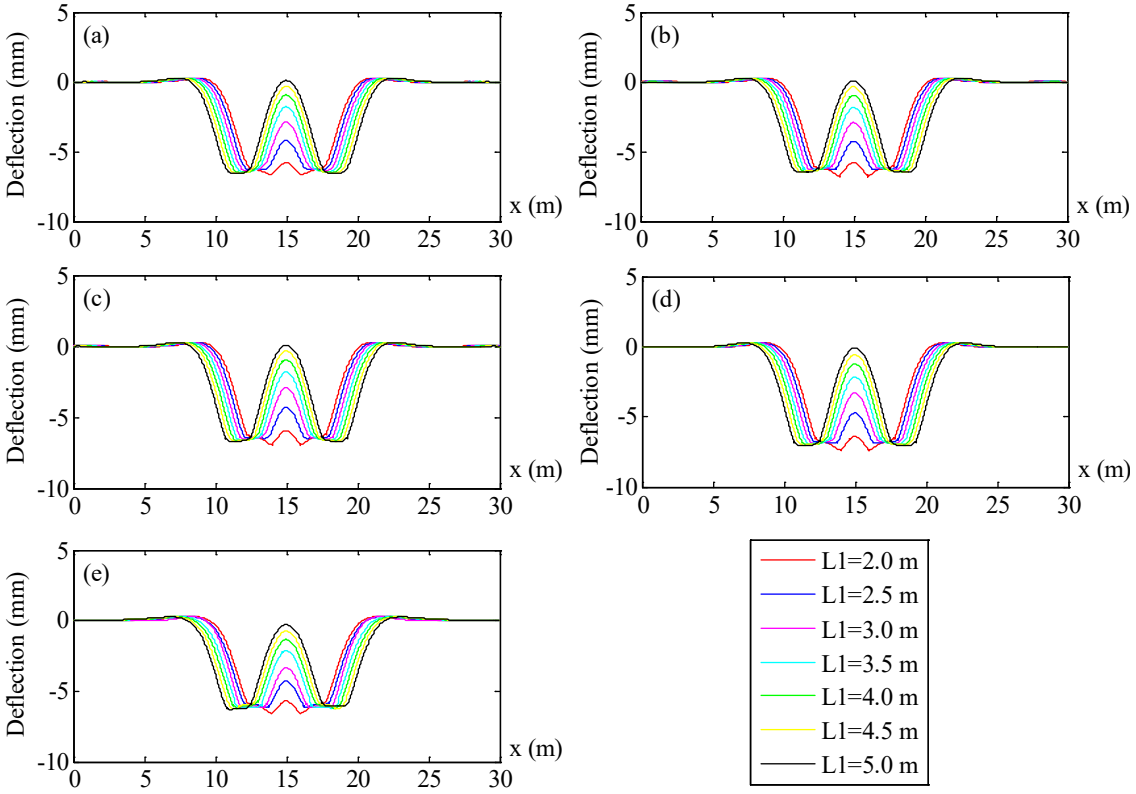

Figure A.2. Deflection along the rail under the track modulus of 27.58 MPa from the (a) Winkler Model (b) Rail on Continuous Foundation Model (c) Rail on One layer of Discrete Spring Supports Model (d) Rail on Two layers of Discrete Spring Supports Model and (e) Rail on Continuum Foundation Model when the axle spacing L1 varies

It can also be seen that the deflection at the middle of the rail varies obviously with axle spacing L1 increasing, while the deflection at the wheel location varies little.

Under the track modulus of 41.37 MPa, when the axle spacing L1 varies from 2.0 m to 5.0 m, the deflections along the rail from the Winkler Model, the Rail on Continuous Foundation Model, the Rail on One layer of Discrete Spring Supports Model, the Rail on Two layers of Discrete Spring Supports Model and the Rail on Continuum Foundation Model were shown in Figure A.3 as following.

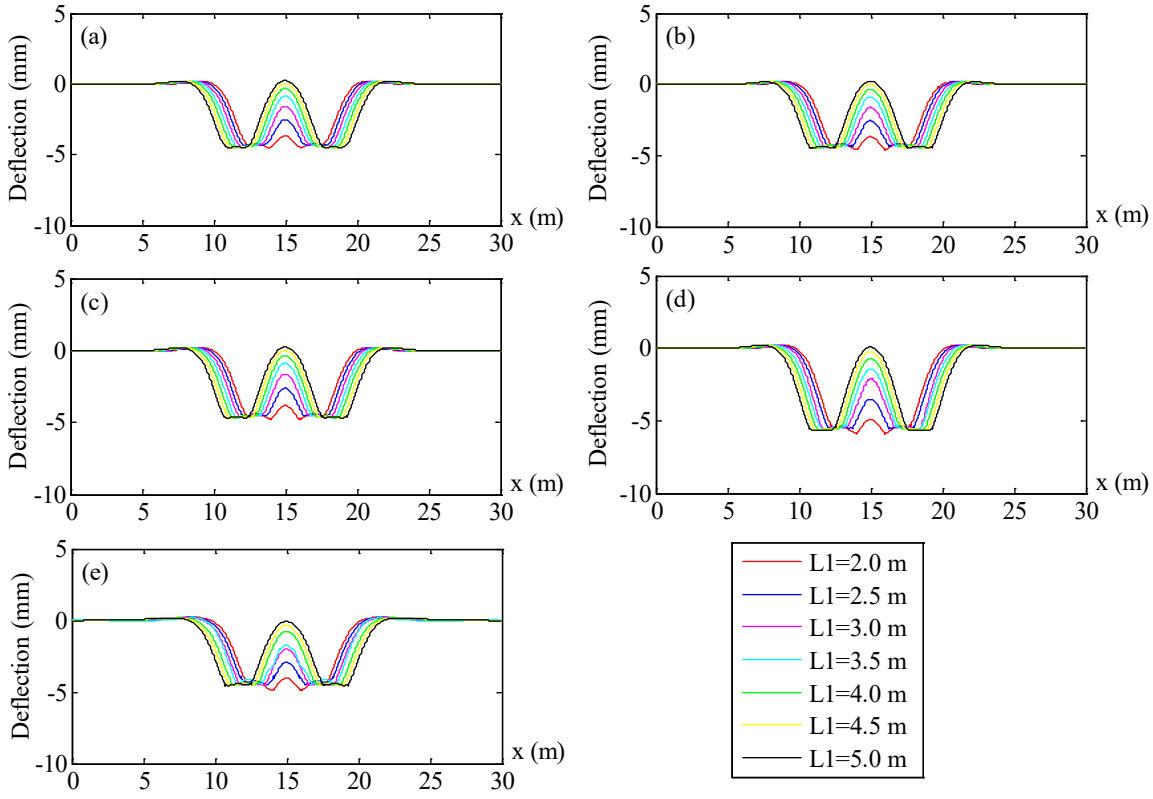

Figure A.3. Deflection along the rail under the track modulus of 41.37 MPa from the (a) Winkler Model (b) Rail on Continuous Foundation Model (c) Rail on One layer of Discrete Spring Supports Model (d) Rail on Two layers of Discrete Spring Supports Model and (e) Rail on Continuum Foundation Model when the axle spacing L1 varies

From Figure A.3, the same conclusions as in Figure A.1 and Figure A.2 can be obtained that, the deflection at the middle of the rail varies obviously when axle spacing L1 increases while the deflection at the wheel location varies much less.

A comparison of the deflection results from different types of models at each axle spacing L1 under the track modulus of 13.79 MPa was shown in Figure A.4. Figure A.4 (a) to Figure A.4 (f) represent the results at the axle spacing L1=2.0 m, 2.5 m, 3.0 m, 3.5 m, 4.0 m, 4.5 m and 5.0 m respectively. In each figure, the red curve represents the deflection of the rail from the Winkler model, the blue curve represents the deflection of the rail from the Rail on Continuous Foundation Model, the black curve represents the deflection from the Rail on One layer of Discrete Spring Supports Model, the green curve represents the deflection from the Rail on Two layer of Discrete Spring Supports Model and the magenta curve represents the deflection from the Rail on Continuum Foundation Model. The horizontal axis in each figure represents the longitudinal coordinate of the rail and the vertical axis represents the deflection of the rail.

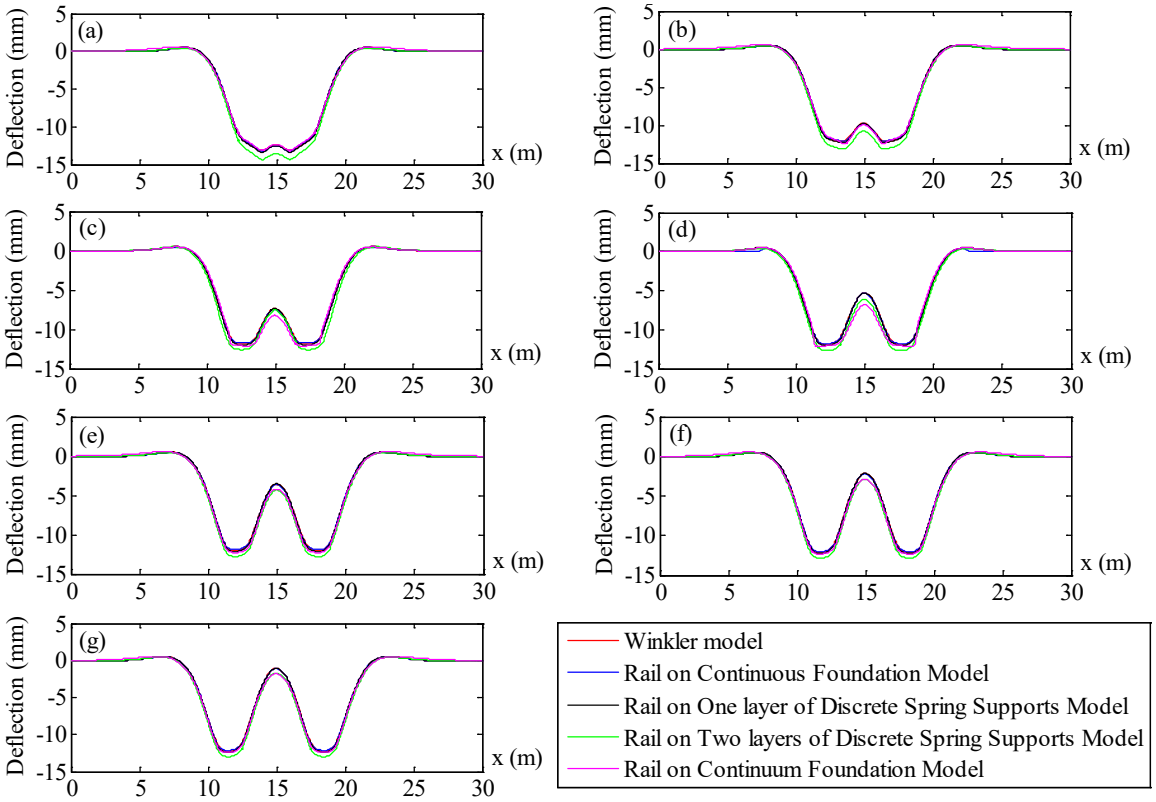

Figure A.4. Comparison of the deflection results from different types of models under the track modulus of 13.79 MPa at the axle spacing of (a) L1=2.0 m (b) L1=2.5 m (c) L1=3.0 m (d) L1=3.5 m (e) L1=4.0 m (f) L1=4.5 m and (g) L1=5.0 m

From Figure A.4, it can be seen that, in general, at each axle spacing L1, the deflections along the rail from different types of models match well.

Under the track modulus of 27.58 MPa and 41.37 MPa, the comparison of deflection results from different types of models at each axle spacing L1 was shown in Figure A.5 and Figure A.6 respectively. When the track modulus is 27.58 MPa, the deflections along the rail at each axle spacing L1 match well for different types of models. When the track modulus is 41.37 MPa, it seems that the deflection of the rail at each axle spacing L1 from the Rail on Two layers of Discrete Spring Supports Model is always larger than that from other types of models, while the deflections of the rail from other types of models match well at each axle spacing L1.

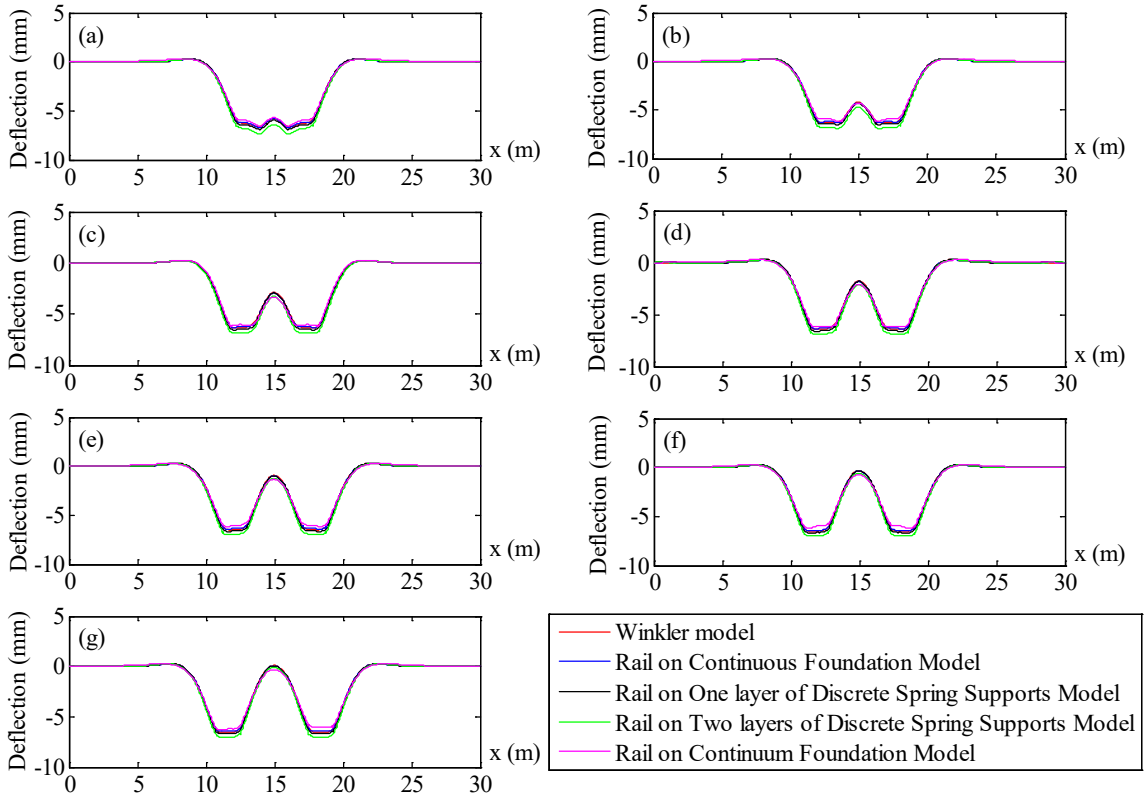

Figure A.5. Comparison of the deflection results from different types of models at each axle spacing L1 under the track modulus of 27.58 MPa at the axle spacing of (a) L1=2.0 m (b) L1=2.5 m (c) L1=3.0 m (d) L1=3.5 m (e) L1=4.0 m (f) L1=4.5 m and (g) L1=5.0 m

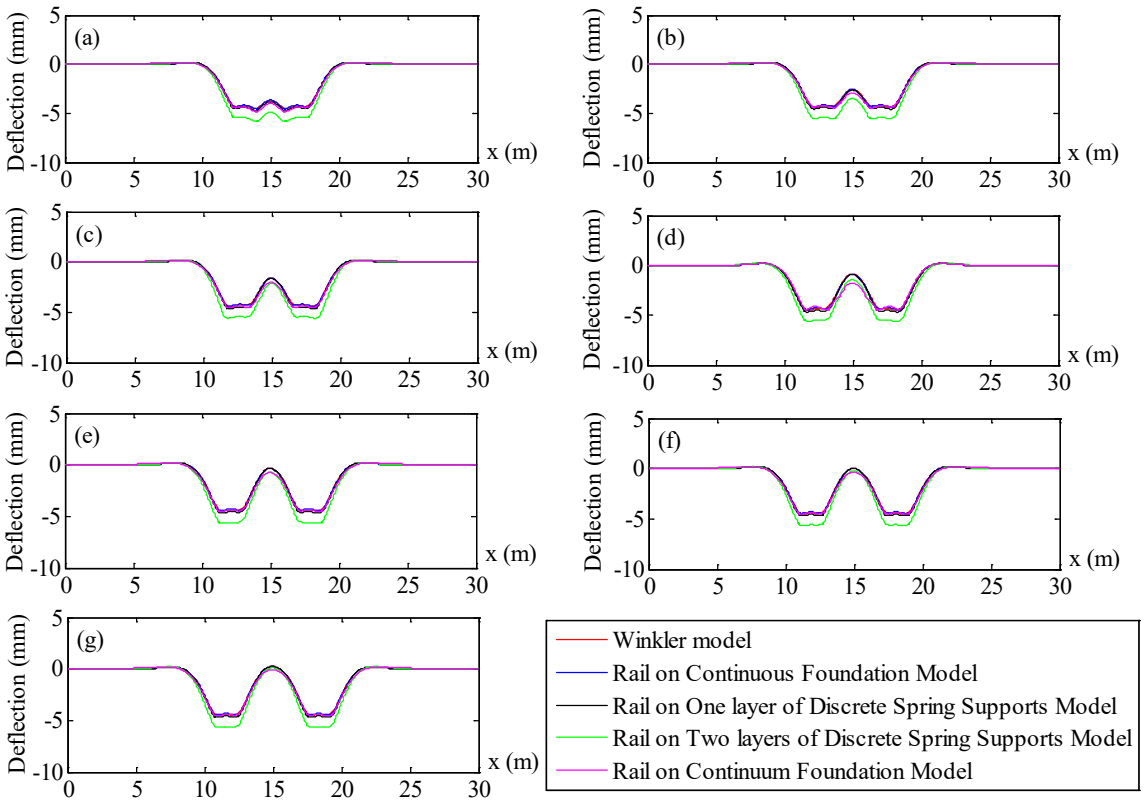

Figure A.6. Comparison of the deflection results from different types of models under the track modulus of 41.37 MPa at the axle spacing of (a) L1=2.0 m (b) L1=2.5 m (c) L1=3.0 m (d) L1=3.5 m (e) L1=4.0 m (f) L1=4.5 m and (g) L1=5.0 m

Under each track modulus, when the axle spacing L1 varies from 2.0 m to 5.0 m, the maximum deflections of the rail from different types of models were shown as follows in Figure A.7. In Figure A.7, the red curve with "×" markers represents the results under the track modulus of 13.79 MPa, the blue curve with "○" markers represents the results under the track modulus of 27.58 MPa, and the magenta curve with "□" markers represents the results under the track modulus of 41.37 MPa. Figure A.7 (a) to Figure A.7 (e) represents the results from the Winker Model, the Rail on Continuous Foundation Model, the Rail on One layer of Discrete Spring Supports Model, the Rail on Two layer of Discrete Spring Supports Model, and the Rail on Continuum Foundaiton Model respectively.

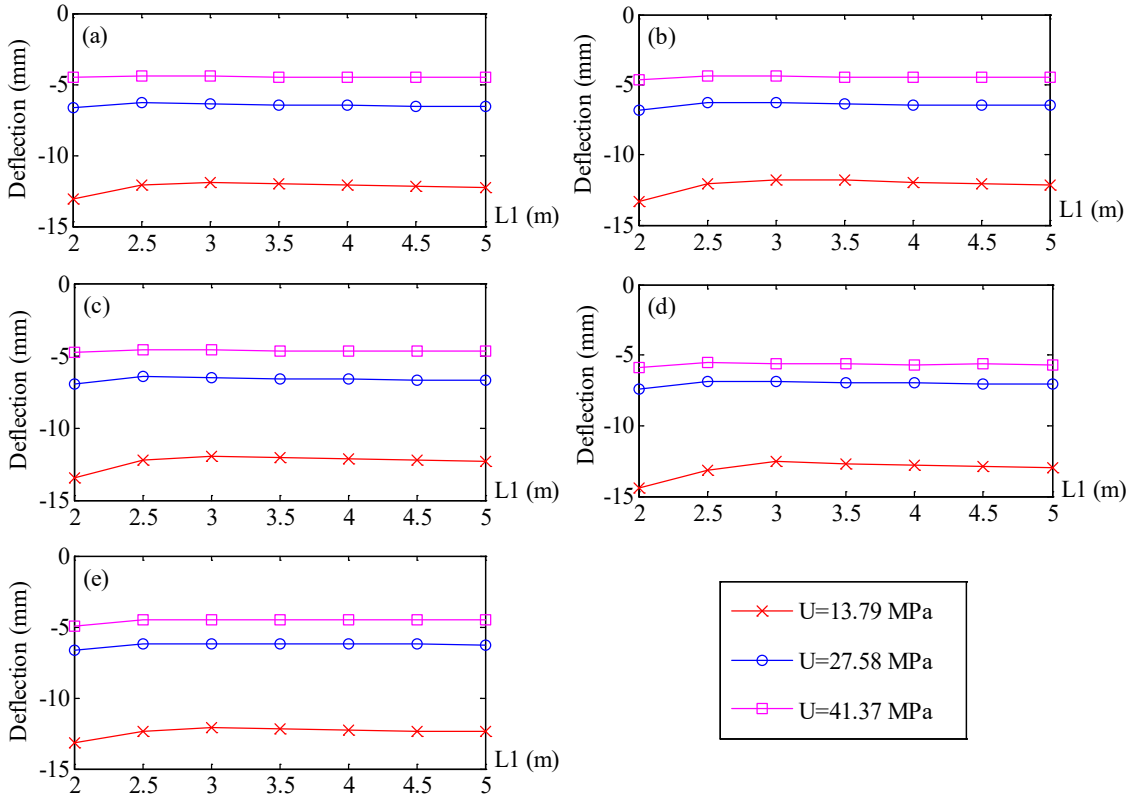

Figure A.7. The maximum deflection of the rail vs. axle spacing L1 under each track modulus from the (a) Winkler Model (b) Rail on Continuous Foundation Model (c) Rail on One layer of Discrete Spring Supports Model (d) Rail on Two layers of Discrete Spring Supports Model and (e) Rail on Continuum Foundation Model when the axle spacing L1 varies

From Figure A.7, it shows that, under the track modulus of 27.58 MPa and 41.37 MPa, from all types of models, the maximum deflections of the rail are nearly constant when the axle spacing L1 varies from 2.0 m to 5.0 m. When the track modulus is 13.79 MPa, the maximum deflection of the rail from each type of model first increases when the axle spacing L1 increases from 2.0 m to 3.0 m and then becomes nearly constant when the axle spacing L1 increases from 3.0 m to 5.0 m.

Figure A.8 provides a comparison of the maximum deflection of the rail from different types of models under each track modulus when the axle spacing L1 varies. The red curve with "◊" markers represents the results from the Winkler Model, the blue curve with "◁" markers represents that from the Rail on Continuous Foundation Model, the black curve with "▷" markers represents that from the Rail on One layer of Discrete Spring Supports

Model, the green curve with "Δ" markers represents that from the Rail on Two layers of Discrete Spring Supports Model and the magenta curve with "▽" markers represents that from the Rail on Continuum Foundation Model. Under each track modulus, the maximum deflection of the rail from the Rail on Two layers of Discrete Spring Supports Model is always larger than that from other types of models. However, the maximum deflections of the rail from all types of models follow the same pattern when the axle spacing L1 varies.

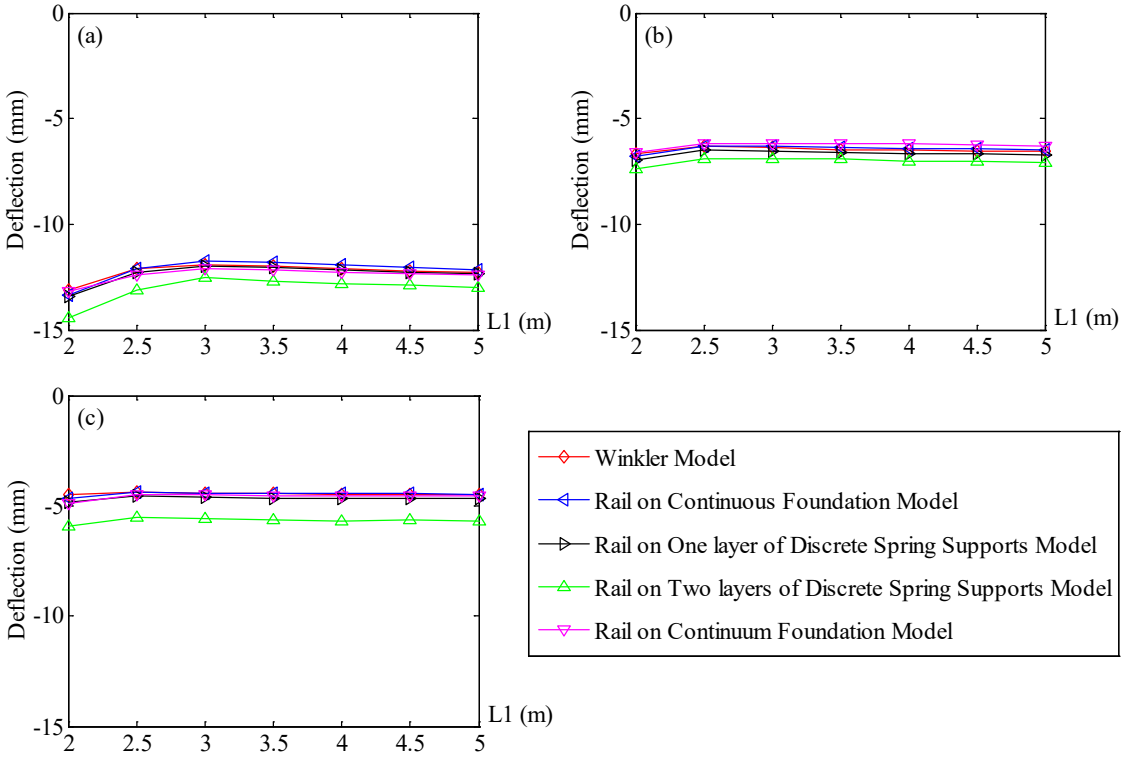

Figure A.8. Comparison of the maximum deflection of the rail from different types of models under the track modulus of (a) U=13.79 MPa (b) U=27.58 MPa and (c) U=41.37 MPa

Under each track modulus, when the axle spacing L1 varies from 2.0 m to 5.0 m, the deflections at the middle of the rail corresponding to reverse bending from different types of models were shown in Figure A.9 as follows.

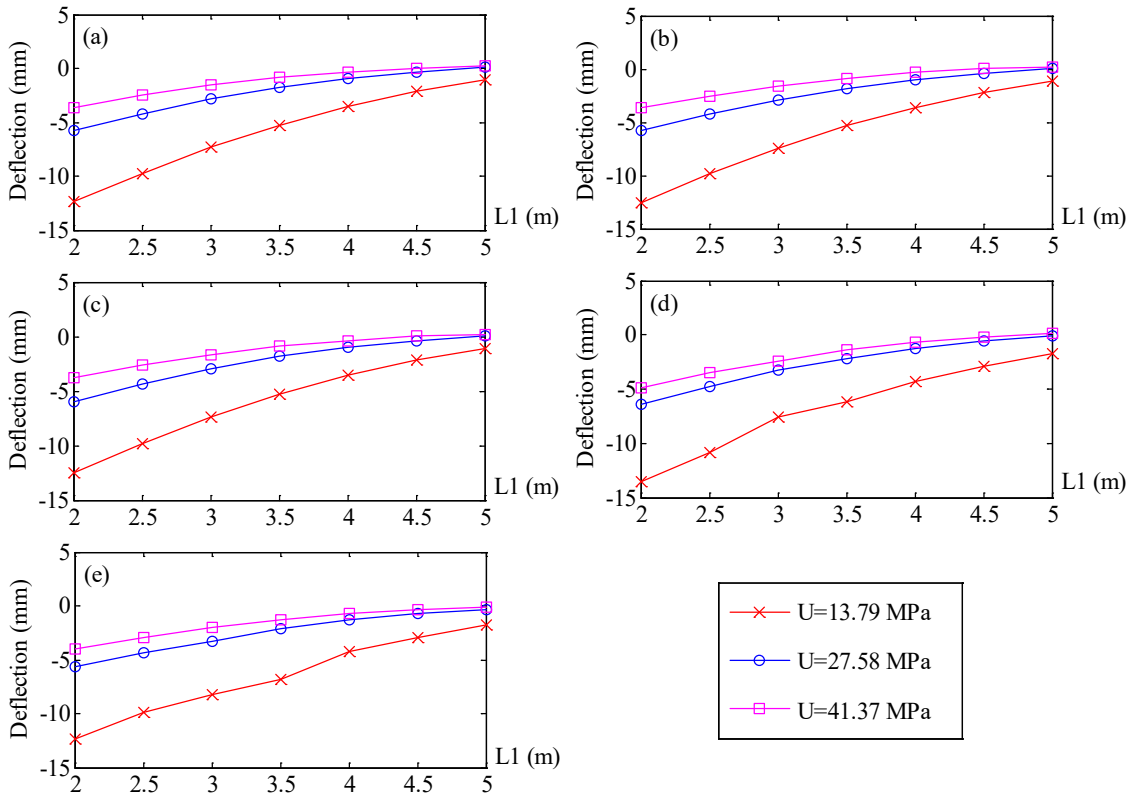

Figure A.9. The deflection at the middle of the rail vs. axle spacing L1 under each track modulus from the (a) Winkler Model (b) Rail on Continuous Foundation Model (c) Rail on One layer of Discrete Spring Supports Model (d) Rail on Two layers of Discrete Spring Supports Model and (e) Rail on Continuum Foundation Model when the axle spacing L1 varies

It shows that, under each track modulus, the deflection at the middle of the rail increases with the axle spacing L1 increasing from 2.0 m to 5.0 m from all types of models. In addition, the deflection at the middle of the rail decreases when the track modulus increases for each axle spacing L1, which is expected.

Figure A.10 gives a comparison of the deflections at the middle of the rail from different types of models. It can be seen that, in general, the deflections at the middle of the rail from different types of models when the axle spacing L1 varies are close to each other which is most obviously seen under the track modulus of 27.58 MPa.

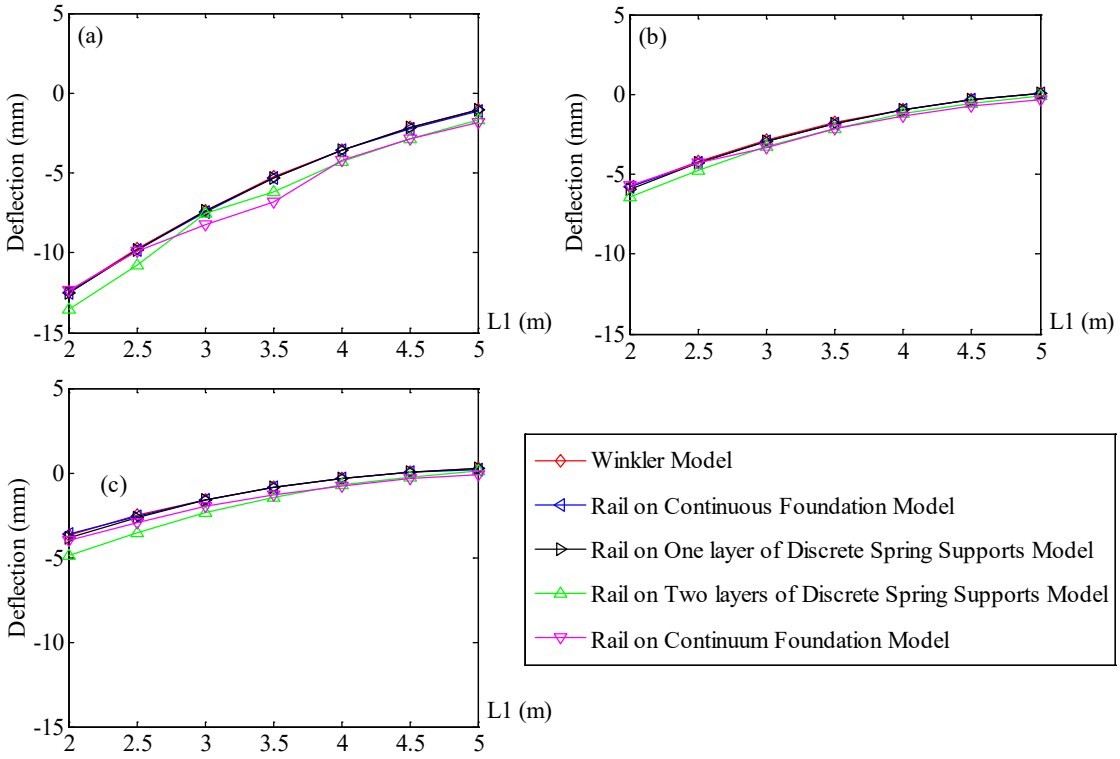

Figure A.10. Comparison of the deflection at the middle of the rail from different types of models under the track modulus of (a) U=13.79 MPa (b) U=27.58 MPa and (c) U=41.37 MPa

APPENDIX B: DYNAMIC ANALYSIS OF THE RAIL BENDING STRESS WHEN THE AXLE SPACING L1 VARIES

When the train is running over the rail, a corrective factor should be introduced when calculating the load acting on the rail due to dynamic effects. The load in dynamic condition can be called dynamic wheel load and the corrective factor is called the dynamic impact factor φ (Sadeghi and Barati, 2010). The dynamic wheel load P_d can be calculated by the product of the dynamic impact factor and the static wheel load P_s, as expressed in Equation B.1 (Remennikov, 2008).

$$P_d = \varphi * P_s \tag{B.1}$$

Different formulas have been proposed by railway researchers and authorities for the estimation of the dynamic impact factor when considering various parameters (Sadeghi and Shoja, 2015). The AREMA manual (2011) provides a way to estimate the dynamic factor by using Equation B.2 when the train speed is taken into account.

$$\varphi = (1 + 5.21\frac{v(km/h)}{D(mm)}) = (1 + 0.33\frac{v(mph)}{D(inch)}) \tag{B.2}$$

where, v is the train speed, D is the truck wheel diameter.

From Equation B.1 and Equation B.2, it is obvious that the wheel load acting on the rail is amplified when there is speed, thus generating higher stress level in the rail.

B.1 Establishment of the railway track system model under dynamic loads

According to the code of Federal Railroad Administration, the operating speed limits for different classes of track are listed in Table B.1 as follows.

Most freight railways in Canada are Class 1 to Class 3 tracks. In our model for dynamic analysis, the speed of 18 m/s was used, corresponding to the maximum allowable operating

speed for freight trains on the Class 3 track, which is 40 mph. The speed was applied to wheels through velocity boundary conditions on their reference points.

Table B.1. The operating speed limits by class of track—(49 CFR § 213.4, 49 CFR § 213.9, 49 CFR § 213.307)

Track classification	The maximum allowable operating speed for freight trains	The maximum allowable operating speed for passenger trains
Excepted track	10 mph	N/A
Class 1 track	10 mph	15 mph
Class 2 track	25 mph	30 mph
Class 3 track	40 mph	60 mph
Class 4 track	60 mph	80 mph
Class 5 track	80 mph	90 mph
Class 6 track	110 mph	110 mph
Class 7 track	125 mph	125 mph
Class 8 track	160 mph	160 mph
Class 9 track	200 mph	200 mph

The material properties of the rail, crossties, and wheels are the same as that described in Chapter 3. However, some components in the track system are made of materials with complicated or even unknown constitutive equations, for example, railpads and ballast. The behavior of these components could be time-, frequency-, and load-dependent (Andersson and Abrahamsson, 2002).

Linear viscous damping is commonly used for modeling the railpad damping, which is proportional to the deformation rate (Iwnicki, 2006). Based on a review of the simulation and experimental work of former researchers, the railpad damping usually falls in the range of 10^1-10^3 kN.s/m. For example, Gao (2013) used the railpad damping of 10 kN.s/m, 100 kN.s/m and 1000 kN.s/m to study their influence on the rail surface displacement and the maximum wheel force on ballast top in low speed and critical speed conditions. Stuart (1993) provided 7 kN.s/m and 70 kN.s/m for the railpad damping based on experimental work. Dahlberg (2002) used 700 kN.s/m as the railpad damping and conducted a comparison between the simulation and experimental results. In our investigation, railpad

damping of 7 kN.s/m, 70 kN.s/m and 700 kN.s/m were applied in models to see how it will influence the rail bending stress behavior.

The damping of the ballast is modeled by the material property definition in ABAQUS by using Rayleigh damping (Nguyen et al., 2012) as expressed in Equation B.3. There are two damping factors in Equation B.3, i.e. *a* for mass proportional damping and *b* for stiffness proportional damping.

$$\mathbf{C}=a\mathbf{M}+b\mathbf{K} \tag{B.3}$$

where, **C**, **M**, **K** are the damping, mass and stiffness matrix of the system.

The two damping factors can be determined from two given damping ratios corresponding to two circular frequencies of vibration, covering the frequency range of interest, as shown in Equation B.4 (Nimbalkar, et al. 2012).

$$\frac{1}{2}\begin{bmatrix} 1/\omega_1 & \omega_1 \\ 1/\omega_2 & \omega_2 \end{bmatrix}\begin{Bmatrix} a \\ b \end{Bmatrix}=\begin{bmatrix} \xi_1 \\ \xi_2 \end{bmatrix} \tag{B.4}$$

where, ξ_1, ξ_2 are damping ratios and ω_1, ω_2 are circular frequencies of vibration in the system.

However, exact values of damping ratios for every mode of vibrations in the system are rarely available, thus usually only one uniform value of damping ratio is commonly assumed to calculate the damping factors (Popp et al., 1999). So the formulation becomes as follows:

$$a=\xi\frac{2\omega_1\omega_2}{\omega_1+\omega_2},\ b=\xi\frac{2}{\omega_1+\omega_2} \tag{B.5}$$

where, ξ is the damping ratio, determined as 10% in this study. The properties of ballast and subgrade, mainly influence the track dynamic responses in the mid-frequency range around 20-300 Hz (Popp et al., 1999; Feng, 2011; De Man, 2002) due to the vibration of rail-crossties over the ballast and subgrade layer. Therefore, in this range, it can be said that the ballast and subgrade have strong effects on track dynamic responses. In this study, the circular frequency range of [125,1885] rad/s was applied, in which the properties of ballast and subgrade have strong effects on the track dynamics (Nguyen et al, 2012). Thus,

the Rayleigh damping factor a and b can be obtained as 23.445 and $9.9502*10^{-5}$, respectively.

B.2 Sensitivity analysis on the dimension and boundary condition in the model

The model established for dynamic analysis is based on the Rail on Continuum Foundation Model but with revision for dynamic analysis. The length of the track in the model for dynamic analysis is 109 m and the depth of the continuum foundation is 30 m, which is enough to eliminate the boundary effects (Yang, et al., 2009). A section of 18 m in the middle of the rail was fine meshed with an element size of 10 mm, and the other parts of the rail are meshed with an element size of 40 mm. The ABAQUS/Explicit solver (ABAQUS 6.13-4 version, 2013) was used for solution.

To determine the suitable width and boundary condition of the continuum foundation layer in the model under dynamic loads, a sensitivity analysis on it was conducted. When the width of the continuum foundation is 10 m, 20 m, 30 m, and 50 m, four models were established, which are denoted as Model 1, Model 2, Model 3, and Model 4, respectively. Another model was established in which the continuum foundation width is 50 m while the symmetric boundary condition was applied on the outer plane of the continuum foundation was established, as denoted by Model 5. From each model, the maximum bending stresses at the rail head under different track modulus were extracted and summarized in Table B.2. The error between the results from these models was calculated and shown in the Error columns.

Table B.2. The maximum bending stress at the rail head under each track modulus

Type	U=13.79 MPa		U=27.58 MPa		U=41.37 MPa	
	Stress (MPa)	Error (%)	Stress (MPa)	Error (%)	Stress (MPa)	Error (%)
Model 1	50.78		44.71		44.22	
Model 2	52.96	-4.12	49.89	-10.38	50.02	-11.60
Model 3	54.15	-2.20	54.34	-8.19	54.81	-8.74
Model 4	53.32	1.56	53.92	0.78	53.63	2.20
Model 5	53.54	-0.41	54.59	-1.23	54.03	-0.74

It shows that, when width of the continuum foundation increases from 10 m to 50 m, the error of the maximum bending stress at the rail head decreases under each track modulus. When the width is 50 m, the error between Model 3 and Model 4 is already small, which is 1.56%, 0.78% and 2.20% respectively under the track modulus of 13.79 MPa, 27.58 MPa and 41.37 MPa. When symmetric boundary condition was added to the continuum foundation, corresponding to Model 5, the error decreases further, with a maximum error of -1.23% under the track modulus of 27.58 MPa, which is acceptable for analysis in engineering.

The maximum deflection of the rail under different track modulus were extracted and summarized in Table B.3. The error between the results from these models was calculated and shown in the Error columns in this table. Similar conclusions can be obtained indicating that, when width of the continuum foundation increases from 10 m to 50 m, the error of the maximum deflection of the rail decreases under each track modulus. When the width is 50 m, the error between Model 3 and Model 4 is within 5% under each track modulus. When the symmetric boundary condition was added to the continuum foundation, corresponding to Model 5, the error decreases more, with an error of 0.00%, 0.08% and 0.00% under the track modulus of 13.79 MPa, 27.58 MPa, and 41.37 MPa respectively.

Table B.3. The maximum deflection of the rail under each track modulus

Type	*U*=13.79 MPa		*U*=27.58 MPa		*U*=41.37 MPa	
	Deflection (mm)	Error (%)	Deflection (mm)	Error (%)	Deflection (mm)	Error (%)
Model 1	19.53		13.16		10.86	
Model 2	18.94	3.12	12.70	3.62	10.40	4.42
Model 3	18.98	-0.21	12.72	-0.16	10.43	-0.29
Model 4	18.22	4.17	12.26	3.75	10.04	3.88
Model 5	18.22	0.00	12.25	0.08	10.04	0.00

In general, when the width of the continuum foundation reaches 50 m and the symmetric boundary condition is applied on the outer plane of the foundation layer, the maximum

bending stress at the rail head and the maximum deflection of the rail have both come to be convergent. Thus, in later analysis, Model 5 will be used.

B.3 Results

When the railpad damping is 70 kN.s/m and the axle spacing L1 varies from 2.0 m to 5.0 m, the maximum deflections of the rail were shown in Figure B.1. It seems that, when the axle spacing L1 increases, the rail maximum deflection decreases for each track modulus. The amplification factors of rail deflection under dynamic wheel loads compared with that under static loads were calculated and shown in Table B.4. It seems that the amplification factor increases when the track modulus increases. In addition, under each track modulus, with the axle spacing L1 increasing, the amplification factor seems to be decreasing.

Table B.4. Amplification factors of the maximum deflection of the rail

L1	2.0 m	2.5 m	3.0 m	3.5 m	4.0 m	4.5 m	5.0 m
U=13.79 MPa	1.38	1.43	1.43	1.39	1.34	1.31	1.27
U=27.58 MPa	1.85	1.92	1.85	1.79	1.73	1.67	1.61
U=41.37 MPa	2.04	2.14	2.06	1.99	1.92	1.85	1.79

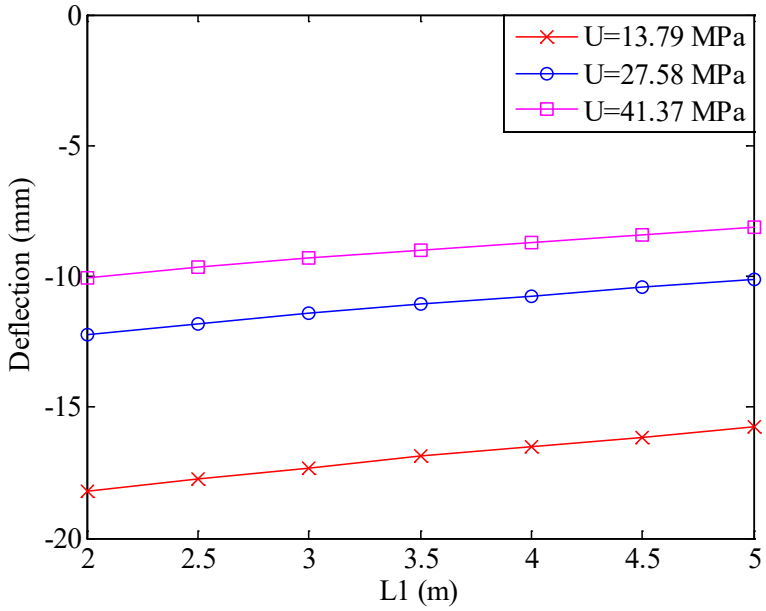

Figure B.1. The maximum deflection of the rail vs. axle spacing L1 under each track modulus

Under each track modulus, when the railpad damping is 7 kN.s/m, 70 kN.s/m, and 700 kN.s/m respectively, at the axle spacing L1=2.0 m, the maximum bending stresses at the rail head and the maximum deflections of the rail were obtained and summarized as follows in Table B.5.

Table B.5. The maximum bending stress at the rail head and the maximum deflection of the rail under each track modulus when the railpad damping varies

Parameter	Stress (MPa)			Deflection (mm)		
Damping (kN.s/m)	7	70	700	7	70	700
U=13.79 MPa	52.66	53.54	53.97	18.22	18.22	18.22
U=27.58 MPa	52.17	54.59	55.98	12.26	12.25	12.25
U=41.37 MPa	51.13	54.03	55.01	10.04	10.04	10.04

From Table B.5, it can be seen that, under each track modulus, when the railpad damping increases from 7 kN.s/m to 700 kN.s/m, the maximum bending stress at the rail head seems to increase a little but the difference is not more than 4 MPa. Under each track modulus, the maximum deflection of the rail seems to be constant when the railpad damping increases from 7 kN.s/m to 700 kN.s/m, with a maximum difference of 0.01 mm.

Under each track modulus, the maximum bending stresses at the rail head when the axle spacing L1 varies were obtained and shown in Figure B.2. It shows that, under each track modulus, the maximum bending stress at the rail head fluctuates when the axle spacing L1 increases from 2.0 m to 5.0 m. However, the maximum bending stress at the rail head in the axle spacing L1 range of 4.5 m to 5.0 m are always lower than that in the range of 2.0 m to 4.0 m. Besides, the maximum bending stress at the rail head at the axle spacing L1 of 4.0 m is always large in general. For example, under the track modulus of 13.79 MPa, the maximum bending stress at the rail head when the axle spacing L1 is 4.0 m is the second largest while the largest occurs at the axle spacing L1 of 2.5 m. Under the track modulus of 27.58 MPa and 41.37 MPa, the peak value of the maximum bending stress at the rail head both occurs at the axle spacing L1 of 4.0 m. Finally, under each track modulus, the curves of the maximum bending stress at the rail head vs. axle spacing L1 when railpad damping are 7 kN.s/m, 70 kN.s/m and 700 kN.s/m are quite close to each other.

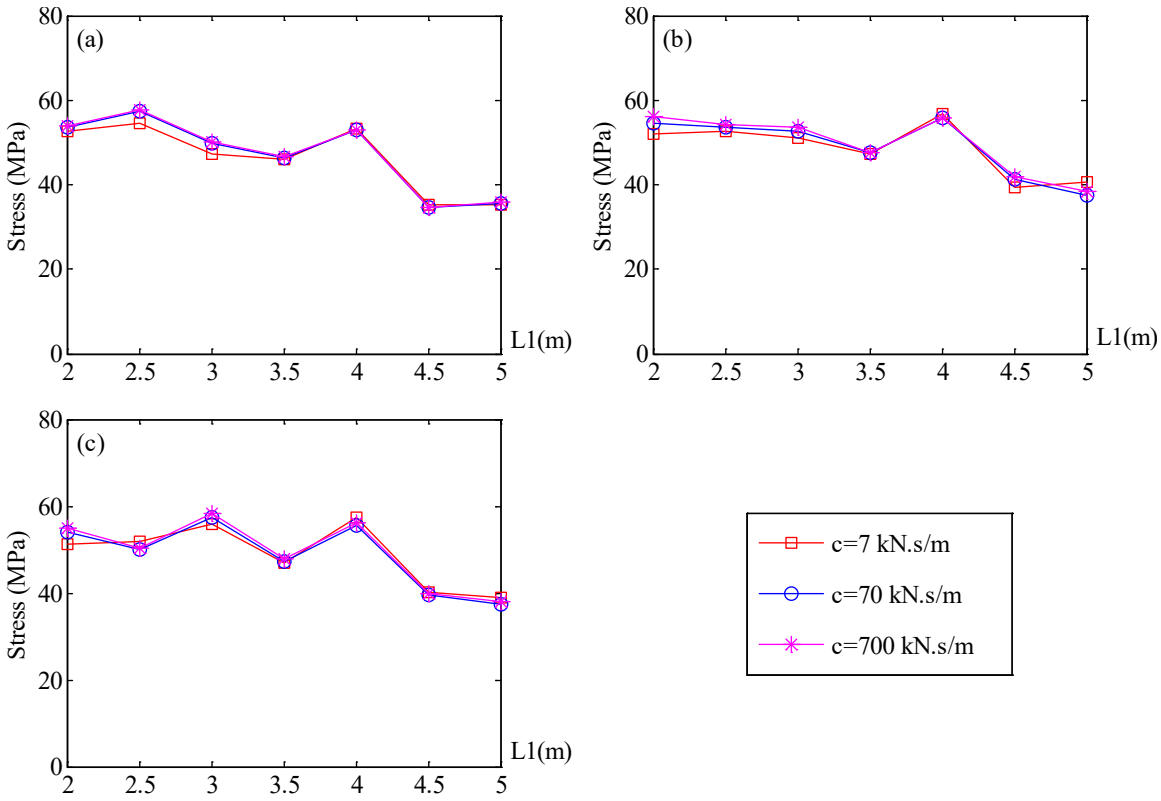

Figure B.2. The maximum bending stress at the rail head when the axle spacing L1 varies under each track modulus. (a) *U*=13.79 MPa (b) *U*=27.58 MPa and (c) *U*=41.37 MPa

B.4 Summary

Finite element models for the railway track system under dynamic loads were established. The train speed and damping parameters were determined and a sensitivity analysis was conducted to determine the suitable dimension and boundary condition for the track foundation in the model. Some initial results from the model were provided, including the maximum bending stress at the rail head and the maximum deflection of the rail.